THE DESIGN AND DEVELOPMENT OF GAP WAVEGUIDE-BASED SLOW WAVE STRUCTURES FOR TRAVELLING WAVE TUBES

AMIRA ZIED ABOZIED

A thesis presented for the degree of Doctor of Philosophy

School of Engineering

University of Lancaster

United Kingdom

7th July 2023

II

DECLARATION

I herewith formally declare that I, Amira Zied Abozied, have written the submitted thesis independently in accordance with Section PR 2.6.2 of the MARP 2022-23 Postgraduate Research Regulations. This thesis has not been handed in or published before in the same or similar form to any university or institution. I certify to the best of my knowledge that this thesis does not infringe upon anyone's copyright and all major sources of information are properly referenced. The work was completed under the guidance of Doctor Rosa Letizia, at Lancaster University, UK.

Signed

Amira Zied Abozied

7th July, 2023.

CONTENTS

VIII

LIST OF TABLES

X

LIST OF FIGURES

XIV

XV

XVI

XVIII

XIX

LIST OF PUBLICATIONS

A. Z. Abozied, J. Gates and R. Letizia, "Half-Height Pin Gap Waveguide-Based Slow-Wave Structure for Millimeter Wave Traveling-Wave Tubes," in *IEEE Transactions on Electron Devices*, vol. 70, no. 6, pp. 3295-3301, June 2023, doi: 10.1109/TED.2023.3266178.

A. Z. Abozied and R. Letizia, "Parametric Study of Pin-based Gap Waveguide for Millimeter Wave Slow Wave Structures," *2022 15th UK-Europe-China Workshop on Millimetre-Waves and Terahertz Technologies (UCMMT)*, Tønsberg, Norway, 2022, pp. 1-3, doi: 10.1109/UCMMT56896.2022.9994829.

A. Z. Abozied and R. Letizia, "Investigation of gap waveguide-based slow wave structure for millimeter wave travelling wave tubes," *2021 14th UK-Europe-China Workshop on Millimetre-Waves and Terahertz Technologies (UCMMT)*, Lancaster, United Kingdom, 2021, pp. 1-3, doi: 10.1109/UCMMT53364.2021.9569878.

A. Z. Abozied and R. Letizia, "Gap waveguides for millimeter wave slow wave structures," *2021 22nd International Vacuum Electronics Conference (IVEC)*, Rotterdam, Netherlands, 2021, pp. 1-2, doi: 10.1109/IVEC51707.2021.9722439.

GLOSSARY

Acronym	Definition
TWT	Travelling wave tube
VED	Vacuum Electron Device
SWS	Slow wave structure
GW	Gap waveguide
WG	Waveguide
DCW	Double corrugated waveguide
DVWG	Staggered double vane waveguide
mm-wave	Millimetre wave
MHz	Megahertz
GHz	Gigahertz
THz	Terahertz
AM	Additive manufacturing
Q-band	Frequency ranges from 33 – 50 GHz
E-band	Frequency ranges from 60 – 90 GHz
W-band	Frequency ranges from 75 – 110 GHz
D-band	Frequency ranges from 141 – 174.8 GHz
TWEETHER	Travelling wave tube-based W-band wireless networks with high data rate, distribution, spectrum and energy efficiency
ULTRAWAVE	Ultra-capacity wireless layer beyond 100 GHz based on mm-wave travelling wave tubes
FPGW-SWS	Full pin gap waveguide slow wave structure

HHGW-SWS	Half height gap waveguide slow wave structure
HWHP-GW	Half wall/half pin gap waveguide
Holey GW	Glide symmetric holey gap waveguide
LIGA	*Lithographie, Galvanoformung, Abformung*, A manufacturing process
CST	Computer Simulation Technology
CAD	Computer aided design
CNC	Computer Numerical Control
RF	Radio Frequency
PhC	Photonic Crystal
PIC	Particle-In-Cell
EM	Electromagnetic
EBG	Electromagnetic bandgap
TD	Time domain
FD	Frequency domain
TE	Transverse electric mode, a propagating electromagnetic mode which the electric field vector is perpendicular to the direction of propagation.
TEM	Transverse electromagnetic mode, a propagating electromagnetic mode which the electric and magnetic field vector are perpendicular to the direction of propagation.
TM	Transverse magnetic mode, a propagating electromagnetic mode which the magnetic field vector is perpendicular to the direction of propagation.
VNA	Vector network analyser
UV	Ultraviolet
PEC	Perfect electric conductor

PMC	Perfect magnetic conductor
AMC	Artificial magnetic conductor
S-parameters	Scattering parameters

ACKNOWLEDGEMENTS

"More than the fuchsia funnels breaking out of the crab-apple tree, more than the neighbour's almost obscene display of cherry limbs shoving their cotton candy-coloured blossoms to the slate sky of Spring rains, it's the greening of the trees that really gets to me. When all the shock of white and taffy, the world's baubles and trinkets, leave the pavement strewn with the confetti of aftermath, the leaves come. Patient, plodding, a green skin growing over whatever winter did to us, a return to the strange idea of continuous living despite the mess of us, the hurt, the empty. Fine then, I'll take it, the tree seems to say, a new slick leaf unfurling like a fist to an open palm, I'll take it all."

 - Ada Limón, 1976

XXX

ABSTRACT

Vacuum electronics have often been referred to as the birth of modern electronics and have been extensively used in applications such as satellite communication due to their significantly higher output power in comparison to solid state amplifiers. While solid state amplifiers are used widely in electronics, recent years have witnessed a resurgence of interest among researchers to develop vacuum electronics power sources. In particular, travelling wave tube amplifiers (TWTs) are being developed for the emerging applications of the millimetre wave (30-300 GHz) and sub-THz frequency (300 GHz -1 THz) range where they are currently the only viable technology to access high output power, robustness, and minimal losses. These developments hold potential from ultrafast wireless networks (5G/6G), where for instance power is needed to overcome the high atmospheric attenuation at these frequencies. To scale these devices down at the sizes imposed by operation above 70 GHz, and meet the requirements of these novel applications in terms of both performance and costs, new solutions are required for the electromagnetic design of the main component of the TWT, the slow wave structure (SWS). This thesis focuses on tackling some of the challenges of the TWT design in the upper millimetre wave spectrum by investigating the use of gap waveguide technology to realise the SWS. Gap waveguides have recently found significant application for the control of electromagnetic propagation at millimetre wave, where they can offer a low-loss solution versus microstrip circuit technology, within structures significantly easier to fabricate in comparison with conventional metal waveguides. Additionally, they can provide flexible designs, with inherent filtering capabilities that have been previously exploited in SWS design but in a simpler, easy to assemble topology. This work mainly investigates pin-based gap waveguides, resulting in two proposed structures: the full pin

gap waveguide SWS (FPGW-SWS) and half height gap waveguide SWS (HHGW-SWS). Numerical simulations predict suitable dispersion characteristics and interaction impedance for wideband operation and a flexible SWS design. The FPGW-SWS suggests an operation bandwidth ranging from 87 to 100 GHz based on cold simulations. Due to the additional advantages offered by the HHGW-SWS, including reduced aspect ratio pins and a compact coupler design suitable for very high aspect ratio sheet beams, this structure was chosen for detailed particle-wave interaction simulations and for experimental verification of the cold characteristics. A minimum gain of 25 dB is achieved in a single section TWT with a 10 GHz 3dB-bandwidth centred at 94.5 GHz, and a saturated output power of 160 W. The results from the test of the fabricated prototype of the SWS and couplers match the results obtained from simulations. An alternative approach to the design of the gap waveguide based on the holey glide symmetric gap waveguide is also investigated for comparison. It was found that this topology may be more suitable for moderate power, cost-effective applications.

CHAPTER 1: INTRODUCTION

Vacuum electron devices (VEDs) have provided efficient, high-power generation for decades. Early cavity klystrons and magnetrons were initially used in radio communications and have continued to develop into more advanced technology to this day. Even everyday objects, such as a microwave to heat up food, satellite TV, and musical amplifiers, utilize VEDs. Travelling wave tubes (TWTs) are a class of VEDs which are amplification devices still used to this day. The TWT was first invented by Kompfner in 1942 and remains an integral form of technology for satellite communication and radar systems [1], [2]. Interest is moving to the enhancement of wireless data rate communication, which would operate in the millimetre wave frequency and terahertz frequency range. To put into context, RF frequency is a range of electromagnetic spectrum of waves which range from MHz up to the THz. Visible light ranges from 380 to 700 nanometres, allowing us to see with our eyes and see various colours depending on the wavelength. Most radios, smartphones and satellites used currently operate in the microwave frequency range. Millimetre wave frequencies (30-300 GHz) house satellite devices and radar communications. As seen in Figure 1-1, as the frequency increases, the wavelength begins to get smaller and smaller.
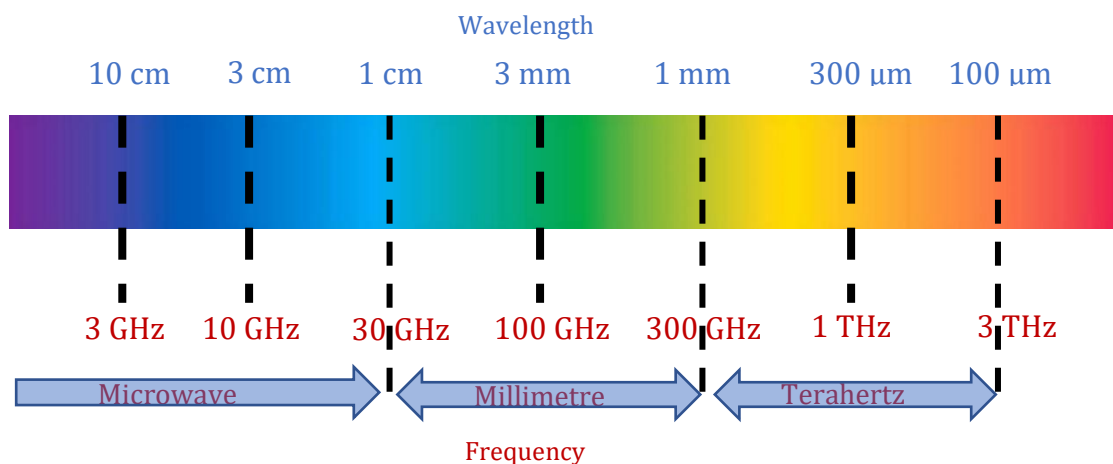
Figure 1-1: Electromagnetic spectrum from the microwave to the THz range.

3

Today, most everyday technology is based on the much smaller and low input power transistor, utilised as an amplifier. These devices have been an integral part in development of all modern technology, from smartphones to heart pacemakers. However, solid state amplifiers are limited to their relatively low output power and at this point in time, due to their small size there is a lack of control to the electron flow due to an effect called quantum tunnelling, the ability for electrons to penetrate barriers that are thin enough [3], thus limiting their continued development. Hence, researchers have looked to vacuum technology for higher frequency (mm-wave and THz) structures due to their high output power, robustness, and low losses. The typical TWT has a helix SWS, which cannot be scaled down above 70 GHz and is furthermore an expensive topology for widespread applications, leading researchers to pursue different SWS configurations.

1.1   Travelling wave tubes and their applications

Commercial TWT production is limited to a few worldwide manufacturers – CPI, Teledyne, and Northup Grumman to name the main few from the USA and Europe. Currently commercially available TWTs, which reach up to Ka-band (40 GHz) are detailed in Table 1-1 [4]. The Helix refers to the SWS, the core component of the TWT, which is widely used in commercial TWTs but not realisable commercially beyond 40 GHz.

Table 1-1: List of some commercially available TWT amplifiers [4].

Description	Frequency range (GHz)	Output power (W)	Gain (dB)
C-band Helix TWT	5.85 - 6.65	2250	44
X-band Helix TWT	7.9 - 8.4	2250	40
Ku-band Helix TWT	12.75 - 14.50	625	45
DBS-band Helix TWT	17.3 - 18.4	1250	52
Ka-band Helix TWT	18.0 - 26.5	40	32
Ka-band Helix TWT	26.5 - 40.0	40	37

A summary of state-of-the-art TWTs compared to solid state amplifier devices, is shown in Figure 1-2. The references in the figure are provided in the original paper, [5]. It should be noted that in this figure, 'commercially available' devices beyond 40 GHz refers to devices used in high-cost and specialised applications, such as development for NASA operations [6], but not widely available as compared to Table 1-1.
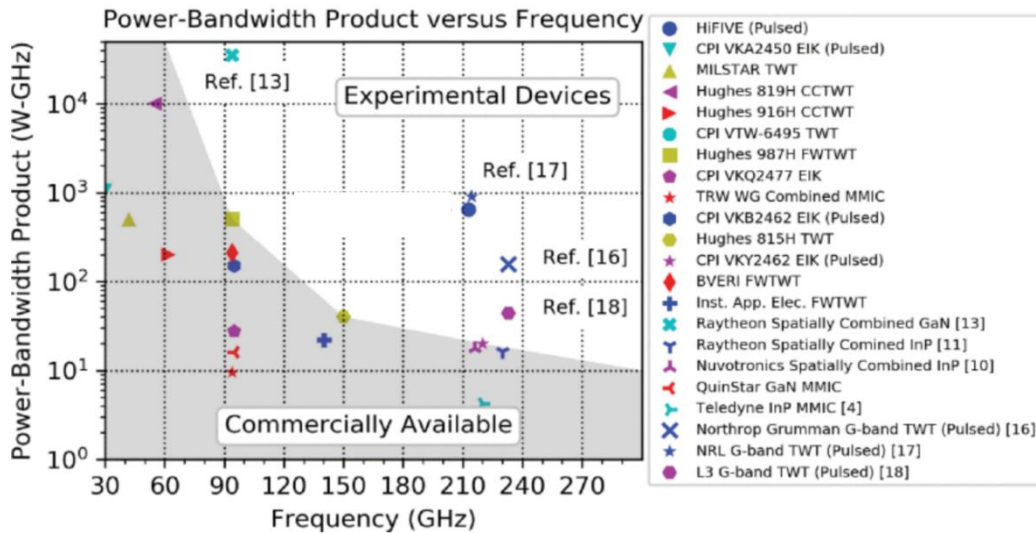
Figure 1-2: Summary of commercially available and state-of-the-art power amplifiers. [5]

GaN solid state amplifiers at W-band have demonstrated 31 W output power in the 94-98 GHz range [7], yet travelling wave tubes (TWTs) in this range can easily surpass 100 W in relatively broad bandwidths of 10 GHz [8]. Some of the leading and vital state-of-the-art technologies use TWTs. The explosion of technological advances shows no sign of slowing down. The promise of virtual reality instantaneously transmitted and 6G will ultimately require ultrahigh data rates in the hundreds of GHz, up to THz, to achieve this. Fibre networks can provide quick connections compared to broadband networks, but can be expensive to deploy and is not available in all areas. One solution is to use RF transmission in the mm-wave frequency range, such as in the Q-band (33 – 50 GHz), E-band (60 – 90 GHz) and W-band (75 – 110 GHz). This frequency range can provide wideband multigigabit per second data rate transmission. However, attenuation of mm-wave radiation due to high humidity or rain, means that a high output power at the level of tens of watts is needed to mitigate this. This makes VEDs, such as travelling wave tube amplifiers, a great candidate in the implementation of such a system.

Multiple projects have been achieved globally to demonstrate the possibility of next-generation networks, such as the European Union's H2020 TWEETHER (travelling wave

tube-based W-band wireless networks with high data rate, distribution, spectrum and energy efficiency) project, coordinated by researchers in Lancaster University. The goal of TWEETHER was to demonstrate a W-band (92 – 95 GHz) point-to-multipoint system for backhaul with high capacity [9].

Similarly, ULTRAWAVE (Ultra-capacity wireless layer beyond 100 GHz based on mm-wave travelling wave tubes) recently focused on the development of a high-capacity backhaul through 5G cell densification in the frequency range above 100 GHz, to provide more than 100 Gb/s per square kilometre in point-to-multipoint at D-band (141 – 174.8 GHz) [10].

1.2   Motivation for Research

Research within the mm-wave and THz frequency range has been explored but there are still major issues to be addressed regarding production, cost, and practical application. This project aims to introduce new concepts for the design and development of the core operating component in the TWT, the slow wave structure (SWS). Gap waveguide technology has been utilised in mm-wave devices, such as bandpass filters [11], and antennas [12], but so far its assessment for SWS design applications has been marginal. Here, their stopband filtering capabilities, potential for relatively easier, cost-effective fabrication and assembly are investigated in detail in the context of a compact, single section, broadband TWT design for the upper millimetre wave range.

1.3   Method outline

The methodology for this project involved a process of simulating, then validating results by fabrication of the structure and a cold test. This is the most viable method of validating results, as pure simulation-based results can present less realistic structures in terms of application despite rapid development of fabrication techniques. A mixture of

7

quantitative, empirical, and experimental data was collated. The calculation of dispersion characteristics, interaction impedance, scattering parameters, output power and gain were the main targets of design. A cold test is performed for the designed structure prototype, accompanied by particle-in-cell based simulations to study the properties of the beam-wave interaction and predict the TWT performance. A hot test would involve the design of additional parts for the TWT, including the magnetic focusing system, the electron gun and the RF windows for the input/output. This test would validate the PIC results; however, they are costly and time-consuming and so are outside the scope of this project. Dimensional tolerances of the prototype SWS, its assembly, and the matching of the measured scattering parameters to the simulated results were investigated.

1.4   Thesis outline

Following the Introduction, an overview of the relevant literature on travelling wave tubes and their operating principles, including beam transport, slow wave structures and their fabrication is presented in Chapter 2. Recent proposals for millimetre wave slow wave structures (SWSs) are discussed, including but not limited to rectangular corrugated waveguides, folded waveguides, photonic crystal-based SWSs, and a gap waveguide-based filter. A critical review of the literature is discussed to show the relevant gaps in the current technology.

In Chapter 3, the gap waveguide technology is then introduced. Different modifications to the pin-based gap waveguide that are in the literature are also reviewed. Unit cell parametric studies are also conducted on different types of pin-based periodic structures for the investigation and design of the gap waveguides' stopband properties.

The design of novel gap waveguide slow wave structures and input/output 90-degree coupler is then presented for the W-band operation in Chapter 4. The numerical study

goes into the details of the SWS dispersion characteristics, the interaction impedance, scattering parameters, power gain and saturated output power. Two different topologies are presented – the full-pin gap waveguide-based SWS (FPGW-SWS), and the half-height pin gap waveguide-based SWS (HHGW-SWS). The HHGW-SWS prototype is fabricated and measured against the simulations to validate the cold characteristics of this design.

Finally, an alternative gap waveguide topology is numerically studied and compared in Chapter 5. Similarly, to the case of the pin-based gap waveguides, the holey glide symmetric gap waveguide (Holey GW) is used to assist the design of the SWS at the W-band frequency range, including parametric studies of the unit cell geometry, the dispersion characteristics, the scattering parameters, predicted gain and output power.

The thesis concludes with a summary on the findings and implications of this work. The limitations of the research are outlined, relevant further work is proposed and discussed.

CHAPTER 2: REVIEW OF MILLIMETRE WAVE AND THZ TWTS

2.1   Introduction

A TWT consists of an electron gun, a magnetic focusing system, a slow wave structure and a collector. The interaction waveguide (the slow wave structure, SWS) is the core component of a travelling wave tube, setting the transfer of energy between the electron beam and the RF signal. The SWS geometry greatly affects the overall performance of the tube, cost, efficiency and size. Conventionally, microwave TWTs use the helix SWS which provides strong interaction between the electromagnetic wave and the beam. As frequency of operation increases and dimensions reach the sub-millimetre level however, fabrication of the structures becomes increasingly more difficult and costly, making the helix unfeasible. Therefore, a trade-off between interaction characteristics and fabrication constraints must be considered at these frequencies and new geometries of SWS need to be sought.

2.2   TWT operation

The conceptual schematic of a travelling wave tube is shown in Figure 2-1. The core elements of the TWT are the electron beam and a wave guiding element for the travelling electromagnetic wave. The electron beam is emitted from the cathode and travels in the longitudinal direction of the slow wave structure along the length of the structure. On injection, the phase velocity of the input RF signal is the speed of light (c) in a metallic waveguide. The electron beam particle's velocity will be only a fraction of this speed. In this instance since the electron beam velocity is much slower than the wave, the guiding element (the slow wave structure) aims to slow down the electromagnetic wave to have

11

the same phase velocity as the electron beam particles to allow interaction with the longitudinal electric field component of the travelling wave and therefore amplify the signal [13].
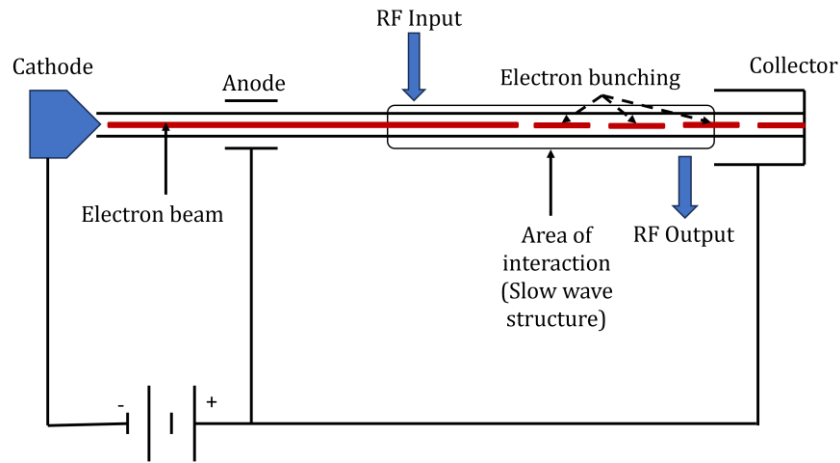
Figure 2-1: Schematic of the basic travelling wave tube (TWT).

As the exchange of energy occurs, the electron beam energy is modulated to form "electron bunches". TWT amplification occurs as the electrons lose kinetic energy and gain potential energy, adding energy to the slowed RF field, leading to amplification. [14]
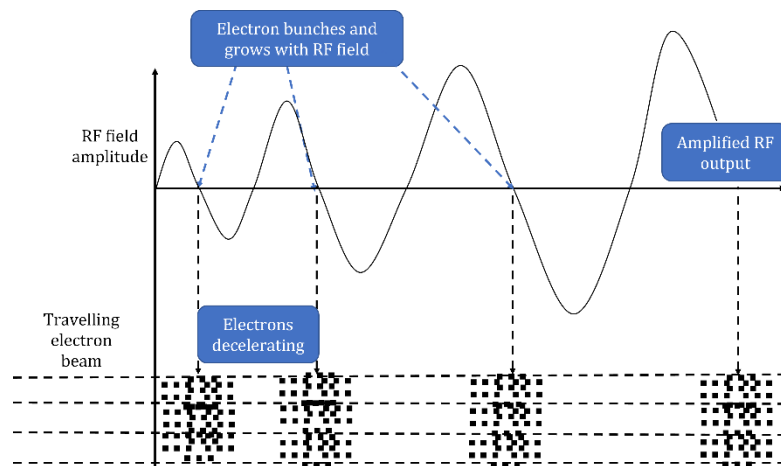
Figure 2-2: Depiction of how the electrons in the beam decelerate and accelerate to form bunches. Those bunches interact with the RF signal to amplify the signal.

2.3   Overview of longitudinally loaded periodic waveguide theory

The uniform waveguide cannot be used as the SWS in high frequency TWTs as such devices are typically periodically loaded, and the uniform waveguide cannot support the propagating modes. An obstacle produces change in impedance and loads the waveguide. This loading causes part of a propagating wave to be reflected. Using equally spaced obstacles means that a wave is periodically loaded. The fundamental TE_{10} mode generated in the uniform waveguide 'folds' in space harmonics, forward space harmonics and backward space harmonics. The wave solution for periodic structures differs from the uniform waveguide in that the electric field distribution varies according to the space harmonic in which the beam interaction occurs. The electric field quantities can be written as a sum of space harmonics. Each space harmonic is the phase shift of $\frac{\pi}{2}$ from the fundamental space harmonic. [15] The modes in periodic structures can be described with the Floquet theorem. The theorem states that in a periodic structure separated by period p, a mode at any given frequency have the same constant factor. [16] [15] Travelling waves can be defined with a complex number as the constant factor to add the phase shift between the points separated by a period (p). This factor can be written as $e^{-j\beta_0 z}$. The space harmonic introduces the periodicity along z. Written as a complex Fourier series form and multiplied by $e^{-j\beta_0 z}$, the field values can be written as a sum of space harmonics.

$$F = \sum_{n=-\infty}^{\infty} f_n e^{\left[-j\left(\beta_0 + \frac{2n\pi}{p}\right)z\right]} \tag{2.2}$$

Where f_n is the transverse field function of the nth space harmonic, and β_0 is the fundamental propagation constant. Therefore E_{zn}:

$$E_{zn} = \sum_{n=-\infty}^{\infty} E_{zn}(x,y)e^{-j(\beta_n)z} \qquad (2.3)$$

Where propagation constant β_n equals

$$\beta_n = \beta_0 + \frac{2n\pi}{p} \qquad (2.4)$$

Abiding by Floquet's theorem, each mode has infinite spatial harmonics n. For interaction to occur, the electron beam must synchronise with a spatial harmonic. The beam in theory can be synchronized with any value of n. The TWT operates in the forward space harmonic (n=0, n=1, n=2, etc...) as opposed to the operation of an oscillator which is in the backward space harmonic (n=-1, n=-2, etc...). The lowest order of n, the fundamental space harmonic (n=0) typically gives the highest interaction. In the conventional helix TWT, the interaction between the electron beam and RF input occurs in the fundamental space harmonic. This is where the electric field would typically be strongest. At high frequencies, the fundamental space harmonic is not generally used for synchronism as it would require either a very small period or a very high beam voltage. Therefore, high operating frequency interaction often occurs in the first space harmonic. Figure 2-3
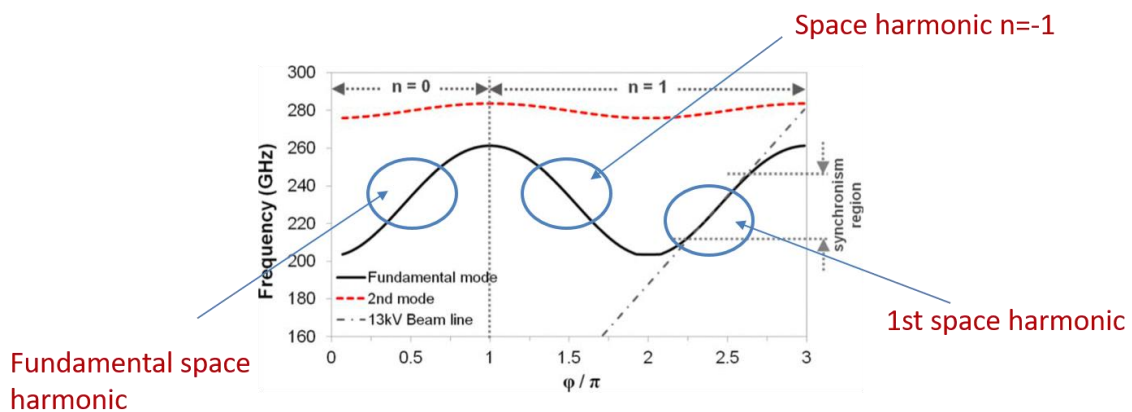
Figure 2-3: Dispersion curve of a periodic SWS showing where space harmonics appear on the propagating mode. Beam interaction occurs in the 1st spatial harmonic (n=1) [22]

shows in more detail where the spatial harmonics lie on the propagating mode on the dispersion curve of a waveguide.

From here, interaction impedance (K) of the wave can be calculated. Interaction impedance is a measure on how effective a slow wave structure is at slowing the phase velocity of the RF signal to permit beam-wave interaction. High interaction impedance leads to better tube efficiency, [17] therefore, when designing the SWS, the value of interaction should be considered. Interaction impedance is given by:

$$K = \frac{|E_{zn}|^2}{2\beta_n^2 P}$$

(2.5)

E_{zn} and β_n are defined as previously mentioned, and P is the power flow or flux of the SWS, which can be derived from Poynting's theorem. [16] Power flow [15] can be expressed as:

$$P = \frac{V_g}{p}$$

(2.6)

Where p is the period length, $V_g = \frac{d\omega}{d\beta_n}$ which is the group velocity, derived from the phase velocity described as $V_p = \frac{\omega}{\beta_n}$.

2.4   Electron beam dynamics

In the electron gun and collector, DC voltage is applied to produce fields that accelerate or decelerate electrons. As discussed in [14], the source of electrons for the electron beam is provided by the cathode, as can be seen previously in Figure 2-1. Typically, heating the cathode emits electrons through the process of thermionic emission. Specific configuration of the electron gun creates the desired focused electron beam with the

chosen geometry, such as a cylindrical or a sheet beam, to provide the best interaction with the SWS.

The electromagnetic fields produced by the beam electrons (space charge forces) can cause undesirable consequences to the trajectory of the beam. To solve this, external magnetic focusing systems are implemented in TWTs to maintain the beam geometry and avoid collision of electrons to the structure. The non-relativistic trajectory of the electrons can be defined by the equation:

$$m\frac{dv}{dt} = F_{RF} + F_{sc} + F_M \tag{2.7}$$

Where m is the electron mass, v is the electron velocity, F_{RF} is the electromagnetic force, F_{sc} is the space charge force produced by the beam electrons, and F_M is the magnetic focusing force.

Assuming that F_{sc} and F_M can be neglected, the Lorentz force explains the motion of the electrons interacting with the RF electromagnetic field in the following way:

$$m\frac{dv}{dt} = q(E_{RF} + v \times B_{RF}) \tag{2.8}$$

Where q is the electron charge, and E_{RF} and B_{RF} are the electric and magnetic fields of the RF signal respectively.

The longitudinal acceleration of the electrons entering the interacting region (assuming only longitudinal velocity), if $a_z = \frac{dv_z}{dt}$, is given by

$$a_z = \frac{q}{m}E_{zRF} \tag{2.9}$$

Thus, how electron beam bunching occurs can be explained. E_{zRF}'s sign changes periodically to achieve amplification of the RF signal. It should also be noted that bunching does not occur uniformly due to the non-uniform nature of the longitudinal RF

16

electric field across the interaction region. Transversally, the electrons follow a circular motion induced by the RF electromagnetic field, also known as centripetal acceleration.

The geometry of the electron beam can impact the beam transportation and magnetic focusing selection process. The cylindrical beam is the more conventional and well-studied beam. Due to the transverse electron motion, the circular motion of the electrons means that the cylindrical beam follows the electron motion and therefore requires less of a magnetic focusing force. On the other hand, sheet beams, which do not follow this motion, require a stronger focusing as the centripetal force tends to cause the beam to rotate. Additionally, the further the electron from the centre of the beam, the higher the sum of the repulsion forces at the edges of the beam occur. The sheet beam has more electrons spread further away from the centre of the beam in comparison to the cylindrical beam. Beam rotation is also impacted by the electron density, as the space charge force increases as more electrons are within the beam area. Simulations are developed using a constant magnetic field force across the TWT. In practice, various magnetic focusing systems are developed to minimize beam deviation. One example is the periodic permanent magnet (PPM) focusing system. The periodic switching of the magnet pulls the electrons in such a way that minimizes the rotation of the beam. The PPM focusing system is an attractive option due to their light weight and no electric power consumption. [18]

The solenoid magnetic focusing system produces a uniform magnetic field and is generally better studied and applied than the PPM. However, liquid cooling systems of the magnets are required and therefore can be bulkier and heavier. In any case, the development of magnetic focusing systems is rapid and hence the options for these systems and consequently the beam type flexibility increases.

17

The beam function can vary according to its geometry, the electron beams' current, voltage and density. The resulting amplification of the RF signal due to the electron beam is measured in terms of gain, shown by:

$$G\ (dB) = 10_{log} \left(\frac{P_{out}}{P_{in}} \right) \qquad (2.10)$$

Where G is the gain, P_{out} is the output power and P_{in} is the input power. Oscillation can also be visualized in the output power result if it is occurring in the tube, which when a positive feedback loop of the RF signal occurs causing it to reflect against the walls of the tube. Oscillations are an undesirable but common issue in TWTs, and can be caused by higher order mode interaction, band edge oscillation or coupling mismatch.

2.5   Numerical techniques for SWS design

Characterizing the operation of the SWS in simulations is the first step in development of TWTs. The main parameters that will be looked at in this thesis are dispersion, interaction impedance, scattering parameters, and particle-in-cell (PIC) simulations. Much of the work conducted was done with the package CST (Computer Simulation Technology) Studio Suite by Dassault Systems [19]. This is an electromagnetic modelling software which a range of solvers, based fundamentally on Maxwell's equations. Both finite-element and finite-integral techniques are used in CST. The mesh of the structure determines the accuracy of the solutions given, as each mesh cell solves Maxwell's equations in the singular cell area and the result is a summation of these solutions. CST uses two different types of mesh cells depending on the solver type and user's input – the tetrahedral, and hexahedral mesh cell. The tetrahedral mesh cell is built on the surface area of the structure, while the hexahedral mesh cells are cross-sectional based. The

mathematics of these techniques are not in the scope of this thesis, further information can be found in CST documentation [20].

The eigenmode solver is a fundamental solver used in unit cell parametric analysis, dispersion characteristics, interaction impedance and beam-wave synchronism studies. The solver allows the user to set boundary conditions, such as metallic or periodic boundaries, on the CAD drawn in the solver. The eigenmode solver studies the design when no excitation signal is applied.

The interaction impedance is also calculated in the eigenmode solver. Mathematically, the interaction impedance is defined by $K = \frac{|E_{zn}|^2}{2\beta_n^2 P}$. To find the numerical calculation for local values of the interaction impedance, the equation for interaction impedance is applied in the form of a macro in the CST Microwave Studio software to calculate K across the bandwidth of interest. To find the average interaction impedance, the macro is run over multiple discretized (x, y) points on the cross section of the beam placement in the SWS. The macro calculation has been verified to be accurate against results published in the literature.

First, a spatial Fourier decomposition must be taken to find E_{zn}.

$$E_{zn} = \sum_{n=-\infty}^{\infty} E_{zn}(x,y)e^{-j(\beta_n)z} \tag{2.11}$$

Electric field E_{zn} can be separated into real and imaginary parts of the electric field, E_{zr} and E_{zi} respectively. Hence, for a periodic wave function E_z with period p, transverse field quantity of E_{zn}, propagation constant β for space harmonic n;

$$E_{zn} = \frac{1}{p}\int_0^p (E_{zr}(z) + jE_{zi}(z))\, e^{j(\beta_n)z} dz \tag{2.12}$$

Substituting Euler's identity into (11):

19

$$e^{j(\beta_n)z} = \cos(\beta_n z) + jsin(\beta_n z) \tag{2.13}$$

Therefore:

$$E_{zn} = \frac{1}{p} \int_0^p (E_{zr}(z) + jE_{zi}(z)) * (\cos(\beta_n z) + jsin(\beta_n z)) \, dz \tag{2.14}$$

By expanding the brackets:

$$E_{zn} = \frac{1}{p} \int_0^p (E_{zr}(z) \cos(\beta_n z) + jE_{zr}(z) \sin(\beta_n z) + jE_{zi}(z) \cos(\beta_n z) - E_{zi}(z) \sin(\beta_n z) \, dz \tag{2.15}$$

Combining real and imaginary parts, as absolute values:

$$E_{zrT} = \frac{1}{p} \int_0^p E_{zr}(z) \cos(\beta_n z) - E_{zi}(z) sin(\beta_n z) \, dz \tag{2.16}$$

$$E_{ziT} = \frac{1}{p} \int_0^p E_{zr}(z) \sin(\beta_n z) + E_{zi}(z) \cos(\beta_n z) \, dz \tag{2.17}$$

To find the magnitude of the complex field of E_{zn}:

$$|E_{zn}| = \sqrt{|E_{zrT}^2| + |E_{ziT}^2|} \tag{2.18}$$

Finally, the interaction impedance can be calculated as:

$$K = \frac{|E_{zn}|^2}{2\beta_n^2 P} \tag{2.19}$$

E_{zn} and β_n are defined as previously mentioned, and P is the power flow or flux of the SWS, which is show in Equation 2.6.

The time domain solver is a finite-integration technique (FIT) based solver which calculates the electromagnetic propagation over a hexahedral mesh. The FIT is a type of finite-difference time domain (FDTD) calculation which uses the discretised integral-form Maxwell's equations. The discretised values of the electric and magnetic field can be summated to show the overall field profile of the structure and can calculate the scattering parameters when adding an input/output with an excited RF signal.

The frequency domain solver displays how much of the signal exists within a given frequency band and has a time-harmonic dependence of the calculated fields. The fields are then described by phasors by multiplying the phasor related to the transient fields with the time factor and taking the real part of the field ($E(t) = Re[E(\omega)e^{j\omega t}]$). The frequency domain can provide more accurate s-parameters with respect to the frequency points however can be more computationally intense for this reason. In CST, both a tetrahedral and hexahedral mesh can be applied to the frequency domain solver.

Particle-in-Cell (PIC) simulations are one of the more complex CST simulations provided. The solver uses a time domain solver to calculate propagating fields, then combines it with a quantised ballistic solver and particle interaction Monte Carlo simulation. Due to this, PIC simulations are extremely computationally demanding and take significant time for each simulation run. The exact method of CST particle studio suite is propriety; however, a general method can be outlined. For the particle emission of the electron beam, 'macroparticles' are utilised by grouping emission regions into a single larger particle. The mesh density of the particle emission points from the beam can be refined for further accuracy. CST uses variable-weight macroparticles, where the emission surface is uniform, and the charge-mass ratios are varied.

CST performs a 4-stage cycle of numerical integration by calculating the value, such as the velocity or position of a particle at points in time, and allowing the dynamics of the particles to evolve as time continues. The cycle runs a calculation for the current distribution from particle motion ⇢ updating the electric and magnetic fields ⇢ interpolating the fields at particle positions ⇢ updating particle positions and momentums [20].

2.6   SWSs proposed designs for TWTs

Many alternative structures have been proposed for high frequency devices in recent years. These structures have been extensively researched at W-band and above. Easy geometries that can facilitate the fabrication, lower beam voltage of operation and increased repeatability are highly desirable. While more complex geometries may provide higher interaction impedance, depending on the complexity of the structure, the microfabrication methods can be costly and difficult to scale to mass production. A trade-off between interaction characteristics and fabrication constraints must be considered in this instance.
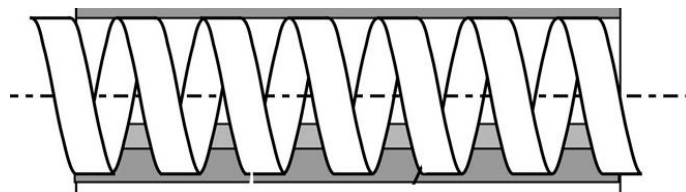
Figure 2-4: Helix slow wave structure (SWS). [16]

The conventional TWT contains a helix SWS. A helix SWS is the most common SWS and has been extensively used in travelling wave tubes and other VEDs. [14] The helix SWS, Figure 2-4, has many known advantages. Interaction impedance is high, and the bandwidth is broad. However, helix SWS are unfeasible to fabricate at sub-mm dimensions and although some examples exist at the lower millimetre wave range, they represent a very complex and costly structure to realise, unsuitable for most of the emerging widespread applications envisaged for mm-wave TWTs. Hence, there is a need to design different SWS to allow good interaction at frequencies above 70 GHz while minimising costs and complexity.

2.7   Corrugated waveguide

The corrugated waveguide SWS in Figure 2-5 is a periodic SWS for high frequency structures which provides a good compromise between ease of fabrication and relatively good interaction impedance. The corrugated waveguide is an umbrella term for many SWS with corrugations and is a simple way to get around fabrication issues of the helix SWS. Many novel SWS have been inspired by the corrugated waveguide, while also being integrated into other designs. Rectangular uniform waveguides are used as a convenient enclosure for this slow wave structure due to their simple fabrication, all metal structure and ease of integration. An example variation of the corrugated waveguide is the double staggard vane (DVG) waveguide, where corrugations are placed on the top and bottom walls. [21]
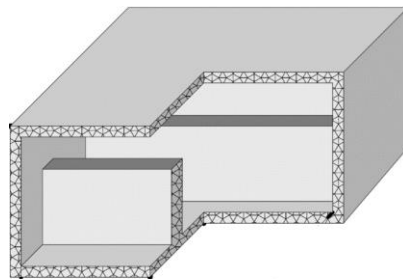
Figure 2-5: Cut-away view of the corrugated waveguide. [85]

2.8   Double Corrugated Waveguide

The double corrugated waveguide, Figure 2-6, (DCW) has two rows of parallel pillars within a rectangular metallic waveguide. When the two pillars are close with a small cross section, an electric field is formed between the pillars. The beam then travels between the two pillars where interaction occurs. A hybrid TE_{10} mode propagates in the DCW. A good beam-wave interaction occurs and has demonstrated an interaction impedance of up to 1.5 Ω in frequencies from 30 GHz – 150 GHz. [22] [23] [1] [24]

23
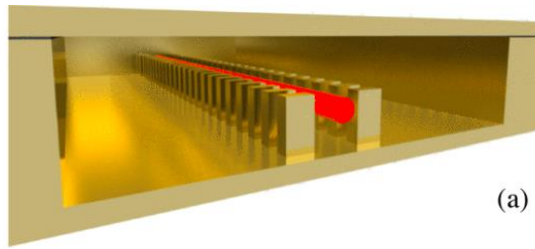
Figure 2-6: 3D Render of the double corrugated waveguide with electron beam passing between the corrugations. [95]

Good dispersion characteristics were also found with this SWS, providing wide bandwidth and good synchronism with the beam at < 20kV. Interaction occurs in the 1st spatial harmonic for the DCW, which is common in this type of SWS.

The double corrugated waveguide is an example of a slow wave structure that can support high operating frequencies while also being easier to fabricate. Fabrication of the SWS had been successfully done with CNC milling and deep x-ray LIGA [1], as well as UV-LIGA [25] which opens the possibility for easier batch production.

2.9   Folded waveguide (FWG)

The folded waveguide (FWG) is a planar rectangular waveguide folded into a serpentine shape. The unit cell of the FWG is shown in Figure 2-7 (b). In this example, a unit cell of the FWG with the circular beam tunnel is shown. It typically works with a beam voltage
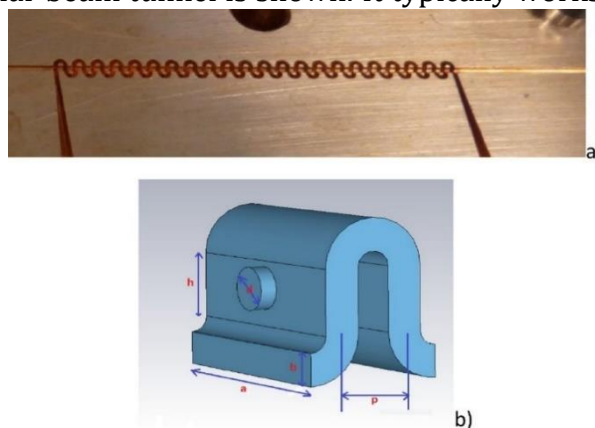
Figure 2-7: (a) Realized folded waveguide, (b) Unit cell for the FWG with beam tunnel. [1]

between 10-20kV. It is a popular waveguide configuration at sub-THz frequencies, due to its easy design, wide bandwidth, easy input/output coupling and relatively high interaction impedance. FWG TWTs have also been demonstrated by companies such as Northrop Grumman at frequencies such as 656 GHz. [26]

However, a problem is presented in the fabrication where it is done in two identical halves that are then bonded together. Misalignment of these halves by even 10 microns can degrade the properties of the SWS. [1]

2.10 Planar waveguides

Planar structures, typically integrated with a dielectric substrate, are a low-cost and effective system for mm-wave devices. They essentially integrate a microstrip-type transmission line into the enclosure of a waveguide, typically a rectangular waveguide. An example of the planar waveguide implemented in TWT devices in the W-band is the meander line SWS. Figure 2-8 shows a W-band variation of a meander line SWS achieving a peak gain of 37 dB, an output power of 25 W, while using a beam voltage of just 8 kV [27]. The advantages include achieving a similar gain to an all-metal SWS while maintaining a much lower voltage electron beam. Such structures can be easier to fabricate via printing techniques or UV-LIGA, which can lend to high-volume production. The biggest drawback is the requirement to include another material which may complicate assembly, and thermal resistance for the material need to be high.
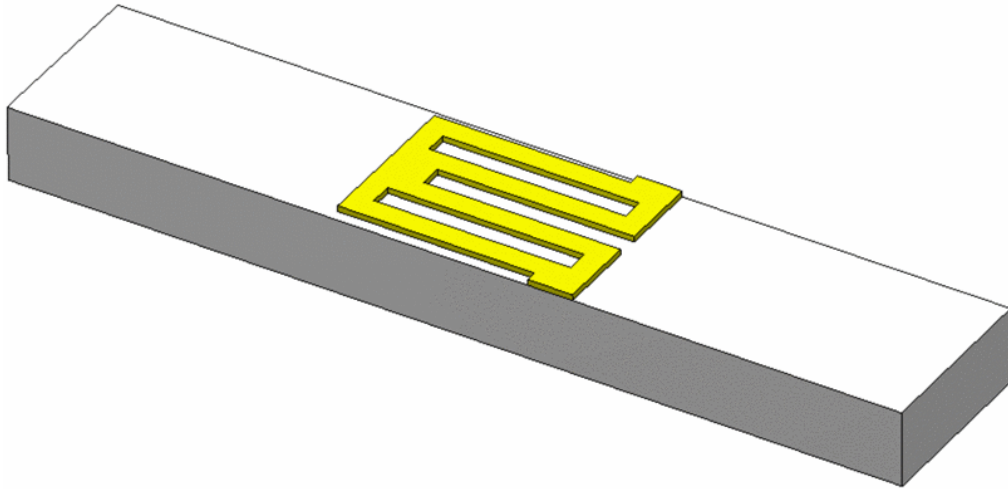
Figure 2-8: Variation of a meander line SWS. [27]

2.11 Photonic crystal corrugated waveguide (PhC WG)

Photonic crystals (PhC's) are artificial periodic structures with a period of the order of optical wavelength. One of the unique properties of PhCs is the photonic bandgap (PBG). It restricts the existence of optical modes and allows the strong control of light emission and propagation, and has been largely applied in waveguides. [28]

Also called photonic bandgap (PBG) structures, PhCs are implemented in the design of electromagnetic waveguides by introducing linear defects within the periodic lattice. These defects can be manipulated to optimize specific functions, such as waveguide bending and filtering.

Photonic crystals used as a lateral wall in a WG were investigated to be used in a corrugated rectangular waveguide configuration. Issues found in conventional metallic waveguides were alleviated with the introduction of photonic crystals, such as reducing difficulty with the vacuum pumping process, assembly and input/output coupling. [29]

An example of this PhC configuration is the 0.65 THz SWS designed for a backward wave oscillator (BWO) with an 11kV sheet beam. The BWO operates at a single frequency point, and the PhC wall is arranged in a periodic set of pins replacing metal walls, which allows

26

confinement to the propagating wave. An arrangement of the PhC lateral walls with a tapered central corrugation is shown in Figure 2-9.
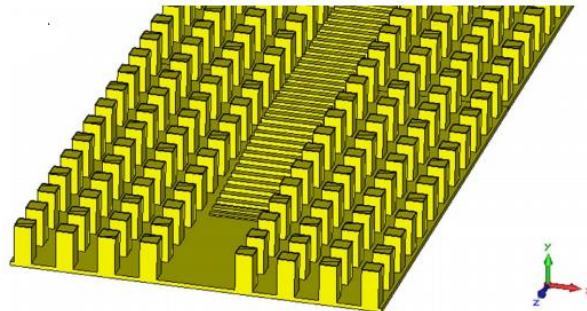
Figure 2-9: Concept of the photonic bandgap lateral walls with a tapered central corrugation. [29]

2.12   Gap Waveguides

Recently, the gap waveguide [30] was proposed as a structure that was easily fabricated, provided contactless walls on the top of the waveguide which reduced assembly issues, and showed lower losses. The gap waveguide is a recent technology that has shown to have several advantages for the design of mm-wave WG devices. [12] [31] [11] Only few numerical studies have been conducted on a gap waveguide folded waveguide (GGFW SWS) for G-Band TWTs, shown in Figure 2-10 [31], with none including the study on the interaction impedance or the experimental verification of the SWS properties. In this
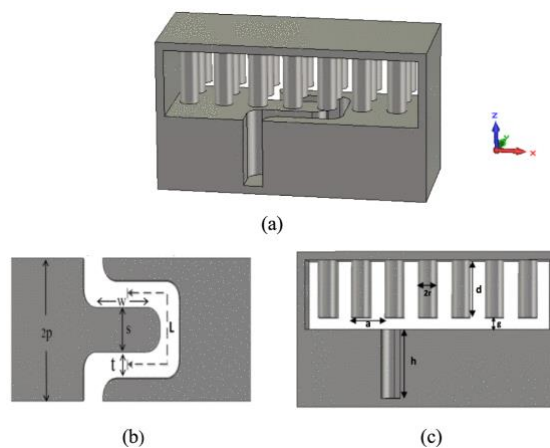
Figure 2-10: (a) Unit cell of the novel GGFW SWS. (b) Folded groove view. (c) Front view. The dimensions stated can be viewed in the original paper, [31].

27

context, the SWS integrates gap waveguide technology into a folded waveguide slot coupler TWT design with a sheet beam of beam voltage 21.6 kV with a peak power of 225 W at 220 GHz.

The potential for gap waveguides for the realisation of SWS at high frequencies can be outlined by the following advantages:

- No contact with the upper wall and lateral walls of the SWS – eases fabrication/assembly, e.g. easier assembly compared to Photonic Crystal structures.
- The gap waveguide can be designed to dampen higher order modes which reduces unwanted interaction with other modes and can reduce the risk of critical oscillations within the tube.
- The design flexibility of gap waveguides can be used to ease the design of the input/output coupler, even for very large aspect ratio sheet beams where the beam tunnel size is typically above the cutoff limit.

Gap waveguides are based on the concept of artificial magnetic conductors (AMC) which utilise high impedance textured surfaces. The details of the theory of gap waveguide technology are discussed more in-depth in Chapter 3.

2.13 Summary of proposed high frequency SWSs in TWT applications

Table 2-2 summarises a few of the successfully developed SWSs for high frequency TWTs, comparing operating bandwidth, beam type, beam current, beam voltage, gain and maximum output power. This summarises the current state-of-the-art SWSs for TWT technology which have been simulated for TWT prototyping. Those denoted with (~) have a machined prototype and measured for cold testing, while those with (*) have been demonstrated in a hot test.

28

Table 2-2: Summary of proposed state of the art high frequency TWTs.

Description	Operating bandwidth (GHz)	Beam type	Beam current (mA)	Beam voltage (kV)	Gain (dB)	Maximum output power (W)
Double corrugated waveguide (DCW) TWT [32]~	71 – 76	Cylindrical	100	12.8	28	70
Folded waveguide (FWG) TWT [26]*	656	Cylindrical	4.8	9.72	21.5	0.108
C-tunnel tapered Folded waveguide (FWG) TWT [33]	215 - 225	Cylindrical	50	17.8	21	70.5
Triangular pillar DCW TWT [34]~	141–148.5	Cylindrical	90	12.7	35	16
Planar meander line WG TWT [27]~	71 – 76	Sheet beam	65	8	31	25
Double staggard corrugated WG TWT [35]~	90 - 95	Sheet beam	500	20.6	36	1000
Gap-Groove Folded-Waveguide Slow-Wave structure TWT [31]	208.5-225	Sheet beam	70	21.6	35-40	225

2.14 Microfabrication of SWSs

Microfabrication is the process of creating small-scale structures and devices with dimensions typically in the range of micrometres to millimetres. Microfabrication is used in many nanotechnology and microelectronics applications [36]. There are many options of machining, such as CNC milling, lithography (specifically UV-LIGA) [37], deep reactive ion etching [38], and more recently additive manufacturing [39]. CNC milling is a very popular method for SWS prototypes due to its accuracy, using a computer programmed machine to etch out a design into a block of metal. The main issue with this is the time intensity, cost and lack of batch production availability. Another option, lithography, is used to transfer copies of a master pattern onto a solid material, the substrate, such as silicon or copper, by using a mask and a number of photolithographic methods. This method is a viable option for batch production. Additive manufacturing (AM) is a more novel form of fabrication for mm-wave VEDs. AM is a technology that can be used for microfabrication by building structures layer-by-layer from 3D digital models. Direct ink writing AM involves creating structures directly on a substrate using a focused beam or a nozzle that deposits material in a controlled manner. Examples of direct ink writing AM techniques include 3D printing, inkjet printing, and microextrusion [40].

2.13.1 CNC milling

CNC stands for Computer Numerical Control, which means that a computer controls the milling machine. CNC milling machines use rotating tools to cut away at a piece of metal, which is constructed via the configuration of a computer-aided design (CAD). CNC machines can provide highly precise, complex structures with minimal human input. These machines are widely used in many fabrication processes in the industry and can provide reliable manufacturing of parts. Some machines can achieve accuracies as high

30

as +/-0.0025mm [41]. Due to the requirement of high precision, accuracy and autonomous machining for mm-wave parts, this method can be particularly expensive especially as structure complexity increases and size decreases.

2.13.2   UV-LIGA

The basic method of UV-LIGA (UV *Lithographie, Galvanoformung, Abformung*) is as follows: The oxidized wafer, which can be made from copper or silicon, is coated with a negative photoresist layer. The wafer is then exposed to a UV light. After that, the wafer is then rinsed in developing solution, removing the unexposed areas of the photoresist and leaving a pattern. The exposed oxide and remaining photoresist are then stripped away. This method is illustrated in Figure 2-11.
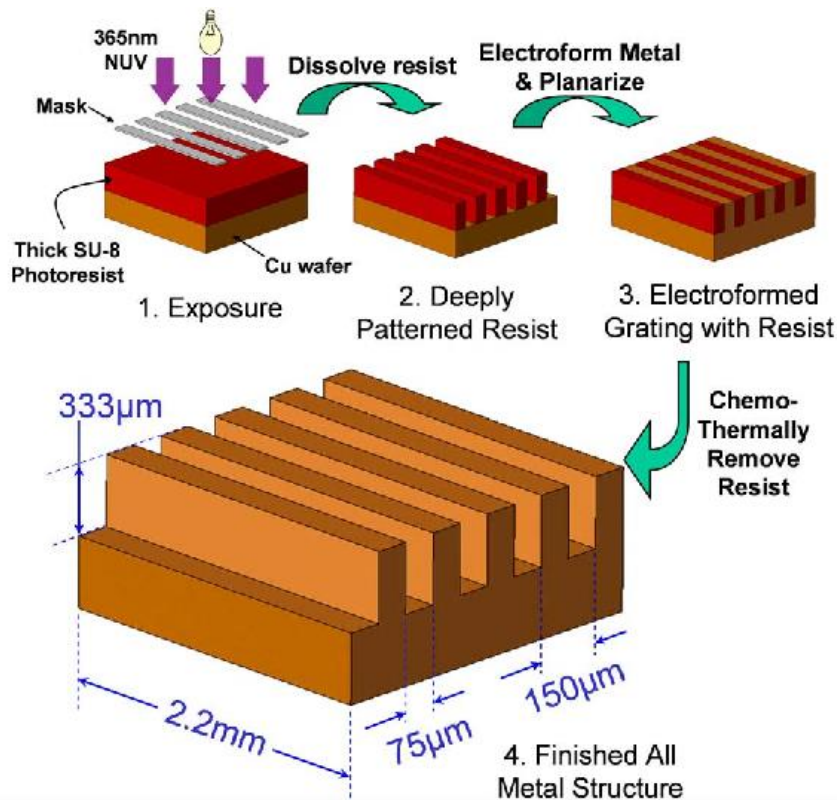
Figure 2-11: The UV-LIGA process for creating an all-copper grating using SU-8 photoresist, [42].

There are standard steps when it comes to lithography. Before lithography (specifically UV-LIGA) can occur, a polishing step of the substrate must be done when using copper to make it mirror-like. The substrate must then be coated with a photoresist normally made of a polymer, a sensitizer, and a solvent. This can be deposited in a number of ways: Spray coating, spin coating, dip coating, roller coating, curtain coating, and extrusion coating. Next, the soft/prebake occurs. This removes the remaining solvent from the resist which may contain built-in stresses. This step is critical as optimising it may increase device yield. SU-8 can be used as a photoresist in this application. Exposure to the UV light then happens - the smallest feature that can be printed using projection lithography is approximately equal to the wavelength of the exposure source. Next, the development of the structure causes dissolution of the unpolymerized resist. Development can be done wet or dry. De-scumming removes the unwanted resist. Post-exposure baking (PEB) removes any residual coating solvent and promotes adhesion. If the temperature goes up too quickly during PEB, it can cause cracking or delamination of the photoresist. This is done before etching or any adding on of materials [42]. Electroplating builds up the metal in the design left by the photoresist and UV exposure. The final step removes the remainder of the photoresist and polishing of the completed structure.

Using UV-LIGA on vacuum electronic devices (VEDs) is ideal for high aspect ratio structures. This can range from W-Band to 1 THz waveguides. UV-LIGA uses conventional radiation as lithographic light source, therefore is an affordable method of lithography without sacrificing quality.

The UV-LIGA process still has challenges. Electroplating for this structure must be done slowly and at a low electrical current as the electroplated metal must be built up to ensure a non-porous structure and a smooth finish to avoid excess surface roughness.

Additionally, overexposure of the photoresist during UV exposure can render the structure useless. Therefore, an ideal exposure time must be adhered to depending on the strength of the UV light and the thickness of the photoresist. The photoresist SU-8 is simple to apply and has good adhesion, however, removal is difficult and the removal of it affects the surface finish which in turn affects electric field [43]. Using plasma fluorination could be potentially used as an easier method for SU-8 removal [44], and other methods are still being explored. Lastly, while the UV-LIGA process is ideal for complex planar structures, due to the steps required for the electroplating and photoresist removal, it is most difficult to build complex structures in the longitudinal direction. 3D SWSs such as the helix SWS would not be possible to create via this method, while rectangular corrugations would be the simpler option for the fabrication of a 3D structure.

2.13.3   Additive manufacturing

The advantages of microfabrication using additive manufacturing (AM) techniques include high precision, design flexibility, and the ability to produce complex and intricate structures. Moreover, AM-based microfabrication techniques can often produce parts and devices in a single step, reducing the need for costly and time-consuming assembly processes. The continued development of AM-based microfabrication is likely to open new applications and enable the creation of novel microdevices that were previously impossible to manufacture.

AM techniques have shown great potential for the fabrication of SWSs used in TWTs [45]. Current AM techniques involve either using a metal as the material which is directly patterned – this method is the most suitable for TWT applications, although surface roughness provided by this method can introduce increased losses. The other method,

using a mould of the structure and pouring a polymer into it, then coating the polymer with a metal, is an interesting method to consider as it would significantly reduce the weight of the device. However, due to the high temperature emitted from TWT operation, the use of a polymer may not be suitable.

2.13.4   Assembly

The final key aspect of microfabrication involves the assembly of the SWS. Typically, SWSs are fabricated in separate parts, usually two parts but it can be more. After the SWS is fabricated, the individual components are aligned and assembled into the final structure. This step requires precision alignment of the components to ensure proper coupling and interaction between the waves and the SWS. The use of alignment pins can ensure this is done effectively. Once the components are aligned, they are bonded together using techniques such as brazing or diffusion bonding. Bonding is a critical step in the assembly process, as it determines the mechanical stability and electrical performance of the SWS. For higher frequency SWSs, diffusion bonding has been a well-studied method of bonding. Diffusion bonding is a joining process used to join two metal parts by applying heat and pressure in a vacuum or an inert atmosphere. In diffusion bonding, the surfaces of the two metal parts are cleaned and brought into contact, and then heated to a temperature below their melting point, typically around 50-70% of the melting temperature, for a certain period of time, which allows atoms to diffuse across the interface and form a strong bond.

During diffusion bonding, the high temperature causes the atoms at the interface to become highly mobile, and they start to diffuse across the interface, forming metallurgical bonds between the two parts. The process requires a high degree of cleanliness and

careful control of the temperature and pressure to ensure that the bond is formed uniformly and with the desired strength.

Diffusion bonding has several advantages over other joining processes. Firstly, it allows for the joining of dissimilar metals, which cannot be easily welded together due to their different melting points and thermal expansion coefficients. Secondly, it produces a joint with a uniform strength and without any distortion or residual stresses, which can be a problem with other joining processes. Finally, diffusion bonding can produce a bond with a high degree of precision and accuracy, making it useful in the production of complex parts with tight tolerances.

After the SWS is assembled, it is tested to ensure that it meets the desired performance specifications. This typically involves measuring the SWS's impedance matching, scattering parameters, and dimensional tolerances.

2.15 Conclusion

In the past few decades, there has been extensive research and interest in TWTs. Initially established in the 1940s, these devices were delegated to highly specialised, low volume electronics applications due to the emergence of solid-state transistors. However, with the pressing demand for high-capacity and high-speed mobile connectivity, TWTs operating at the millimetre wave and sub-THz range have emerged as the only technology capable of providing sufficient power to support the race for the next generation of wireless communication development. The slow wave structure, which defines the main electromagnetic characteristics of TWTs, has been investigated up to the 1 THz region [23]. Despite this progress, many challenges remain before such devices become fully demonstrated while being economically viable for the envisaged applications. Examples are their difficult fabrication and assembly, and less than ideal interaction characteristics

such as too much loss, or a narrow bandwidth. Some high frequency TWTs have been successfully used by highly specialised, low volume applications by Northrop Grumman [26] and NASA [6], these TWTs are costly to fabricate and not appropriate for large volume commercial use. To address these challenges, further research is necessary before high-frequency TWTs can be widely used. Designing these structures in a way that can alleviate the current issues found when fabricating and assembling these devices while keeping costs low is of great significance to further the potential of this field.

CHAPTER 3: GAP WAVEGUIDE TECHNOLOGY

3.1   Introduction

Gap waveguides are a recent development in mm-wave technology that offers low loss, flexible and easy to realise solutions to the confinement of electromagnetic waves at these frequencies. Gap waveguides are based on concepts that belong to the field of electromagnetic bandgap structure (EBG) structures; in that they use periodic structures to generate a stopband. The stopband can be exploited to confine the forbidden frequencies within a 'defect' region created in the periodic structure, which is the principle used when designing waveguides. The nature of the confinement realised in these structures permits to design channels with a single mode of propagation. This can be particularly useful to filter out transmission from undesired higher order modes. Additionally, compared to other electromagnetic bandgap-based waveguides, gap waveguides can allow for easier fabrication. To realise the stopband, gap waveguides are based on the use of high surface impedance textured surfaces [46].

The term electromagnetic bandgap structures (EBGs) cover periodic structures which generates a bandgap, a band of a range of frequencies that cannot propagate within the periodic lattice and uses this as a part of its operation. This type of structure can be utilized to design filters [47], mm-wave devices [48] [49], and recently their properties have been of interest for the design of vacuum electron devices (VEDs).

Photonic crystals are a popular EBG-based technology developed for the design of optical waveguides which work by introducing linear defects within the periodicity of the structure, typically made of dielectric material. This allows control over light propagation, thus, can be scaled to manipulate wave propagation in mm-wave and THz devices. All-metal photonic crystals have been successfully demonstrated to assist the

38

design of SWSs for THz VEDs, [50]. The gap waveguide works in a similar way to a 2D (two directions of periodicity, *x* and *z*) photonic crystal waveguide in that a forbidden frequency range is generated by the 2D periodicity of the structure, however this is realised in the presence of an air gap between a textured surface and the metal enclosure of a structure. This allows to design field confinement and waveguides that do not need electrical contact of the metal walls. Other advantages include the presence of the gap allows no contact between the top and bottom metal plates, which can potentially ease assembly by relaxing the requirement to bond walls together which can cause potential defects or misalignment in the structure. Additionally, an all-metal structure simplifies the fabrication and assembly process.

A comprehensive review of gap waveguides is shown in [51]. This Chapter introduces the theory and design guidelines of gap waveguide technology, and how it can be utilised in addressing some of the challenges found when designing high frequency mm-wave structures. A review of the main gap waveguide-based structures proposed in the literature is then presented. Finally, parametric unit cell studies on gap waveguide structures with various textured surfaces are shown.

3.2   Gap waveguide principles

Gap waveguides (GWs) are based on two parallel plates, one made of a perfect electric conductor (PEC) and one a perfect magnetic conductor (PMC), as shown in Figure 3-1. The PMC has a special case boundary condition which sets the surface current density to zero by setting the tangential component of the magnetic field to zero. This can be interpreted as a high surface impedance boundary condition. Electric current cannot flow in a PMC boundary as that would violate conservation of charge. No waves propagate in the direction of the periodicity between two parallel plates realizing the conditions of PEC

and PMC respectively when the air gap between them is less than a quarter of the wavelength.
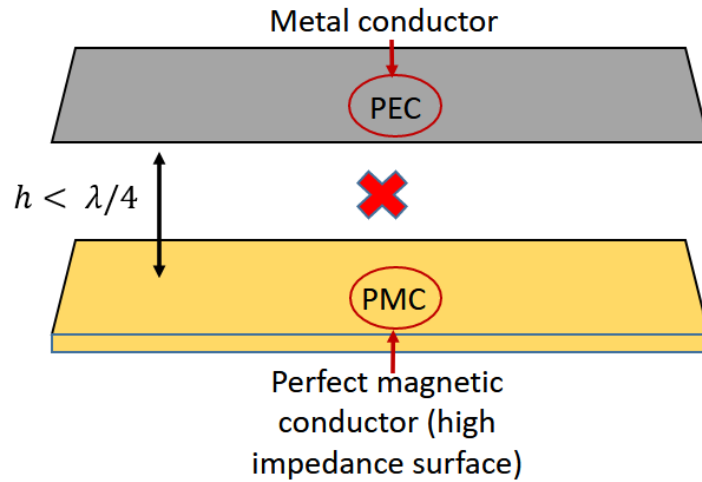
Figure 3-1: Schematic showing absence of parallel plate modes in the condition of a PEC and PMC surface less than a quarter wavelength apart.
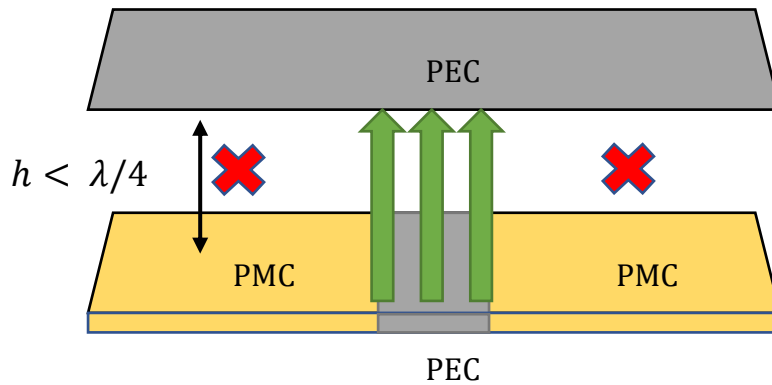
Figure 3-2: Schematic of the gap waveguide principle. A local wave is able to propagate along the PEC strip while being laterally confined by the PMC that stops all other parallel plate modes from propagating.

In contrast, parallel-plate TEM modes will propagate in the gap between two PEC parallel plates. If the bottom PEC plate is instead surrounded by a PMC plate on both sides, as shown in Figure 3-2, no waves will propagate in the section of PEC/PMC gap, only allowing a local TEM mode to propagate in the centre of the gap between both PEC plates, generating a propagation channel or waveguide. In practice, The PEC plate is realized by using a metal conductor such as copper. To realize the PMC which does not exist in nature, an artificial magnetic conductor (AMC) must be realised by using a high surface impedance structure, which can be created with a periodic textured surface, a so-called bed of nails, or mushroom type EBG textures, [46].

3.3   Textured surfaces

Textured surfaces are designed to change the surface impedance and tailor the propagation properties of surfaces waves. There are several types of textured surfaces. Mushroom-type EBGs are metallic patches with centre vias, operating as a high impedance surface [52]. These structures are mostly used in the microwave frequency range, although are limited by their narrow bandwidth.

One of the more popular pin configurations used to realise a textured surface is the so-called bed of nails, shown in Figure 3-3. The bed of nails configuration can synthesize an artificially high impedance surface. [52] The pins work as a high impedance surface within a stopband defined by a lower and upper cut-off frequency. The pin unit cell is shown in Figure 3-4. The pin structure has many advantages because it is an all-metal structure which allows a simple design for fabrication. This makes it suitable for high frequency mm-wave and THz designs. The bed of nails can be easily manufactured with various milling techniques. [53] outlines several design guidelines for the gap waveguide pin. The height of the pins is to be approximately $d = \lambda/4$, which defines the lower cut-

41

off frequency of the stopband. The upper cut-off frequency is defined as the frequency where $d + h = \lambda/2$, where h is the air gap between the pin and top PEC plate, with $h < \lambda/4$. The period p is defined as the pitch of a pin, and it should be small in relation to the wavelength ($\frac{p}{\lambda} \ll 1$).

(a)   (b)
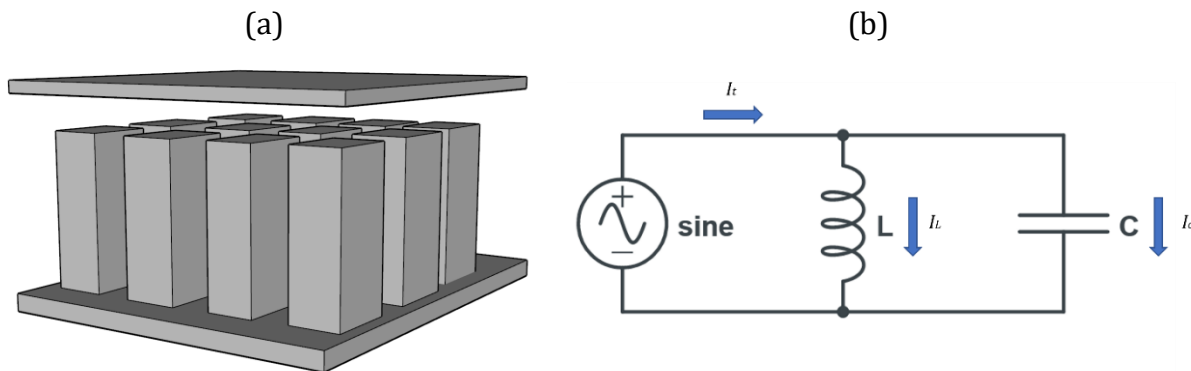
Figure 3-3: (a) Perspective view of the periodic bed of nails. (b) Equivalent lumped-circuit design of a transmission line which can describe gap waveguide technology.
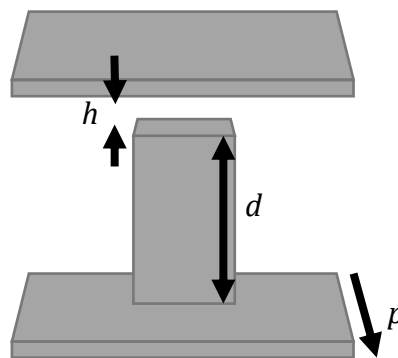
Figure 3-4: Unit cell of the textured surface 'bed of nails'. h refers to the gap height, d is the pin height, and p is the period.

The bed of nails surface unit cell can be described using lumped-circuit elements when the protrusion of the textured surface is small compared to the operating wavelength, Figure 3-3 (b). Near the LC circuit resonance frequency, the surface impedance is very high near the resonance frequency $\omega_o = \frac{1}{\sqrt{LC}}$. At resonance, the parallel LC circuit acts as an open circuit and no current flows through it, hence waves do not propagate

42

through the structure as they readily radiate into surrounding space. This defines the forbidden frequency range. In the frequency range where the surface impedance is very high, the tangential magnetic field is small, acting in the same characteristic as a PMC/AMC in a certain frequency range. [52] A larger gap causes a larger capacitance effect while the pillar structure has an inductive effect. A smaller pillar gives a smaller inductance.

The high impedance surface design plays a key role in the design of gap waveguides as the frequency range over which the local quasi-TEM mode can propagate as a single mode is determined by the frequency range over which there is a stop band of the parallel-plate modes. When all x and z propagating modes are forbidden from propagating in a certain frequency band, a stopband is formed. Only one direction of the propagating waves needs to be examined in this instance due to the symmetrical nature of the structure. The following equation describes the requirement for having no wave propagation for the parallel plate waveguide:

$$\left| \cos\theta - \frac{b_0}{2}\sin\theta \right| > 1 \qquad (3.1)$$

Where $\theta = kp$, k is the propagation constant of the parallel plate waveguide, p is the length of the unit cell with a shut susceptance across the midpoint of the line. The shunt susceptance b_0, is normalised to the characteristic impedance Z_0 of an infinite loaded transmission line. Depending on the frequency and the normalised shunt susceptance values, the periodically loaded line will exhibit either passbands or stopbands. [54] [55]

The half-height pin unit cell, shown in Figure 3-5, is a textured surface configuration similar to the full pin structure, but the height of the pin is split into two smaller aspect ratio pins, with the gap situated between the two sections. The half-height pin unit cell

43

has symmetry between the upper and lower plates. The PEC/PMC theoretical model described above for full-height pin gap waveguide is applied slightly different to the half-height pin structure. The solution of the generalised parallel plate condition, from equation (3.1) is used instead. The value θ becomes $\frac{\theta}{2}$, with a transmission line of length $\frac{p}{2}$, a shunt susceptance b_0, and another transmission line section of length $\frac{p}{2}$.
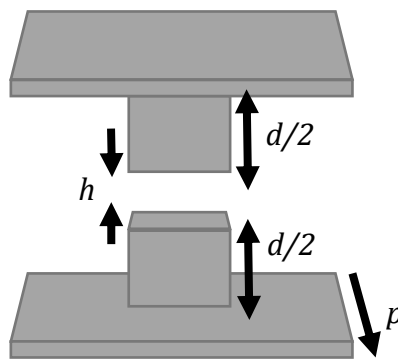
Figure 3-5: Unit cell of the textured surface half-height
bed of nails. h refers to the gap height, d is the pin height,
and p is the period.

3.4   Gap waveguide design

The gap waveguide can be a groove gap waveguide (GGW), or can be designed as a ridge gap waveguide, essentially containing a "ridge" between the pillar structures and allowing field confinement in the gap between the ridge and the top plate [56]. For a groove gap waveguide, a TE_{10} like mode will propagate in the metal strip, Figure 3-6 (a). The local wave in a ridge gap waveguide will be a quasi-TEM wave except for the ideal PMC case, where it is a TEM wave, Figure 3-6 (b).
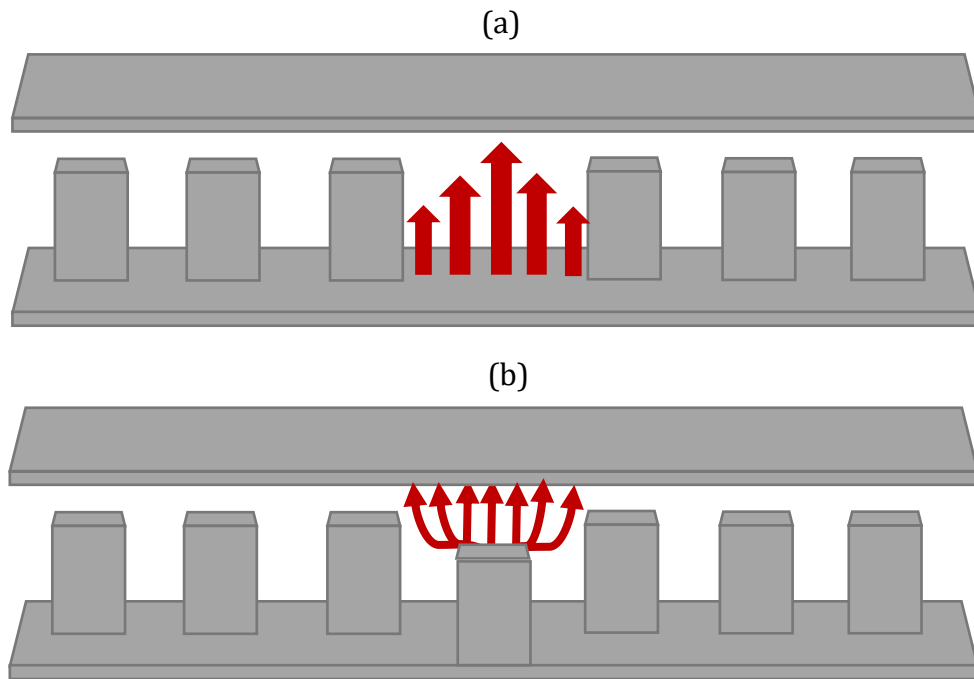
Figure 3-6: Schematic of the gap waveguide with a bed of nails surface acting as the AMC, with the generated field depicted. (a) Groove gap waveguide (TE_{10}), (b) Ridge gap waveguide (Quasi-TEM).

In addition, the gap waveguide in the case of containing a central SWS, can act as the metal walls of a rectangular waveguide as will be demonstrated in Chapter 4.

To summarise the most typical structures used in a gap waveguide, the schematics of

(a)　　　　　　　　　　　　(b)
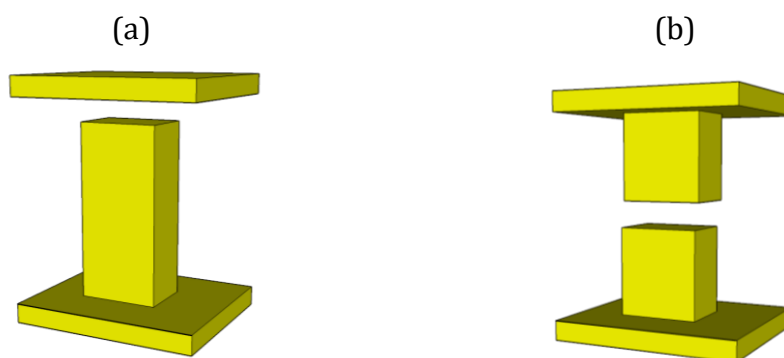
Figure 3-7: Perspective view of (a) Full pin unit cell, (b) Half height pin unit cell.

different types of EBG pins and central channels are shown in Figure 3-7 and Figure 3-8 respectively.

45

(a)   (b)
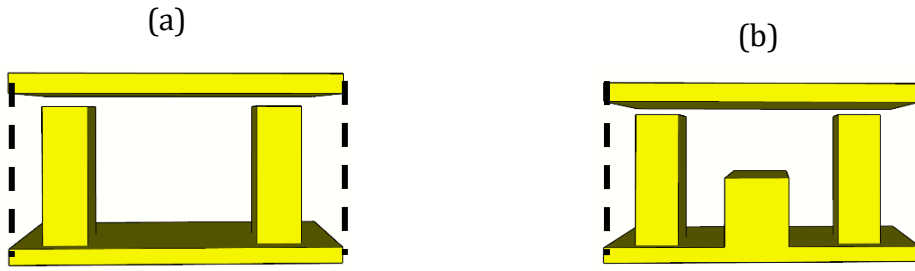
Figure 3-8: (a) Groove gap waveguide, (b) Ridge gap waveguide.

The summation of the design rules for the gap waveguide pillars, where h is the air gap, p is period, and d is pillar height are:

$$h < \frac{\lambda}{4} \tag{3.2}$$

$$\frac{p}{\lambda} \ll 1 \tag{3.3}$$

$$d + h \cong \frac{\lambda}{2} \tag{3.4}$$

$$d \cong \frac{\lambda}{4} \tag{3.5}$$

Where $\lambda = \frac{c}{f\sqrt{\varepsilon_r}}$, c is the speed of light, f is the operating frequency of the waveguide and ε_r is dielectric constant = 1 in vacuum.

3.5   Overview of Gap waveguides-based mm-wave components

Gap waveguide technology has been proposed in mm-wave waveguides and components, all of which are within the 1 – 60 GHz frequency range. A few examples are the full-pin gap waveguide [53], [56], half-height ridge gap waveguide [55], slow wave bandpass filter [47], the half wall-half pin gap waveguide [49], and the holey glide symmetric gap waveguide [57].

The first, and most popular implementation of gap waveguide technology is the full pin 'bed of nails' gap waveguide, first proposed in [53]. A low-loss, broad bandwidth is provided by the implementation of full pins in a gap waveguide arrangement.
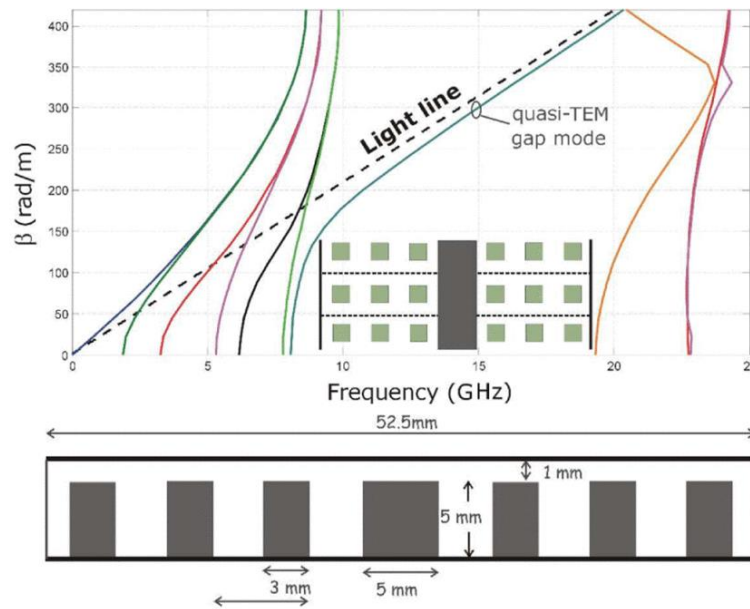
Figure 3-9: Dispersion diagram and schematic of the parallel plate ridge gap waveguide, consisting of a ridge in between a bed of nails (full pin). [53]

The dispersion and schematic of the proposed ridge gap waveguide structure in the frequency band 7 – 19 GHz is shown in Figure 3-9. The unit cell of the full-pin is shown in Figure 3-10 (a). All wave propagation is prohibited by the stopband frequency range, unless a guiding element is introduced in the form of a groove, ridge or corrugation in a channel for a locally generated propagation mode.

Recently, a variation of the full-pin structure was put forward; the half-height gap waveguide pin [58]. A less studied gap waveguide with the same premise as the full pin, but the gap is situated between two shorter pillars, depicted in Figure 3-10 (b). The half-height gap waveguide pin was implemented in a ridge gap waveguide in [55].

Recent studies have showcased the potential of employing another pin-based geometry as a viable alternative to conventional microstrip lines and waveguides. Researchers have

47

successfully implemented printed technology to create a novel gap waveguide structure known as the inverted microstrip gap waveguide, as demonstrated in [59]. In Figure 3-10 (c), the unit cell of the inverted microstrip gap waveguide is compared to the conventional pin configuration. This approach offers notable advantages, including low loss and broad bandwidth. The incorporation a dielectric material enables the manipulation of dispersion through material modifications and facilitates easier integration into planar waveguides such as meander lines.
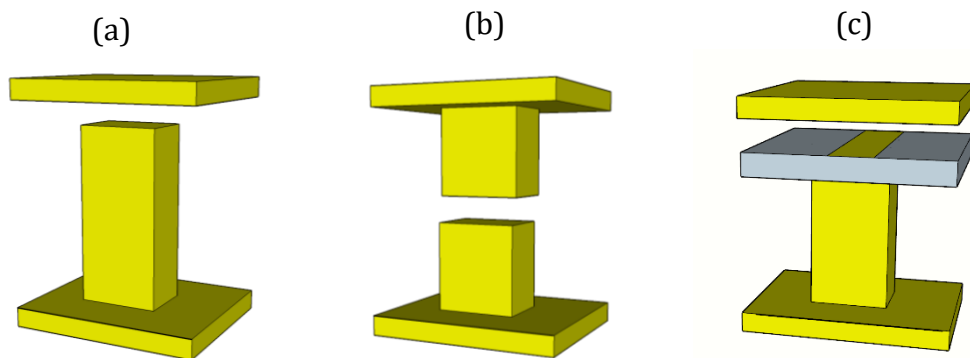
Figure 3-10: Comparison of unit cells for the (a) The full pin (b) The half height pin (c) The inverted microstrip pin.

The gap waveguide can be flexible in its design characteristics and placement of the gap. Another example of a gap variation in the pin is shown in [47] for the design of a bandpass filter. This presents the pins with a 'double gap', with a gap on both the bottom and top of the pins, with a plate keeping the pins suspended. A view of this double-gap bandpass filter is shown in Figure 3-11.
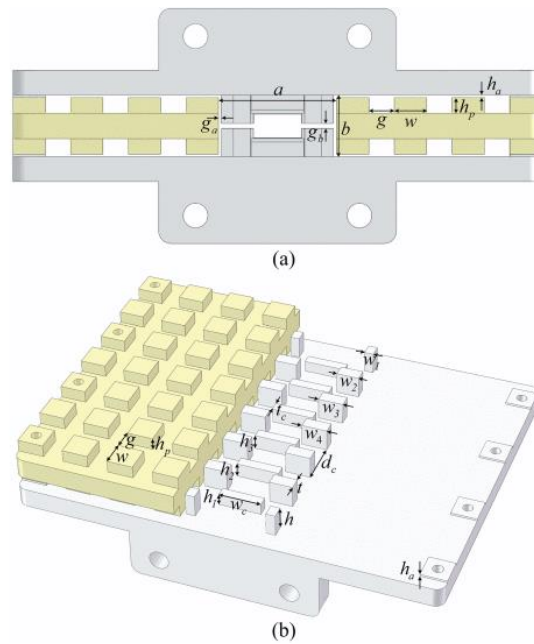
Figure 3-11: The double gap, bandpass filter. Dimensions
can be referred to in the original paper, [47]

The structure was successfully fabricated and provides the flexibility of replacing different pin plate variations for prototyping due to the presence of the suspended plate of pins.

Another interesting variation to the pin-based gap waveguide is shown in [49], based on a half pin/half wall unit cell topology. Figure 3-12 shows this consists of half a pin, placed on top of a solid wall acting as the AMC, with the top plate acting as the PEC. This structure can provide a similarly adequate stopband compared to the conventional pin, while potentially allowing for faster fabrication as there is only one section of shorter pins. However, the use of the wall does lend to less flexibility in design.
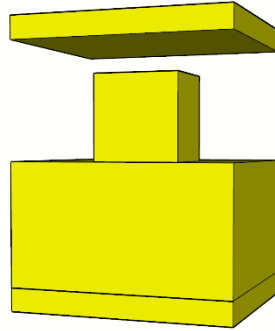
Figure 3-12: Proposed wall and pin form unit cell in
[49].

The final gap waveguide structure of interest is the holey glide-symmetric structure. It is

a recently proposed gap waveguide constructed via drilling of holes into a metal block to

create the AMC rather than using pins. With two parallel plates separated by a gap, if the

top holes are shifted longitudinally by half a period, a relatively broad stopband can be

achieved shown in [60]. This structure maintains the advantages of the pin-based gap

waveguide, while also promising a much simpler method of fabrication, potentially

lending to batch production and repeatability of the structure. The hole dimensions are

also larger in proportion to the frequency, which means the fabrication of a higher

frequency gap waveguide requires dimensions which are not as small as the typical sub-

mm dimensions when reaching the 80 – 300 GHz range [57] [60]. The glide symmetry can

be realised as 1D (one direction of periodicity) or 2D (two directions of periodicity)

structures. Figure 3-13 details the configuration of the 2D structure, as well as the unit

cell design for the holey glide symmetric gap waveguide.
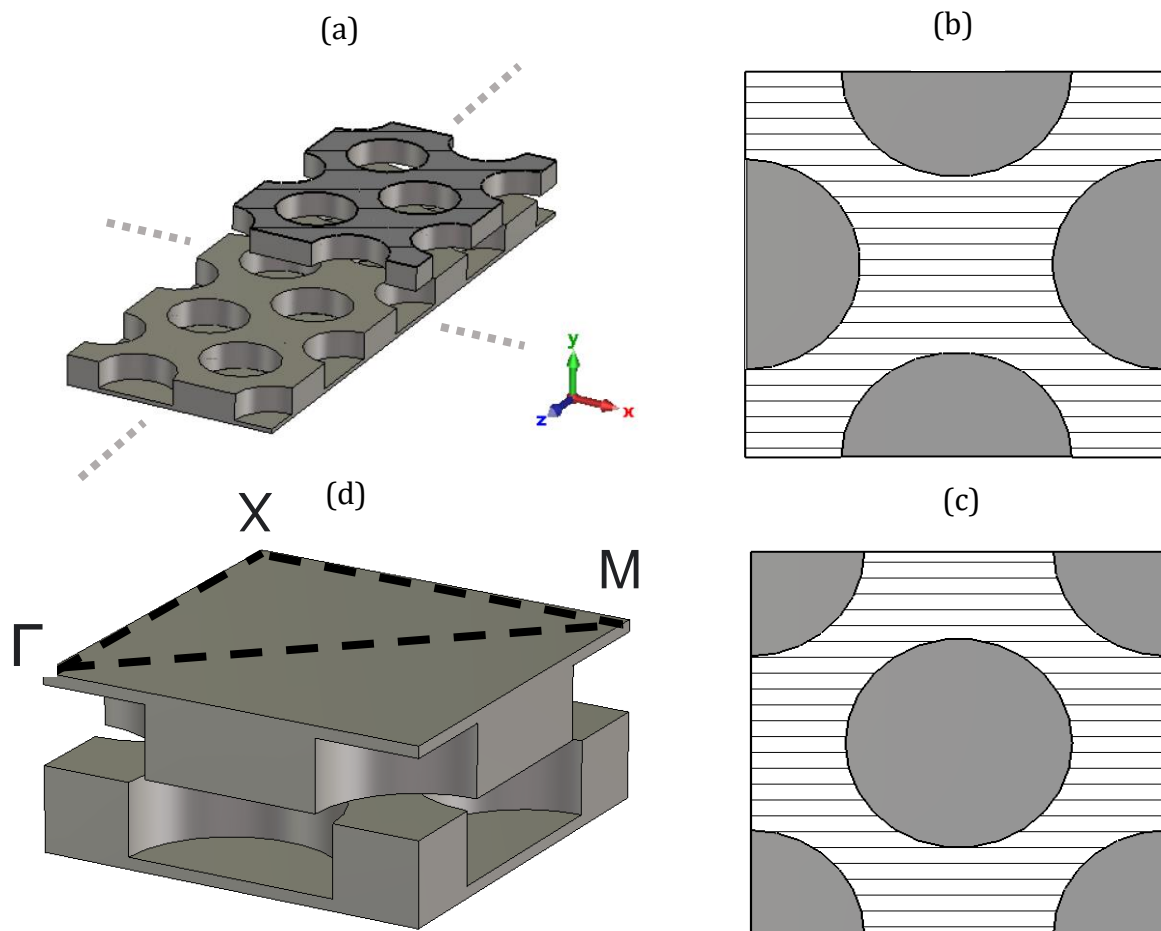
Figure 3-13: (a) Schematic of the top and bottom plates of the glide-symmetric holey gap waveguide configuration. (b) Bottom plate of the unit cell (c) Top plate of the unit cell (d) Perspective view which shows the irreducible Brillouin zone.

Full pin Gap Waveguide

Following the review on gap waveguide principles and the current proposals in the literature, the design and parametric analysis of the pin-based gap waveguide is conducted in the upper frequency range of the W-band (75 - 110GHz) to assist the design of a TWT SWS. Upon the successful implementation of the photonic crystal technology in [61], the full-pin design can be formulated with minimal adjustments, making it an ideal starting point as it is entirely composed of metal and compatible with rectangular waveguide machining. The stopband is determined by the gap between the top metal plate and the top of the pillar, which typically should be less than a quarter of the wavelength of the desired frequency. In initial eigenmode simulations, dimensions are

51

calculated according to the gap waveguide design guidelines. The dimensions and a schematic of the unit cell are shown in Table 3-1 and Figure 3-14 respectively. The material of the structure is set to be a perfect electrical conductor (PEC) in the eigenmode simulations. Periodic boundary conditions are set in the longitudinal direction (z) while the x and y boundaries are set as metal boundaries. A numerical convergence study is performed on the unit cell to find the minimum required mesh for numerical accuracy of these simulations, as shown in Figure 3-15. Convergence is reached at 20k tetrahedral meshcells. The stopband parametric study for the full pin unit cell is shown in Figure 3-16, varying the air gap h, and consequently the pin height d. From this study, it is apparent that a larger gap provides a narrower stopband, and vice-versa. The gap $h = 0.3$ mm gives a stopband of 60 – 100 GHz, while a gap of $h = 0.05$ mm is found to be 40 – 110 GHz. As the gap acts as capacitance and the pin as inductance, the resonance frequency shifts as these values change with different parameters. It should be noted that multiple mode solutions are generated in the gap, however for clarity of the plot of parametric studies, only the stopband edges are shown.

Table 3-1: Initial dimensions of the full-pin unit cell parametric study for h.

Parameter	Dimension (mm)
b	1.27
xo	0.58
zo	0.58
p	1.1
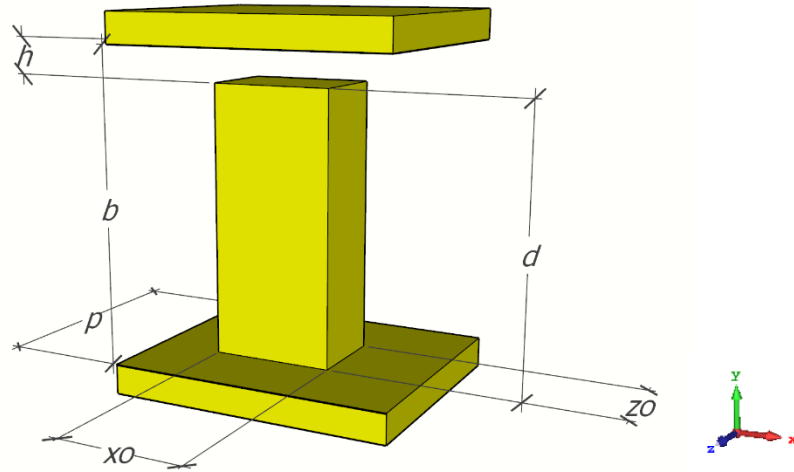
Figure 3-14: Schematic of the full-pin unit cell. Dimensions referred to in Table 3-1.
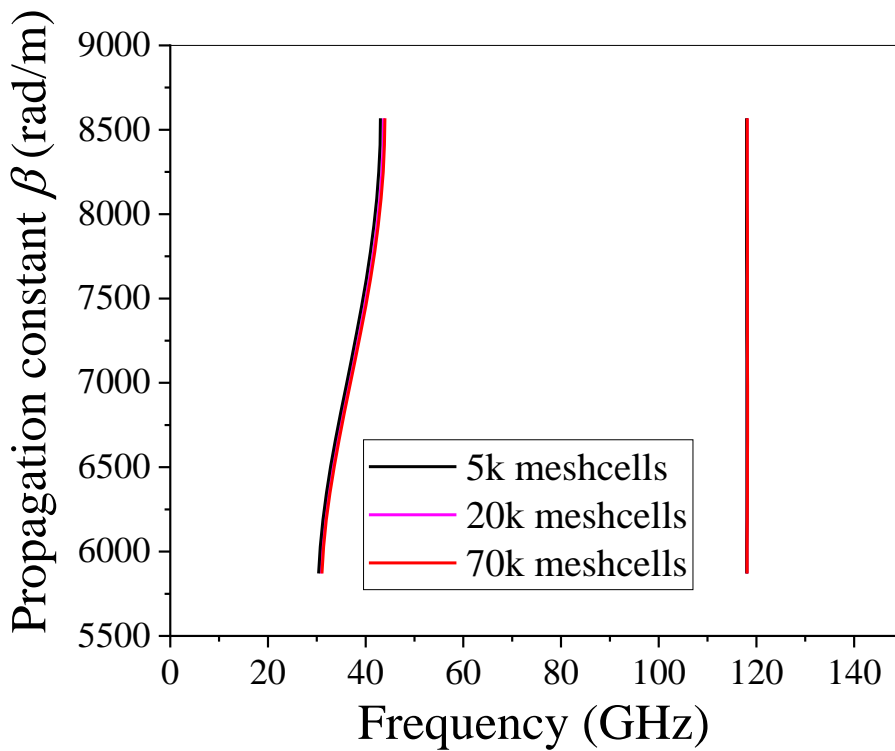
Figure 3-15: Convergence study on the mode dispersion (stopband) of the unit cell gap waveguide structure. The higher frequency cut-off (120 GHz) overlaps at all three convergence points. Convergence for the lower cut-off (40 GHz) is reached at 20k meshcells, therefore final mesh density is taken at 20k meshcells.
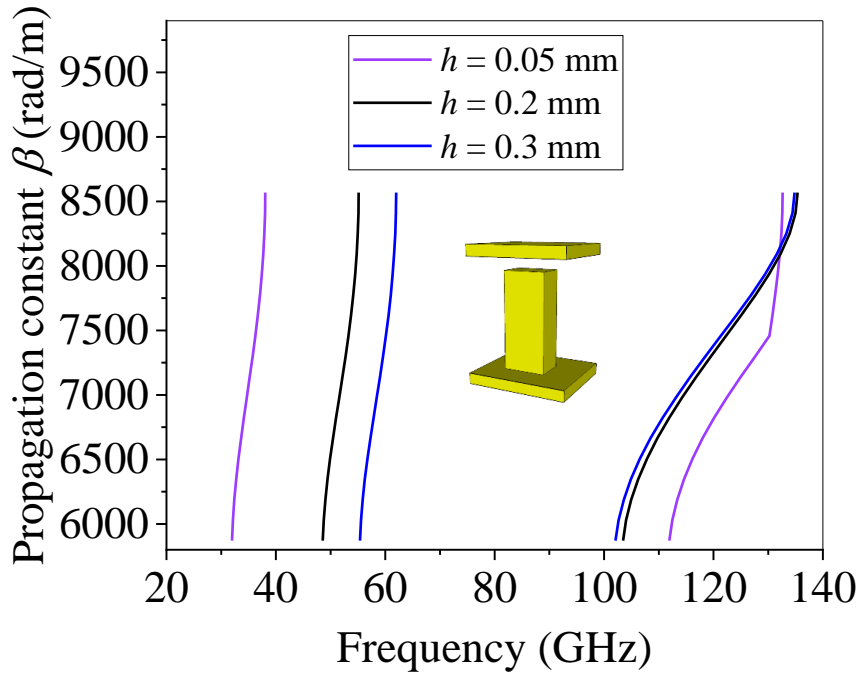
Figure 3-16: Full pin unit cell stopband parametric study. h = 0.05 mm (d = 1.22 mm). h = 0.2 mm (d = 1.07 mm), h = 0.3 mm (d = 0.97 mm).
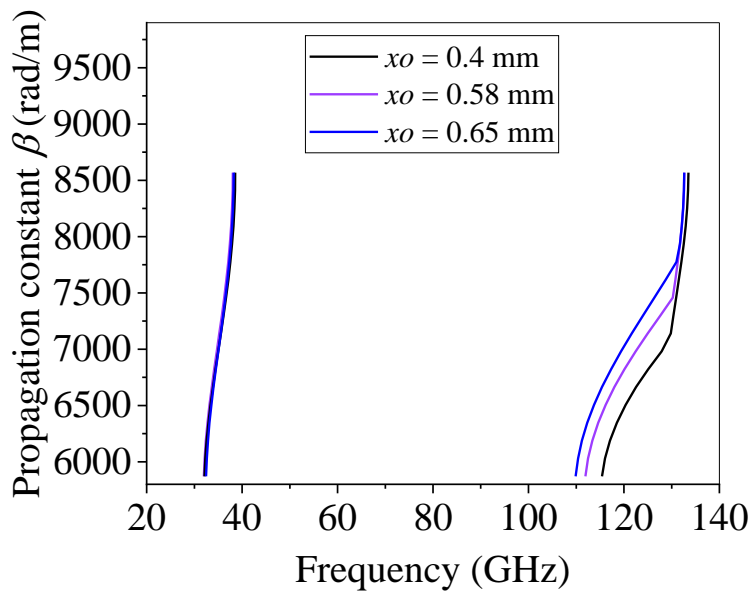
Figure 3-17: Full pin unit cell stopband parametric study for xo. Other dimensions b = 1.27 mm, h = 0.05 mm, d = 1.22 mm, zo = 0.58 mm, p = 1.1 mm.
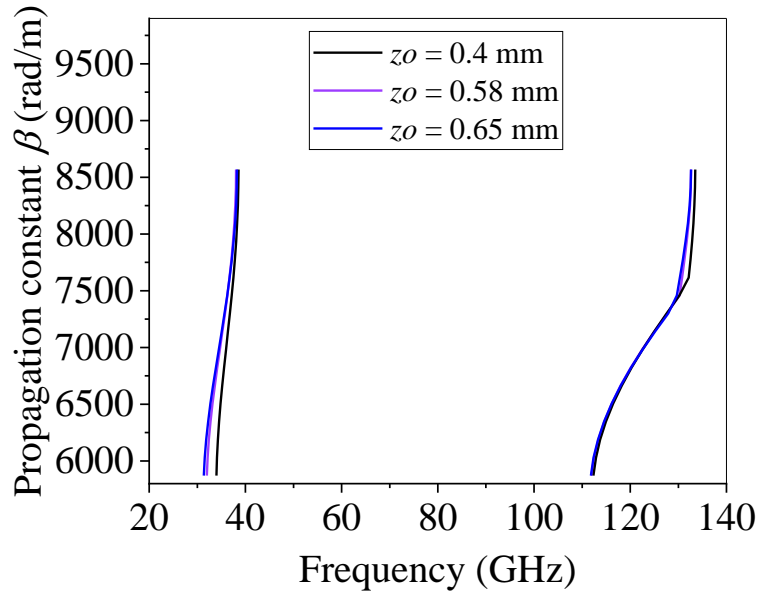
Figure 3-18: Full pin unit cell stopband parametric study for *zo*.
Other dimensions *b* = 1.27 mm, *h* = 0.05 mm, *d* = 1.22 mm, *zo* =
0.58 mm, *p* = 1.1 mm.

Studies were conducted on both widths of the pin, *xo,* (Figure 3-17) and *zo* (Figure 3-18).

In this instance, both studies gave a stopband of around 40 – 110 GHz. *xo* and *zo* had little

effect on the stopband and so there was flexibility on selecting these dimensions based

on other design constraints.

Next, the design of the groove gap waveguide based on the full-pin structure was

considered. A study was conducted to compare the use of one row of pins, vs. 3 rows of

pins at each side of the central groove, on the full pin groove gap waveguide in Table 3-2

as shown in Figure 3-19. Typically, at least 3 rows are required in a gap waveguide. In a

TWT application, a metal enclosure is required to create the vacuum seal. Because of this,

when a metal enclosure is considered, it can be seen that the stopband is successfully

generated with just one row of pins on each side of the central groove. The simulation is

run with metal boundaries in *x*. In this simulation, the width between the pins and height

is maintained as the width and height of a W-band standard rectangular waveguide (2.54

mm x 1.27 mm). The presence of this metal enclosure allows for flexibility in the number

of rows required to generate a stopband. This reflects the flexibility of the gap waveguide design based on its application. If more significant damping of unwanted modes is required, then additional rows of pins can be used to strengthen the stopband capabilities. The groove gap waveguide generates a propagating mode within the stopband, similar to that of the TE_{10} mode of a rectangular waveguide. The electric field distribution of this mode is shown in Figure 3-20. It can also be seen that the introduction of the groove channel to the pin structure does not impact the stopband generated by the pins.

Table 3-2: Dimensions for the full-pin groove gap waveguide.

Parameter	Dimension (*mm*)
b	1.27
h	0.05
d	1.22
xo	0.47
zo	0.58
p	1.1
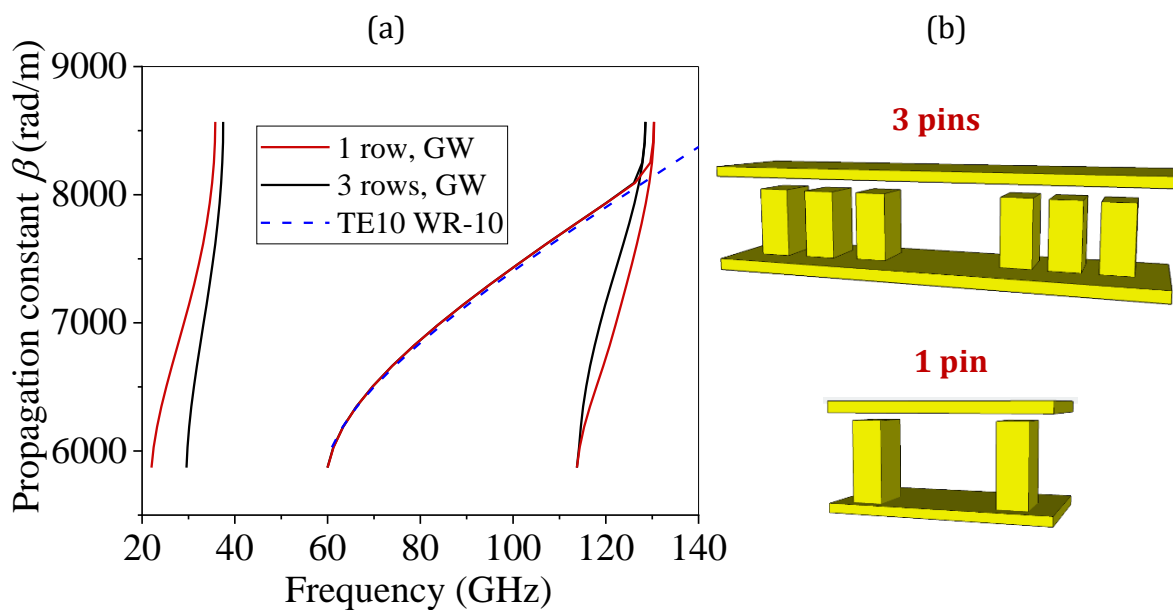
Figure 3-19: (a) TE_{10} mode and stopband of the full-pin groove gap waveguide, using 3 rows of pins vs. 1 row of pins. The TE_{10} mode of the W-band standard waveguide is superimposed over the figure. (b) View of the 3-row pin groove gap waveguide and the 1-row pin groove gap waveguide.
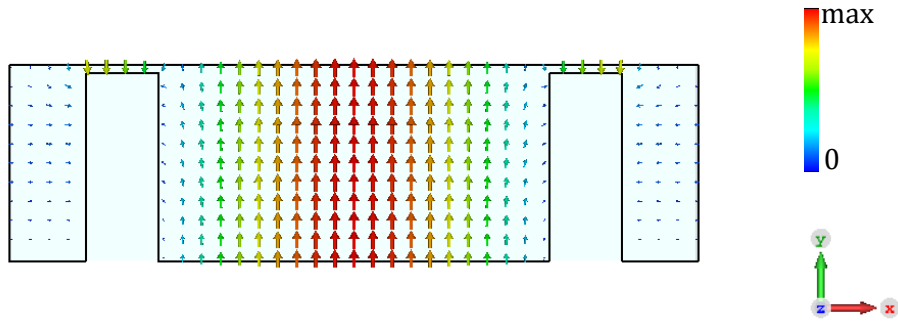
Figure 3-20: The electric field polarisation in the x, y plane of the generated TE_{10} mode for the full pin groove gap waveguide.

Half height Gap Waveguide

The half-height gap waveguide configuration is analysed next as an alternative to the conventional bed of nails surface. As introduced in Section 3.3, this topology can introduce some further advantages such as a shorter height of the pins and reduced aspect ratio that allow for easier fabrication via both CNC milling and LIGA process.
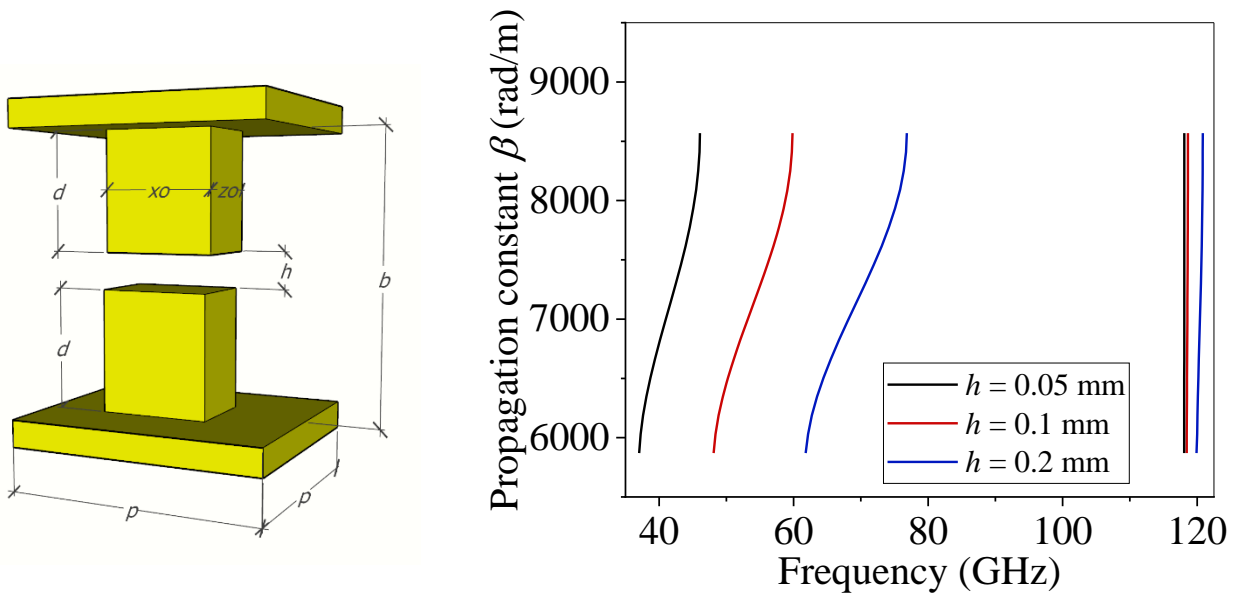
Figure 3-21: (a) Half-height pin unit cell schematic, b = 1.27 mm, xo = 0.47 mm, zo = 0.58 mm, p = 1.1 mm. (b) stopband parametric study.

The dimensions for this structure unit cell are kept the same as for the full-pin structure, except for the pin height reduced to $d/2$. The stopband dependence with air gap h is presented in Figure 3-21. With the same air gap height, the half-height pin provided a slightly shifted bandwidth of 43 – 120 GHz compared to the full pin.
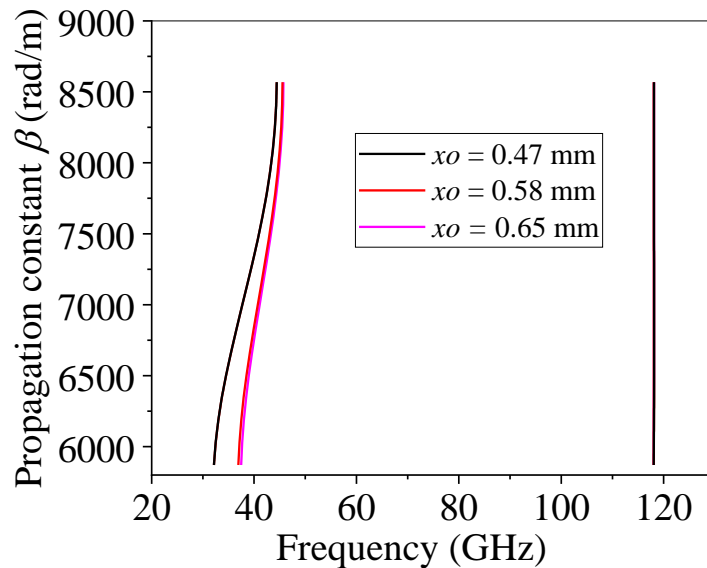
Figure 3-22: Half height pin unit cell stopband parametric study for *xo*. Other dimensions are b = 1.27 mm, h = 0.05 mm, d = 1.22 mm, zo = 0.58 mm, p = 1.1 mm.
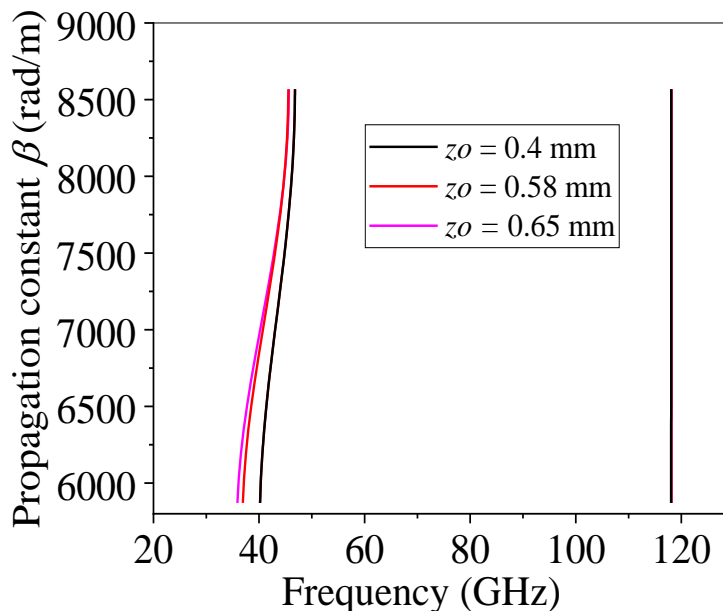
Figure 3-23: Half height pin unit cell stopband parametric study for *zo*. Other dimensions are b = 1.27 mm, h = 0.05 mm, d = 1.22 mm, xo = 0.58 mm, p = 1.1 mm.

Figure 3-22 and Figure 3-23 show the parametric studies for the half-height unit cell varying *xo* and *zo* respectively. For both the *xo* and *zo* variations, there is minimal change in the upper cut-off band edge, and a slight change in the lower cut-off band edge.

As done for the full-pin gap waveguide case, a groove gap waveguide based on the unit cell dimensions was designed. The channel width of the structure was set to the same as the width and height of a conventional W-band waveguide (2.54 mm x 1.27 mm). The study of comparing 3 pins vs 1 pin of the half height configuration was repeated, with similar results to that of the full pin, as shown in Figure 3-24. The TE_{10} of the conventional W-band waveguide is superimposed over this figure to compare the similarity of the generated TE_{10} mode in Figure 3-24 (b). The electric field distribution of the half-height groove gap waveguide is shown in Figure 3-25, indicating a TE_{10} mode polarisation.

Table 3-3: Dimensions of the half-height pin groove gap waveguide.

Parameter	Dimension (*mm*)
b	1.27
h	0.05
d	0.61
xo	0.47
zo	0.58
p	1.1
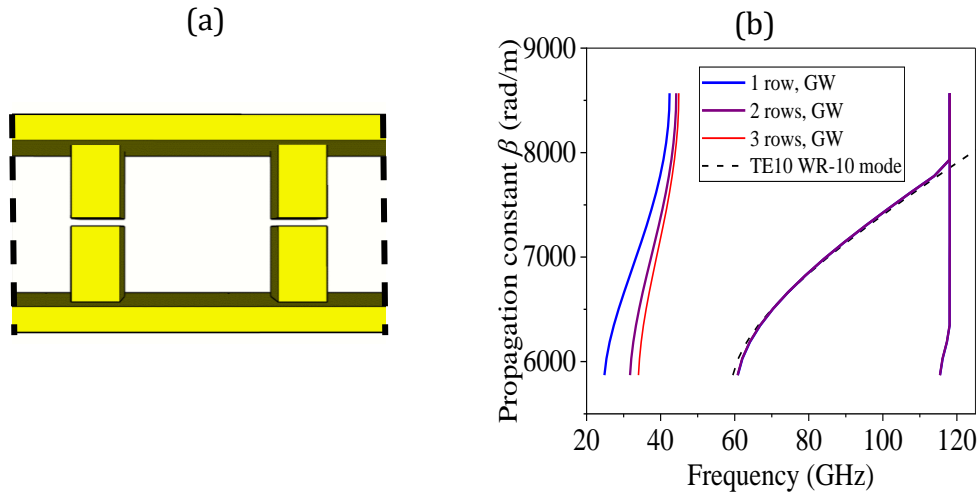
Figure 3-24: (a) View of the half-height pin groove gap waveguide, (b) Comparison of the TE$_{10}$ mode and stopband using 3 rows, 2 rows and 1 row. Superimposed is the TE$_{10}$ mode of the standard W-band waveguide.
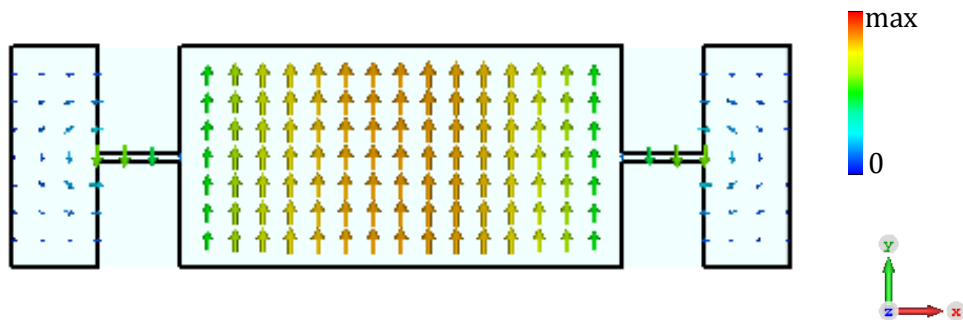
Figure 3-25: The electric field polarisation in the *x, y* plane of the TE$_{10}$ mode for the half height pin groove gap waveguide.

Half wall/Half Pin (HWHP) Gap waveguide

The wall and pin form waveguide, proposed in [49], was analysed for comparison. A modification of the pin/wall form is done by instead placing the gap between the top pin and the wall, shown in Figure 3-26 with dimensions in Table 3-4.

Table 3-4: Dimensions of the half wall/half pin unit cell.

Parameter	Dimension (*mm*)
b	1.27
xo	0.47
zo	0.58
p	1.1
d	0.61
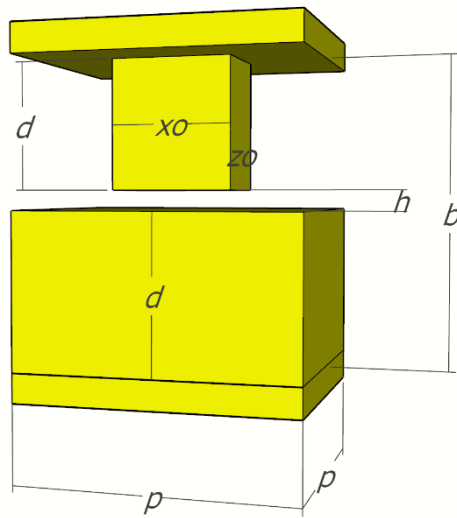
Figure 3-26: Half wall/half pin schematic. Dimensions are referred to in Table 3-4.
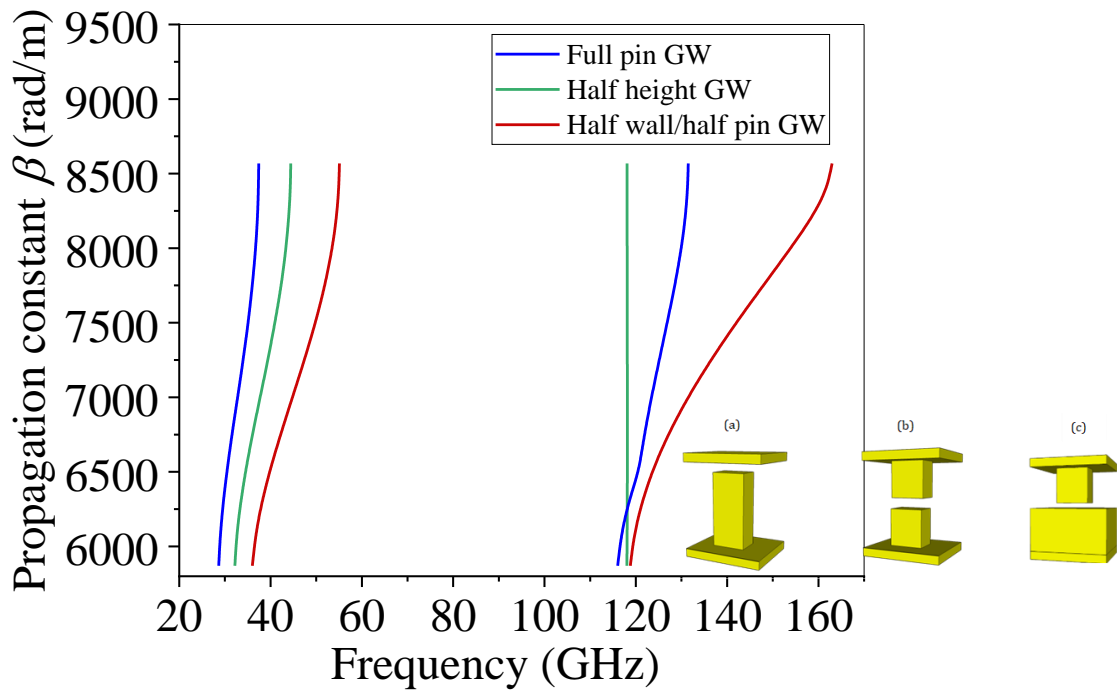
Figure 3-27: Stopband comparison of the full-pin, the half-height pin, and the half wall-half pin unit cell.

By implementing the half-height configuration of placing the gap between the pin and the walls, the half wall/half pin (HWHP) configuration may have an advantage of better confinement of the wave due to the solid metal wall on one half of the structure, as well

as faster fabrication as pins are only needed on one half of the structure while still maintaining the low aspect ratio of the pins.

A comparison of the band diagram study of the three pin structures considered is detailed in Figure 3-27, all with a gap height value of *h = 0.05* mm. The stopband generated by each seems to be relatively similar, so the selection of which pin configuration to use can be dictated by the desired application and other design and fabrication constraints.

3.7   Conclusion

Gap waveguide technology principles have been introduced to provide an understanding of the electromagnetic bandgap, or stopband generation. Several types of gap waveguide structures have been discussed, with their advantages and limitations. Gap waveguide design guidelines have been summarised, along with parametric studies of the full-pin, half-height pin and half wall/half pin unit cells for operation in the upper W-band. The parametric study on these structures demonstrates that the gap *h* plays a critical role in defining the stopband of the unit cell. In comparison, the widths of the pin *xo* and *zo* had relatively little influence on the stopband. This allowed for flexibility in selection of these dimensions based on other more critical parameters. Using a different gap waveguide pin had minimal influence on the stopband unit cell and therefore can be selected based on other design requirements. Additionally, a study on the number of the rows of lateral pins of a groove W-band waveguide was presented. Similar stopband is generated with even just one row of pins with a propagating TE_{10}-like mode, so there is flexibility in selection of the number of pin rows based on other constraints.

CHAPTER 4: GAP WAVEGUIDE-BASED SWS FOR MILLIMETRE WAVE VACUUM ELECTRON DEVICES

4.1   Introduction

Chapter 3 presented gap waveguide theory, the advantages of gap waveguide technology and initial unit cell simulations of different gap waveguides. Continuing from that, this chapter discusses in detail the design and fabrication of the gap waveguide-based slow wave structure (SWS) for W-band travelling wave tubes (TWTs). The chapter presents two novel gap waveguide-based SWS: the full pin GW-SWS (FPGW-SWS) and the half-height pin gap waveguide-based SWS (HHGW-SWS). The single section TWT design based on the HHGW-SWS is presented, where Particle-in-Cell simulations are performed to study the beam-wave interaction of the proposed TWT. The beam transportation through the TWT is also analysed. A modified version of the beam tunnel design is also presented to show the flexibility of design that the gap waveguide platform can provide. Finally, the experimental characterisation of a prototype for the HHGW-SWS is presented and compared to the simulated results.

4.2   Full pin gap waveguide-based SWS (FPGW-SWS)

4.2.1 Introduction

The rectangular corrugated waveguide SWS is a well-studied and documented structure, as shown in [62], and has been previously implemented in other electromagnetic-bandgap (EBG) structures [61]. Rectangular corrugated waveguides are simple to fabricate and for this work, the SWS implemented in the gap waveguide is adapted from the rectangular corrugation variation first presented in [63].

64

In Chapter 3, the unit cell of three types of gap waveguide pins was shown. This showed the stopband can be generated using different types of pins to be implemented as part of a SWS, namely the full pin gap waveguide-based SWS (FPGW-SWS), the half-height gap waveguide-based SWS (HHGW-SWS), and the half wall/half pin gap waveguide-based SWS (HWHP-SWS).

Chapter 3 also presented the groove gap waveguide design as the equivalent of a WR-10 waveguide using one row of pins, two rows of pins, and three rows of pins at the sides of the central channel. The results showed that, in the presence of a metal enclosure, only one row of pins was required to generate a stopband in this structure.

With these parameters in mind, two main SWSs are presented and compared – a full-pin gap waveguide (FPGW), and a half-height pin gap waveguide-based (HHGW) SWS to operate in the W-band. Starting from the stopband of the FPGW unit cell initially presented in Chapter 3, it is optimised to have a stopband of 40 - 120 GHz which adequately covers the W-band frequency range. the unit cell of the FPGW-based and HHGW-based SWS is studied in this chapter.

4.2.2   Dispersion of the FPGW-SWS mode

A wide bandwidth, good beam-wave synchronism and comparatively high interaction impedance while keeping complexity of the geometry and costs low are the specifications to be achieved in this structure. Some dimensions had a more significant impact on these results than others, which will be shown in the upcoming section.

A schematic of the FPGW-SWS is presented in Figure 4-1, dimensions shown in Table 4-1. Before starting the parametric studies and dimension optimisation, a convergence study on the propagating mode was considered where the simulations converged at a tetrahedron mesh density of 48,000, as shown in Figure 4-2.
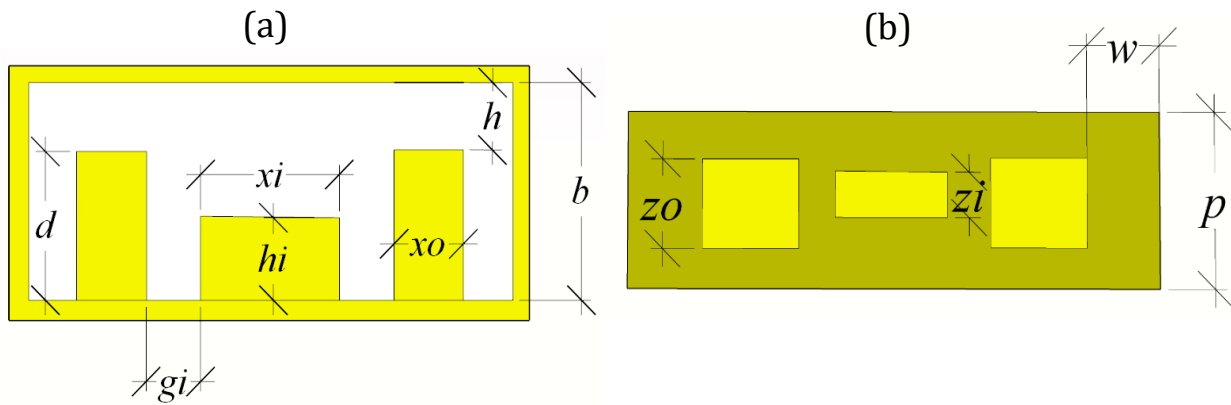
Figure 4-1:(a) Front view of the full-pin gap waveguide-based SWS (FPGW-SWS), (b) Top view of the FPGW-SWS.

Table 4-1: Dimensions for the full pin gap waveguide-based SWS (FPGW-SWS).

Parameter	Dimension (mm)
b	1.27
xi	0.6
hi	0.46
zi	0.31
xo	0.47
zo	0.58
p	1.1
gi	0.39
w	0.5
d	1.22
h	0.05
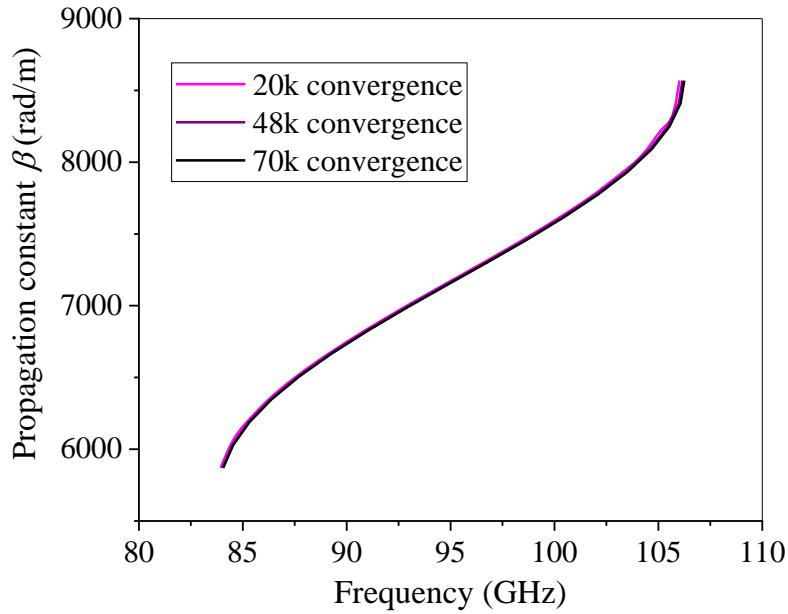
Figure 4-2: Convergence study on the propagating mode of the gap waveguide.
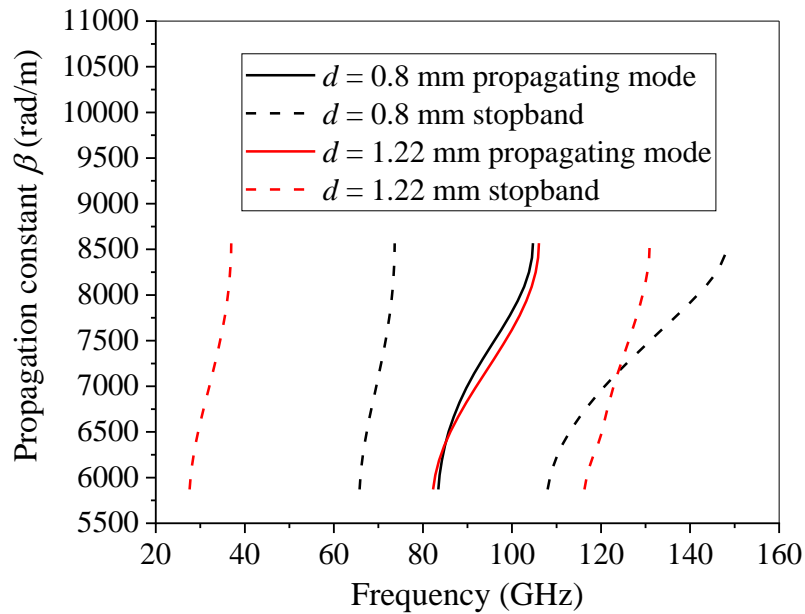
Figure 4-3: Dispersion diagram of the FPGW-SWS, showing how it varies according to the gap height and pin height, d. Other dimensions are referred to in Table 4-1.

Initially, using the design equations of the gap waveguide presented in Chapter 3, a gap of $h = 0.47$ mm was chosen, with a pin height of $d = 0.8$ mm, following the gap waveguide design guidelines of $d = \lambda/4$. As shown in Figure 4-3, this was later optimised to $d = 1.22$ mm to allow for improved beam synchronism and increased bandwidth. The other

dimensions not being studied are held constant, as with all the upcoming eigenmode simulations, shown in Table 4-1.

The hybrid mode of the FPGW-SWS is illustrated in Figure 4-4 at around 94 GHz, the central frequency point of the bandwidth. The electric field is most concentrated around the central corrugation, with minimal field located within the air gap.

(a)

(b)
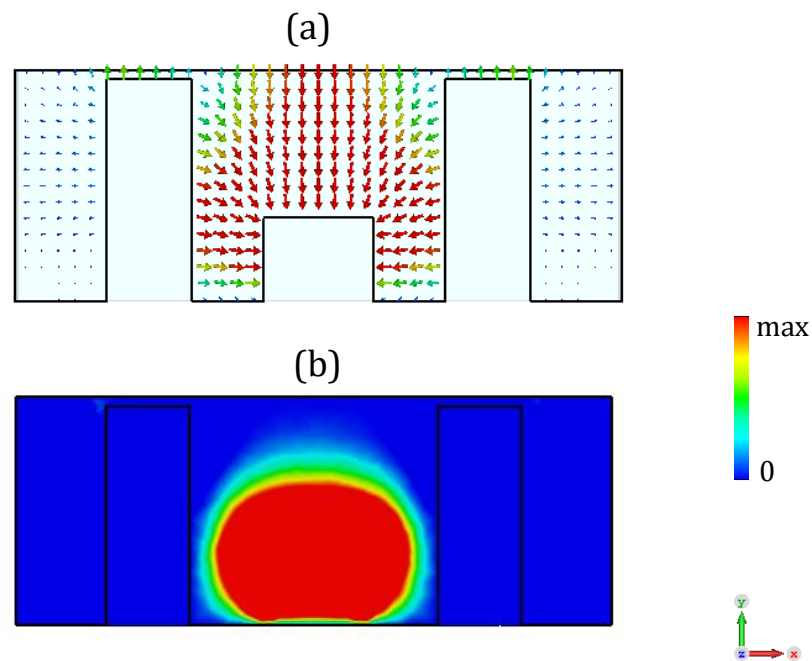
Figure 4-4: (a) Field polarisation of the FPGW-SWS at 94 GHz. (b) E_z field component.

To achieve synchronism, The phase velocity of the field needs to match the velocity of the electrons travelling above the central corrugation and along the SWS. The phase velocity of the RF signal can be converted to phase voltage to determine the synchronism of the SWS with the beam voltage. Conversion to phase voltage uses the following equation (4.1):

$$V_{p\,(kV)} = {\left(\dfrac{(V_p * c)}{593000}\right)^2}\Big/{1000} \qquad (\,4.1)$$

Where V_p is the phase velocity of the SWS, and c is the speed of light, taken as 2.99×10^8 m/s. [64]
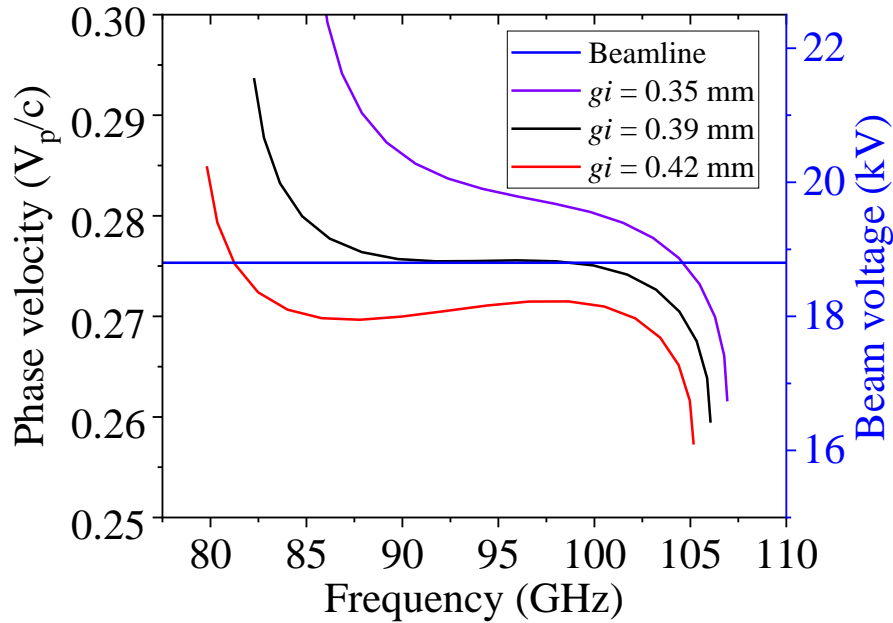
Figure 4-5: Phase velocity of the FPGW-SWS by varying the dimension *gi*. This is compared to the beamline in kV, to see which value gives the best beam synchronism. Other dimensions are referred to in Table 4-1.

Figure 4-5 shows the SWS mode dispersion in terms of normalised phase velocity variation with frequency. To achieve the best synchronism with the beam in the operation band of the TWT, a parametric study is conducted on the value *gi.* It can be noted that the phase velocity value and flatness is influenced by the gap between the corrugation and pins, *gi*. For this structure with the beam voltage set at approximately 19 kV, interaction is best for a value of *gi* = 0.39 mm at the frequencies of interest, allowing a wideband interaction of 90 – 100 GHz.

69

Further parametric simulations are conducted to study individual geometrical parameter dependence of the phase velocity of the SWS hybrid mode. Figure 4-6 shows that a larger period, p, requires higher beam voltages for synchronism and suggests a reduction in bandwidth.
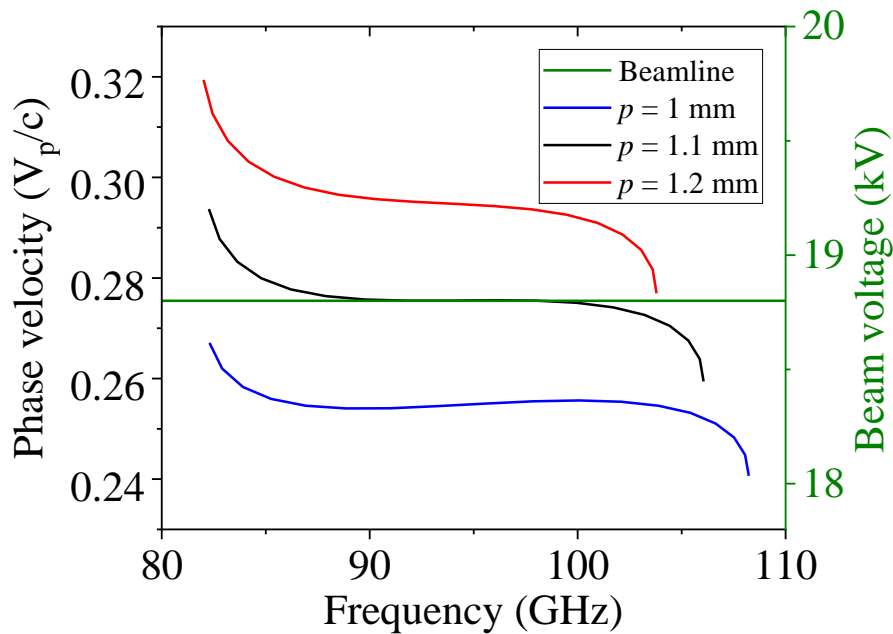
Figure 4-6: Parametric study on the phase velocity in terms of the period p for the FPGW-SWS, compared to the 19 kV beamline. Other dimensions are referred to in Table 4-1.
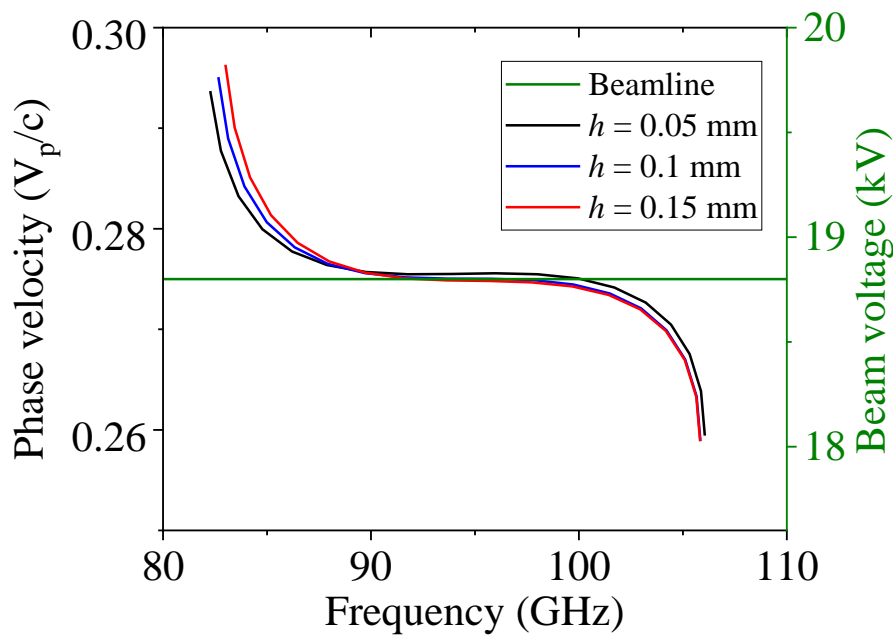
Figure 4-7: Parametric study on the phase velocity in terms of the gap h for the FPGW-SWS. This is compared to the 19 kV beamline. Other dimensions are referred to in Table 4-1.

Finally, the gap height, h, is studied in Figure 4-7. This figure suggests that a smaller gap size allows for a slightly wider bandwidth for operation. The region of synchronism is approximately 90 – 100 GHz for a value of h = 0.05 mm.

4.2.3 Interaction impedance

In this TWT design, a sheet beam is considered. The sheet beam was selected as the geometry of the sheet beam is more suitably shaped for the area which the electric field is generated by the corrugated waveguide.

Sheet beam instability must be accounted for when being transported along the length of the TWT, namely Diocotron instability. This refers to the effect of sheet beam electrons shifting until the beam loses its shape as it travels along the length of a tube. Due to diocotron instability, which is influenced by the $E \times B$ velocity drift, where E is the transverse space charge field, and B is the magnetic field strength [65], [66], curling of the edges of the beam can cause substantial loss of gain, as well as collision of electrons to the structure. Figure 4-8 captures this effect. Sheet beams typically require a stronger magnetic focusing system to properly confine it. Using the equation (4.2) in [67], the uniform magnetic field to confine the sheet beam can be calculated to where Diocotron instability does not occur.

$$L > 800\gamma^3 \beta_z^2 \frac{B}{J} \tag{4.2}$$

Where L(cm) is the total interaction circuit length, $\gamma = (1 - \beta_z^2)^{-1/2}$ is the relativistic energy parameter, and $\beta_z = v_z/c$ which is the axial beam velocity normalised to the speed of light in a vacuum. J(A cm^{-2}) is the beam current density, and B(kG) is the magnetic field intensity [68].

71

Proposed in [63], rather than having sharp beam corners, the design of a rounded beam corner could reduce the gain loss as well as the electron drift. A radius of 0.1 mm is used to round the corners of the selected beam when calculating the average interaction impedance and running the particle-in-cell (PIC) simulations. Practically, the sheet beam realised will have slightly rounded edges and so it is beneficial to take it into account during simulation.
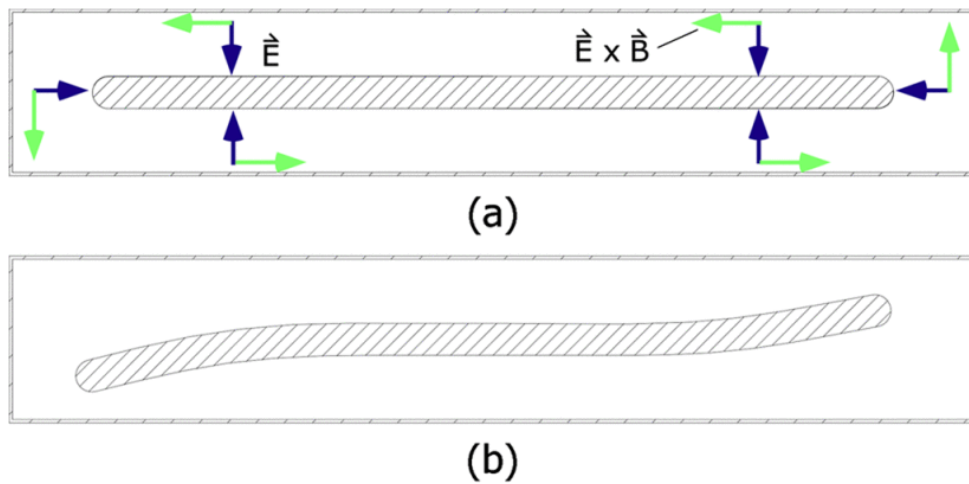
Figure 4-8: Sheet beam electron drift. [66]

With the parameters of the sheet beam set, the interaction impedance can be calculated for a specific beam aspect ratio. The interaction impedance is an approximate figure of merit to estimate how effectively the beam and the SWS mode longitudinal electric field interact with one another. The mathematical equations for determining the local interaction impedance are presented in Chapter 2. In essence, interaction impedance K is calculated in (4.3) as:

$$K = \frac{|E_{z(n)}|^2}{2\beta_{(n)}^2 P} \tag{4.3}$$

The typical value for rectangular corrugated SWSs in the 80-300 GHz range is around 1 Ω [62]. The average interaction impedance is here calculated on the assumption of a 1

72

mm x 0.2 mm sheet beam, situated σ = 0.08 mm above the central corrugation, by taking an average of discretized points across the beam cross-section. The schematic and cross section of the beam in the SWS is shown in Figure 4-9. In all instances, the local interaction impedance refers to the centre of the beam at the height of the beam gap betweent the corrugation (x, y = 0, 0.08).
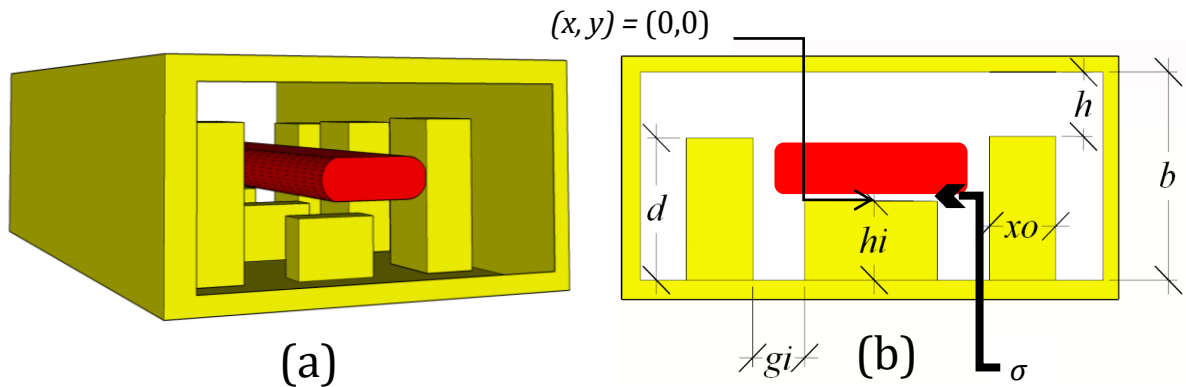
Figure 4-9: (a) Perspective view of the placement of the beam in the FPGW-SWS. (b) cross sectional view of the beam placement in the FPGW-SWS.

The local interaction impedance parametric study shows the comparison between different values of gi and p in Figure 4-10 and Figure 4-11 respectively. The interaction impedance is calculated using a 1 mm x 0.2 mm sheet beam, situated σ = 0.08 mm above the central corrugation for different values of gi. Figure 4-10 shows that minimal change occurs when reducing gi, while increasing it beyond gi = 0.39 mm shifts the frequency band and slightly reduces the interaction impedance.
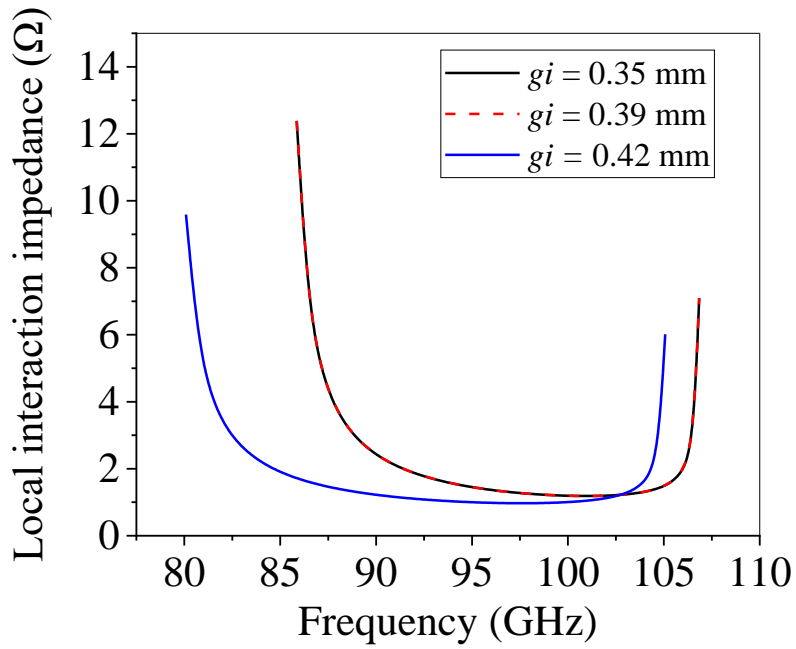
Figure 4-10: Parametric study on the local interaction impedance for the FPGW-SWS, varying the value *gi.* Other dimensions are referred to in Table 4-1.
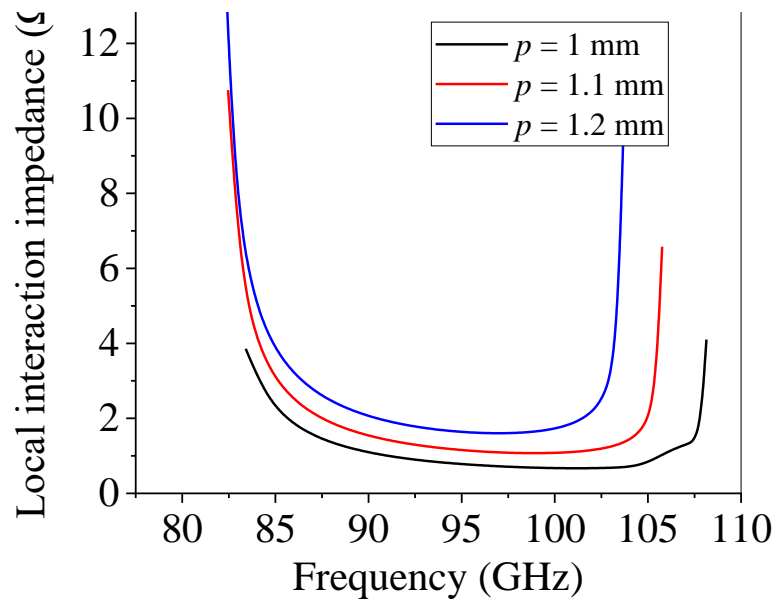
Figure 4-11: Parametric study on the local interaction impedance for the FPGW-SWS, varying the value *p*. Other dimensions are referred to in Table 4-1.

Figure 4-11 shows that increasing *p* can increase the interaction impedance but also reduces the bandwidth.

As a reference, the average interaction impedance of the same corrugated waveguide when simulated within conventional metal walls, is found to be approximately 0.5 Ohm. Comparing the FPGW-SWS to the reference SWS with metal walls, shows that the interaction impedance remains unaffected by the introduction of the gap waveguide arrangement, compared in Figure 4-12.
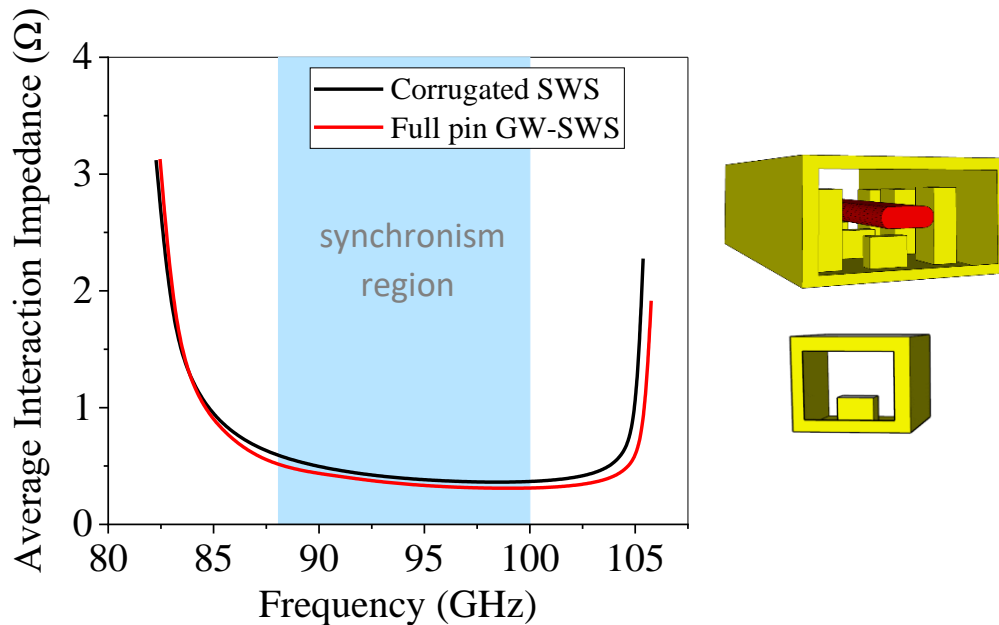
Figure 4-12: Average interaction impedance of FPGW-SWS
compared to corrugated SWS.

4.2.4 SWS Coupler design

In the design of a TWT, the coupler matches the SWS input and output ports to that of a standard waveguide, in this case the WR-10, to be able to feed and collect the input/output RF signal to/from the TWT. The coupler includes a beam tunnel to allow for the beam to travel through the SWS and interact with the electric field to amplify the RF signal.

To design correct input/output coupling to the SWS, several sections are required. First, the designed central corrugations of the SWS must be tapered gradually to the standard waveguide port to convert the fundamental mode in input (TE_{10}) to the SWS hybrid mode

with minimum reflections of the input signal (S_{11}). The tapering must also be compact, while still feasible in terms of fabrication.

Second, the gap-waveguide integrated bend is a critical section in providing good scattering parameters of the coupler. The placement of the pins proved to be very critical in this sense and required careful consideration in their placement.

Third, the beam tunnel must be integrated to ensure enough space for the beam to pass through without collision to the structure which would thus cause a loss in interaction and damage to the pins. Moreover, the beam tunnel should not permit coupling from the RF signal. An easy choice for the beam tunnel width is to have this dimension below the cut-off frequency of the input signal which avoids transmission and consequent loss of the signal within the beam tunnel. However, this poses a limitation on the wide dimension of the sheet beam to be used, and thus its aspect ratio, especially when the frequency of operation increases. Such a limitation can be overcome by integrating the beam tunnel design within the gap waveguide platform, which will be shown in Section 4.3.4.

Fourth, the conductivity of the material for the coupler must be considered. Typically, copper is used for the development of TWTs due to its high electrical conductivity and thermal properties. Ohmic losses caused by surface roughness introduced from machining however can effectively reduce the output power. This effect can be introduced in simulation by modelling the copper material with a reduced conductivity to mimic the losses due to surface finishing in transmission (S_{21}) on the structure.

Finally, the number of periods of the interaction section must be considered. A shorter version of the SWS is used for the baseline coupler design, fabrication, and cold test measurements (10 periods). For the full TWT design, a much larger number of periods are used to allow for gain to be established.

76

4.2.5   Back-to-back coupler design

 The coupler section includes a taper in height for the central corrugation and a lateral taper for the side pins. The first type of taper enables the conversion between the TE_{10} mode injected at the input into the hybrid mode supported by the SWS while the second widens the groove width between the pins to match standard dimensions of the WR-10 standard W-band waveguide. The full pin back-to-back GW-SWS prototype consists of 10 periods for the propagating section, and 20 periods of tapering section on each side of the couplers, shown in Figure 4-13.

W-band sections

Propagating sections

Tapering sections
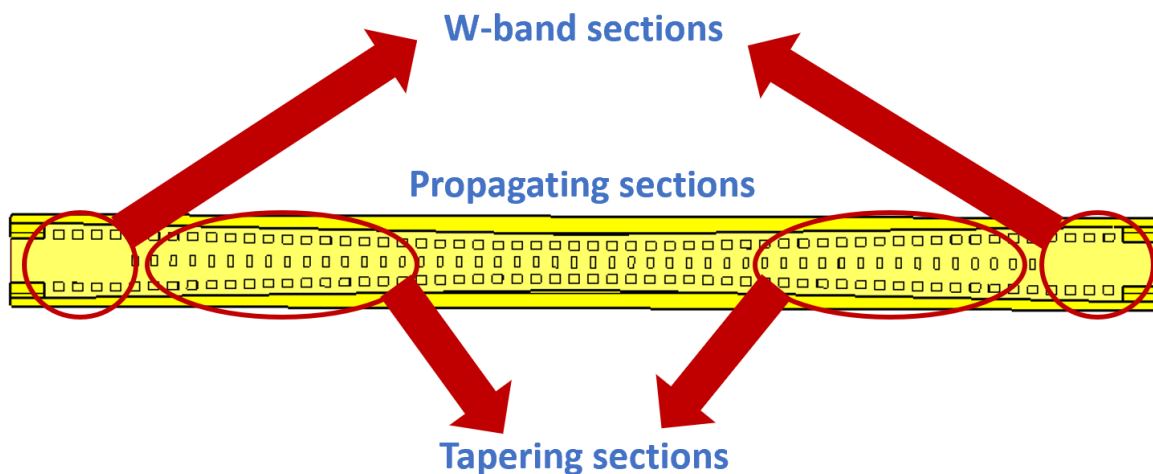
Figure 4-13: Top view of the back-to-back FPGW-SWS coupler.

Numerical simulations of the scattering parameters were initially conducted in the time domain package of CST to limit the computational running time of the simulations in the initial design phase. The number of hexahedral mesh cells required for numerical accuracy are shown in Figure 4-14, showing the convergence of the structure occurring at 11 million meshcells. In the final phase of the design optimisation, the simulations were conducted in the frequency domain package of CST, for refined accuracy. The convergence of the frequency domain simulations is considered in Figure 4-15, built off the number of cells per wavelength used in the time domain mesh settings. The mesh cells

in the frequency domain are tetrahedral and convergence is reached at 350,000 meshcells.

Figure 4-16 shows a study on the number of periods required for the taper sections. It was found that a minimum number of 20 periods were required for the tapering to adequately reduce the reflections in the final design. This figure used the ideal conductivity of copper ($\sigma = 5.96 \times 10^7$ S/m).
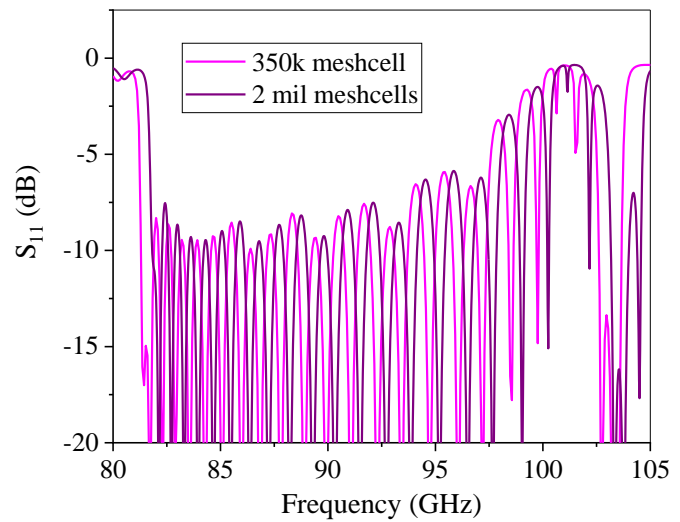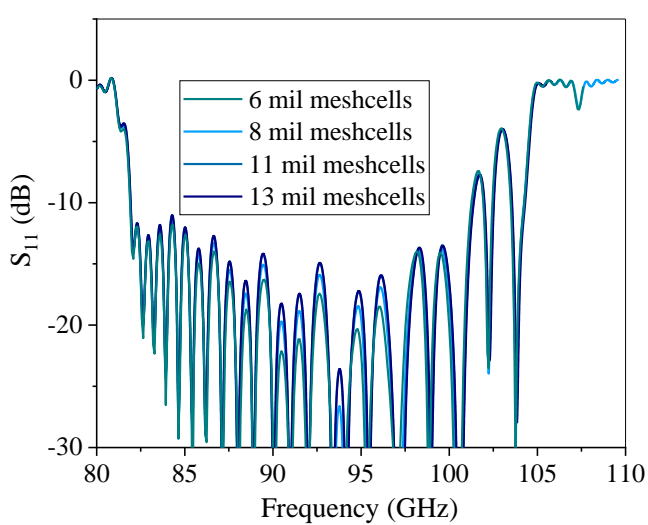
Figure 4-14: Convergence study on the scattering parameters in the time domain.

Figure 4-15: Convergence study on the scattering parameters in the frequency domain.
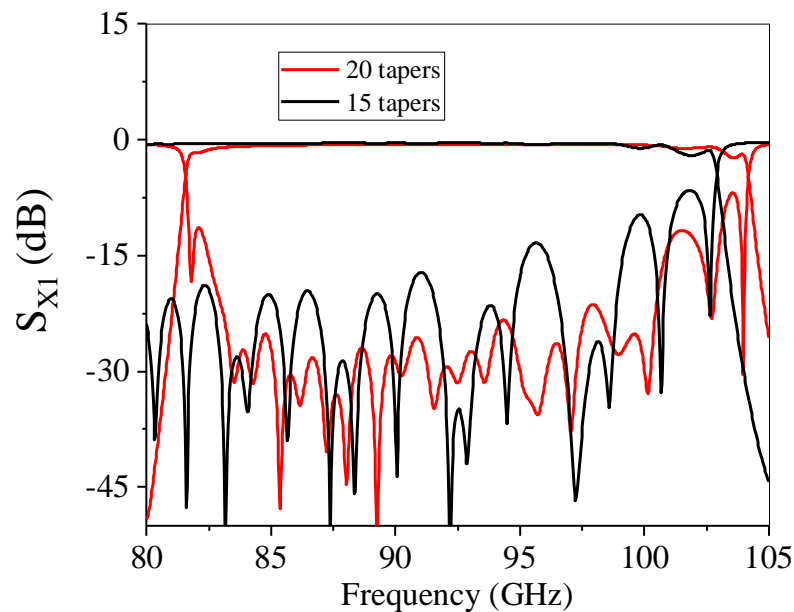
Figure 4-16: Parametric study on the number of tapers required for the coupler for the back-to-back FPGW-SWS.

78

4.2.6 Final coupler design

The bend of the coupler facilitates the beam tunnel to allow passage of the beam, as well as housing the input and output ports to couple to the standard WR-10 waveguide flanges. The schematic of the FPGW-SWS coupler bend is shown in Figure 4-17. The half height pins are required to be used around the beam tunnel to allow the beam passage, as simply shortening the full pin did not adequately reduce reflections. Pins around the beam tunnel are locally modified in height to allow passage of the beam tunnel. The periods of the pins are also modified to shift the frequency band of operation. The width of the inner corner pin is increased to reduce reflections. The details of these changes are depicted in Figure 4-17 and Table 4-2 respectively. The corner pins consist of two pairs of pins with a gap of go = 0.35 mm and a pair of pins with a gap of gh = 0.51 mm. The other pin modification is zh = 0.895 mm.
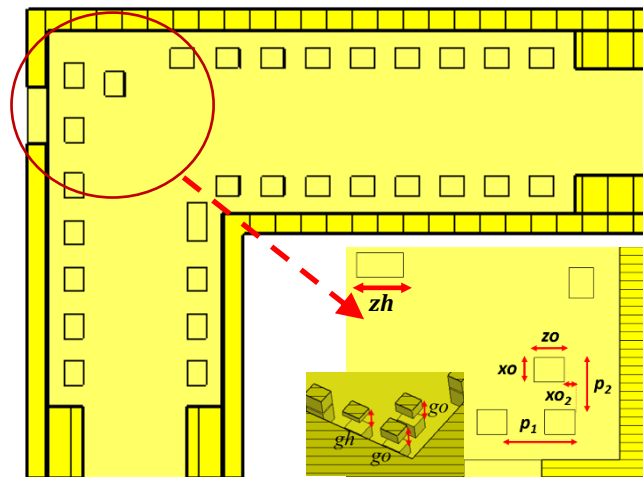
Figure 4-17: Coupler bend design.
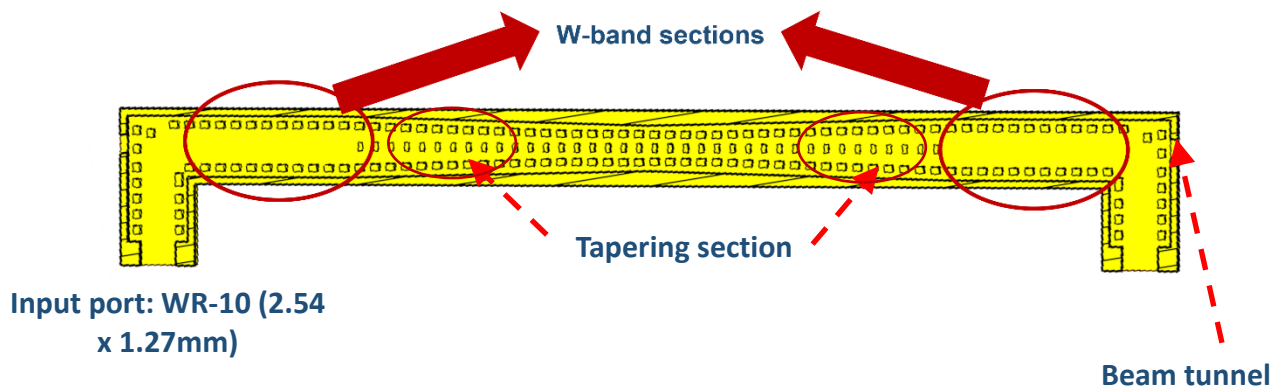
Figure 4-18: Top view of the FPGW-SWS coupler.

Table 4-2: Coupler bend parameters.

Parameter	Dimension (mm)
xo	0.47
xo_2	0.2
zo	0.58
go	0.35
gh	0.51
zh	0.895
p_1	1.3
p_2	1

The complete input/output coupler, including the waveguide 90-degree bend and beam tunnel is then considered in simulation. The use of the pins in this structure allows for the seamless transition using 90-degree bends, which allows for a more compact design.

Figure 4-18 demonstrates the full pin coupler, with the "W-band" waveguide section and the tapering section highlighted. 16 periods of the W-band waveguide section are used on each side of the structure (2.54 x 1.27 mm), before transitioning into the bend. The parametric study on the number of W-band periods is shown in Figure 4-19, indicating that a minimum of 16 periods are needed to taper the coupler while keeping the reflections low.
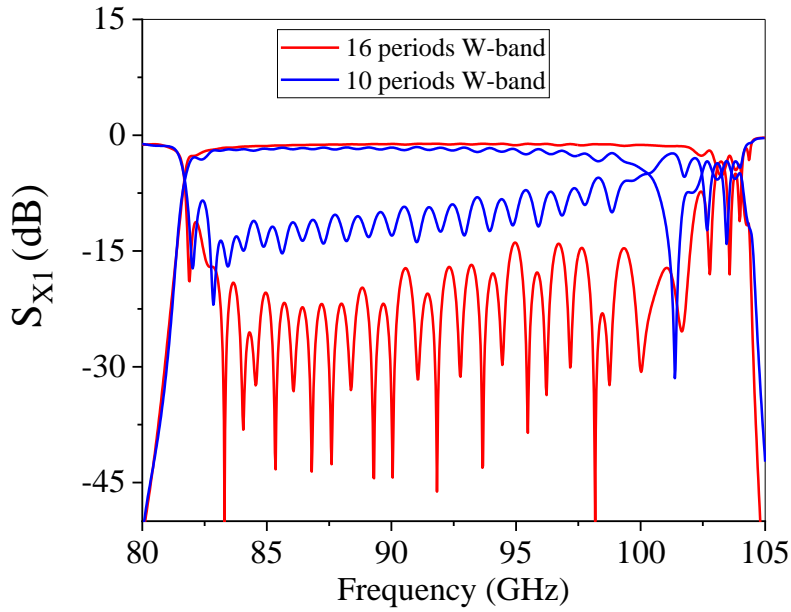
Figure 4-19: Parametric study on the number of w-band periods, showing the scattering parameters of the FPGW-SWS for the full coupler.

The metal walls of the enclosure are also tapered to keep the lateral distance between pin and wall, *w*. It was found that *w* has no effect on the dispersion or scattering parameters of the structure, so this value was set to *w* = 0.5 mm for easier fabrication, which will be further discussed in Section 4.5. The transmission is computed using reduced copper conductivity (σ = 2.89 x 10^7 S/m) in Figure 4-19. The final region of transmission is shown to be 82 – 103 GHz.

4.3   Half height pin gap waveguide-based SWS (HHGW-SWS)

4.3.1   Dispersion of the HHGW-SWS mode optimisation

The advantages of the half-height pin with respect the full pin arrangement and other pin-based structure such as photonic crystals, as discussed in Chapter 3, are the lower aspect-ratio and lower height of the individual pins which allow for a simpler fabrication. Derived from similar dimensions of the FPGW-SWS, the half-height pin gap waveguide-based SWS (HHGW-SWS) is presented in Figure 4-20, with the dimensions show in Table 4-3.
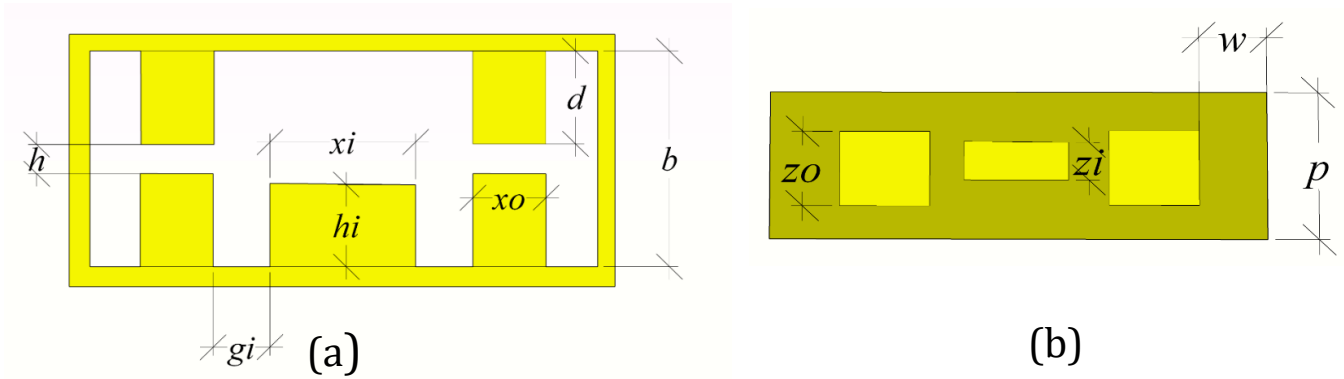
Figure 4-20: (a) Front view of the half-height gap waveguide-based SWS (HHGW-SWS).
(b) Top view of the HHGW-SWS.

Table 4-3: Parameters for the HHGW-SWS.

Parameter	Dimension (mm)
b	1.27
xi	0.6
hi	0.46
zi	0.31
xo	0.47
zo	0.58
p	1.1
gi	0.42
w	0.5
d	0.61
h	0.05
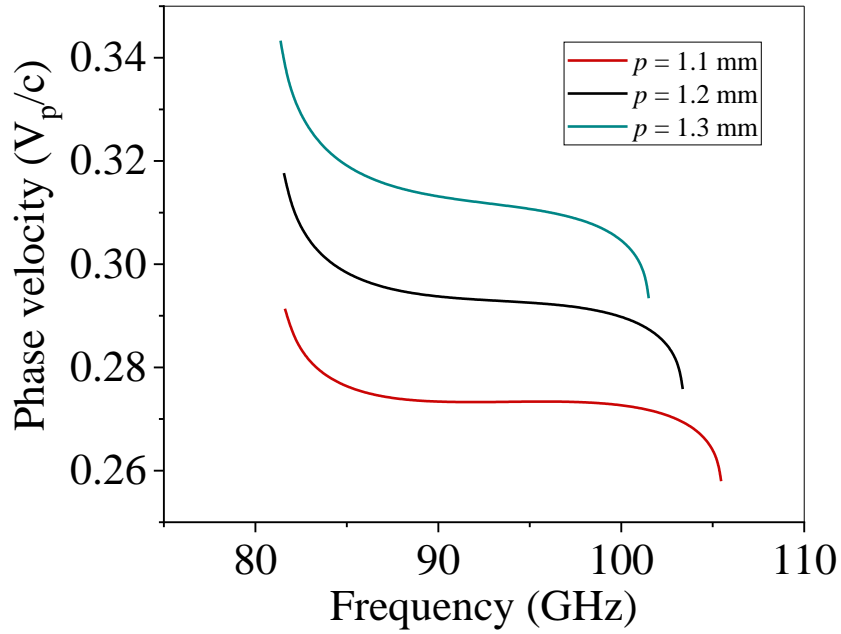
Figure 4-21: Parametric study on the phase velocity of the
HHGW-SWS in terms of the period.

A parametric study on the HHGW-SWS shows the impact of the period p on the phase velocity, in Figure 4-21. It confirms that the choice of period for the HHGW-SWS p = 1.1 mm can keep the phase velocity curve flat in a broad region of frequency and low enough to interact with a beam voltage of < 20 kV.
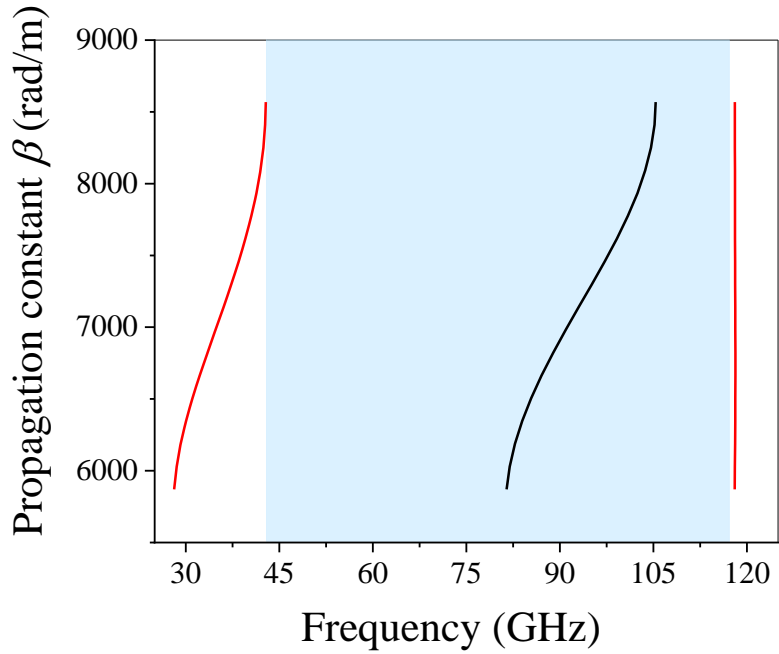
Figure 4-22: Dispersion diagram of the half height gap waveguide-based SWS. (HHGW-SWS). The stopband region is shaded.
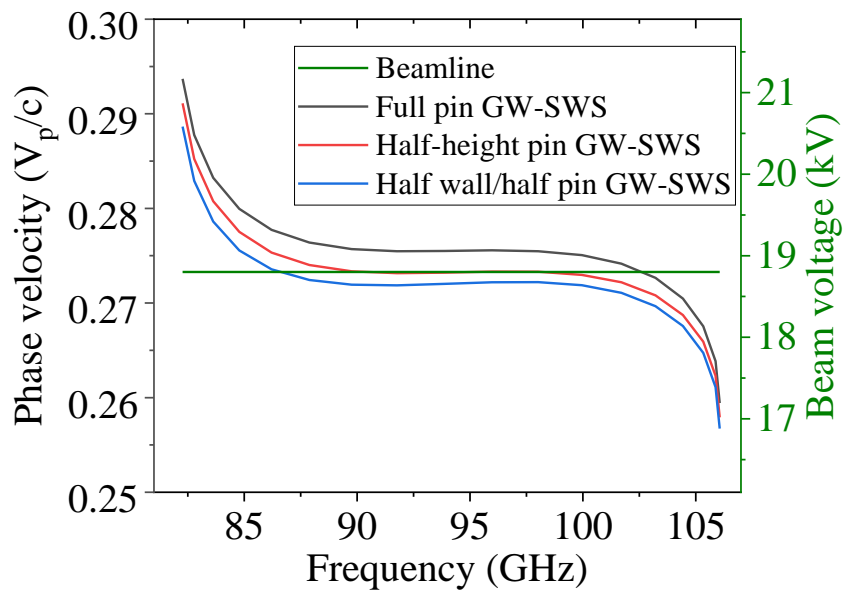
Figure 4-23: Comparison of the phase velocity of the full pin, the half-height pin, and the half wall/half pin gap waveguide, including the 19 kV beamline.
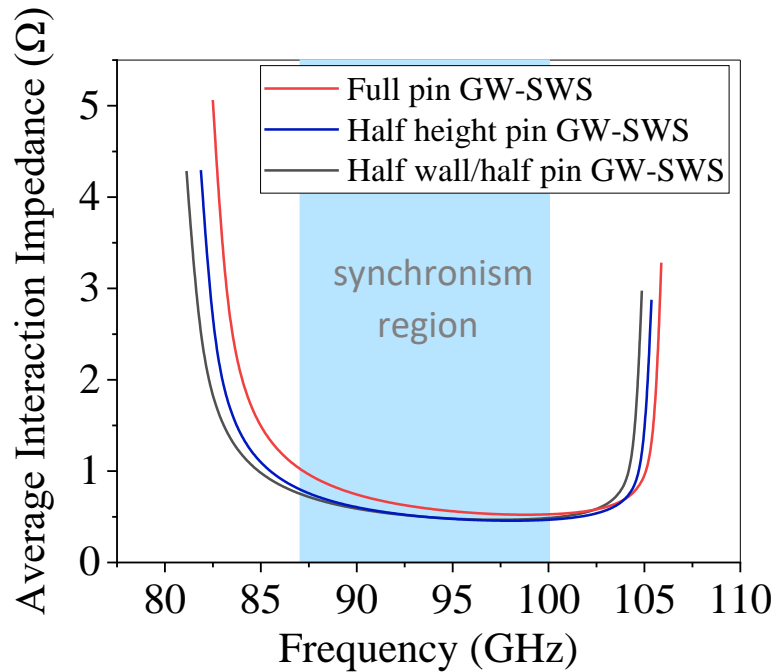
Figure 4-24: Comparison of the interaction impedance of the full pin, the half-height pin, and the half wall/half pin gap waveguide for a 1 x 0.2 mm sheet beam, situated 0.08 mm above the corrugation.

The band diagram for the HHGW-SWS unit cell study is shown in Figure 4-22 where the stopband edges are represented in red, and the SWS mode dispersion is shown in black. The dispersion of this structure is from 83 to 105 GHz. For reference, a comparison of the HHGW-SWS to two other pins simulated in Chapter 3, with the addition of the rectangular corrugated waveguide to create the SWS. This includes the half-wall/half pin gap waveguide-based SWS (HWHP-SWS) and the FPGW-SWS. Figure 4-23 and Figure 4-24 show the comparison of all three pin forms in terms of the SWS beam synchronism and average interaction impedance. As with the full pin structure, the beam synchronism is very sensitive to the value gi. To keep the phase velocity flat for each pin configuration of the SWS, gi is modified slightly in each case. For the full pin, gi = 0.39 mm. For the half-height pin, gi = 0.42 mm. For the half-wall pin, gi = 0.455 mm. All other parameters are kept the same as shown in Table 4-3.

Compared to the FPGW-SWS, the HWHP-SWS gives a slightly lower phase velocity than the other structures, which is advantageous for having a lower beam voltage. The HWHP-SWS has the benefit of faster fabrication as only one half of the SWS needs pins to be machined. However, the configuration of the coupler would need to be changed and flexibility of its design would be limited without the pin's arrangement on both parts of the SWS. While the FPGW-SWS and the HHGW-SWS provide similar dispersion characteristics, the HHGW-SWS showed some additional advantages. First, thanks to the reduced aspect ratio and height of the pins, they are less susceptible to snapping or bending during the fabrication process. Second, which will be shown in Section 4.3.3, a more compact coupler can be realised compared to the FPGW-SWS while maintaining good scattering parameters. The e-field distribution of the hybrid mode of the HHGW-SWS is illustrated in Figure 4-25 at around 94 GHz, the central frequency point of the predicted TWT bandwidth. The electric field is most concentrated around the central corrugation, with minimal field located within the air gap. The potential for vacuum breakdown due to excess concentration of electric field [69], is minimal, due to low concentration of the electric field in the gap.

(a)

(b)
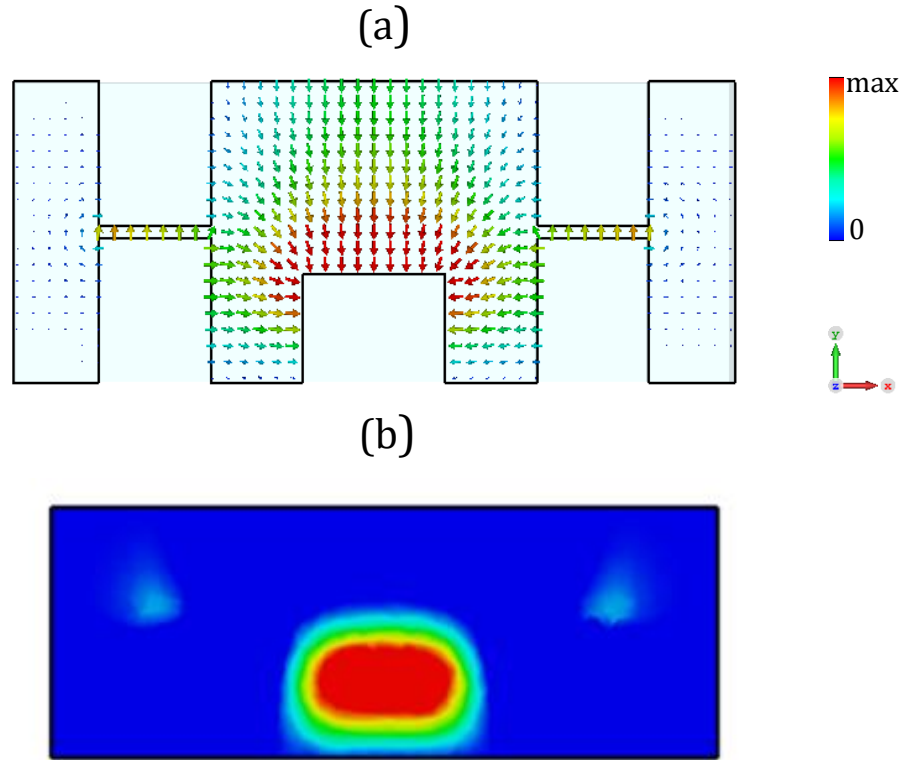
Figure 4-25: (a) Field polarisation of the HHGW-SWS hybrid mode at 93 GHz. (b) E_z field component.

4.3.2   Comparison with the conventional corrugated waveguide

The equation (4.1) from the beam voltage can be rearranged to plot the beam-wave synchronism in terms of the mode frequency-phase plot rather than the phase velocity, as seen in Figure 4-26. Viewing the mode dispersion in this way can show how the beam synchronises while considering the space harmonic of interaction. The space harmonic where the beam interacts for both the FPGW-SWS and the HHGW-SWS is the 1st space harmonic. To demonstrate this, the phase shift is normalized, as shown in (4.4):

$$Normalised\ phase = \frac{Phase(degrees)}{180}$$ (4.4)

The beam line corresponding to a certain voltage can be overlapped to estimate beam-wave synchronism using (4.5):

$$Beamline(kV) = \left(\frac{V_e * Normalised\ phase}{2 * period(metres)}\right) * 0.000000001 \qquad (4.5)$$

Where V_e, the electron velocity, is:

$$V_e = 593000 * \sqrt{Beam\ voltage(Volts)} \qquad (4.6)$$
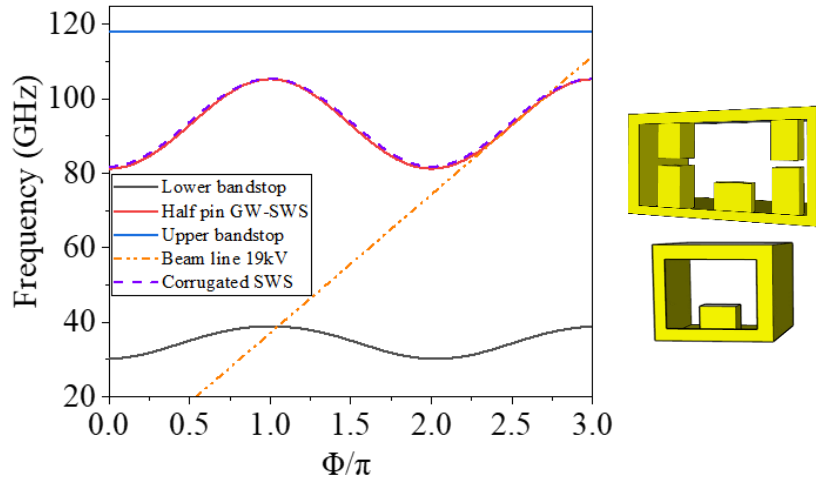
Figure 4-26: Dispersion characteristic of the HHGW-SWS mode compared to that of the conventional corrugated WG. The upper and lower edges of the HHGW stopband are shown.
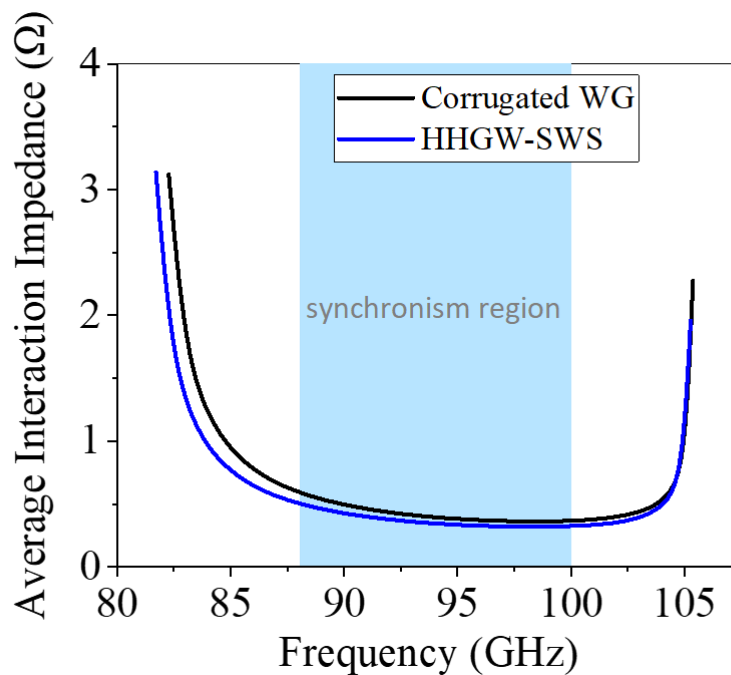
Figure 4-27: Average coupling impedance for the HHGW-SWS and the conventional corrugated WG. The shaded area represents the estimated region of synchronism in the 86-100 GHz range.

Using the sheet beam of 1 x 0.2 mm, placed at 0.08 mm above the corrugation, the average interaction impedance of the HHGW-SWS is found to be similar to the one calculated for the FPGW-SWS. Figure 4-27 shows the comparison of the average interaction impedance for the HHGW-SWS and the corrugated waveguide SWS with metal walls. This shows that the use of these different pin structures replacing the conventional metal walls has little effect on the interaction impedance of the SWS. Therefore, the pin structure selection will depend on other considerations, mainly on fabrication aspects and SWS coupler design as it will be shown in the following sections.

4.3.3   Coupler design

The optimised SWS coupler design for the HHGW, including the gap waveguide 90-degree bend, is detailed in Figure 4-28, where parameters are shown in Table 4-4. For the majority of the pins, the same dimensions are used in that of the interaction section. Minimising reflections by correct placement needs to be considered while also allowing beam passage. Additionally, the inner corner pillars were chamfered at a 45° angle on the corner at c_1 = 0.3 mm, and c_2 = 0.2 mm respectively, for easier fabrication, as will be discussed in Section 4.5.
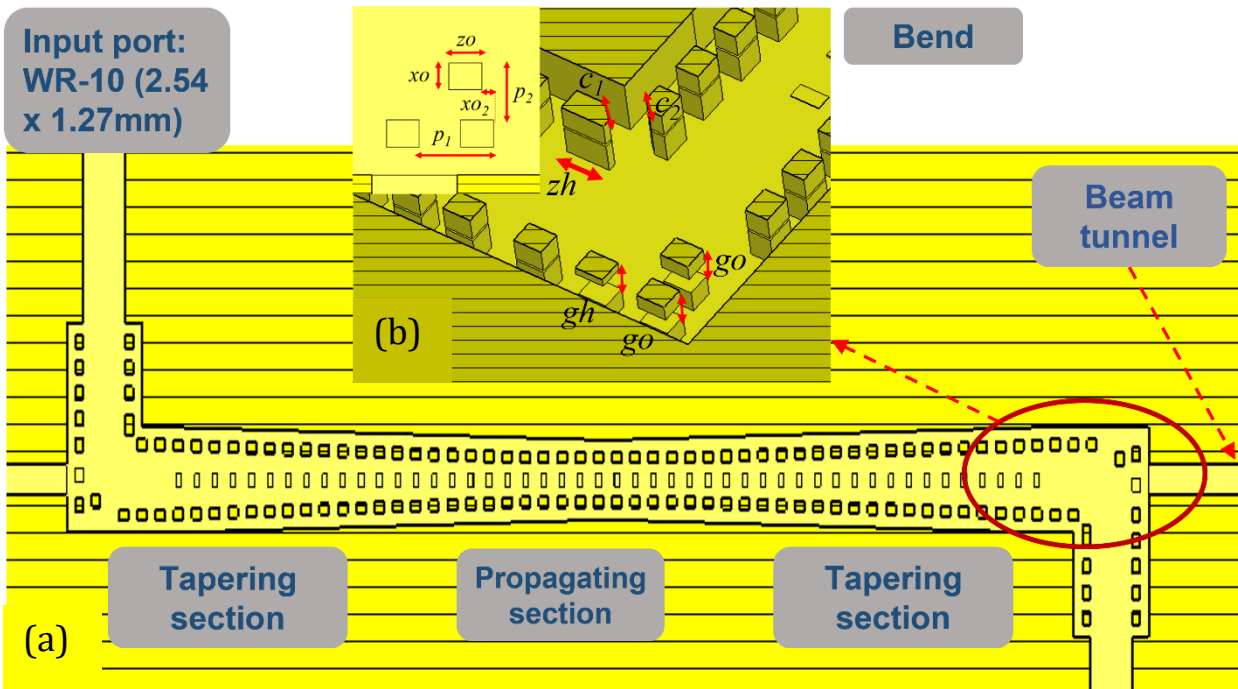
Figure 4-28: Schematic of the complete HHGW-SWS (10 periods of the interaction section). (a) Bottom half top section view. (b) Close-up of coupler 90-degree bend.

Table 4-4: Parameters of the HHGW-SWS coupler bend.

Parameter	Dimension (mm)
xo	0.47
xo_2	0.2
zo	0.58
go	0.35
gh	0.51
zh	0.895
p_1	1.3
p_2	1
c_1	0.3
c_2	0.2

The maximum size of the beam tunnel height was found to be 0.51 mm due to constraints by the gap size of the surrounding pins, which would cause an increase in reflections with a larger gap. The final designed beam tunnel was 1.3 x 0.51 mm.
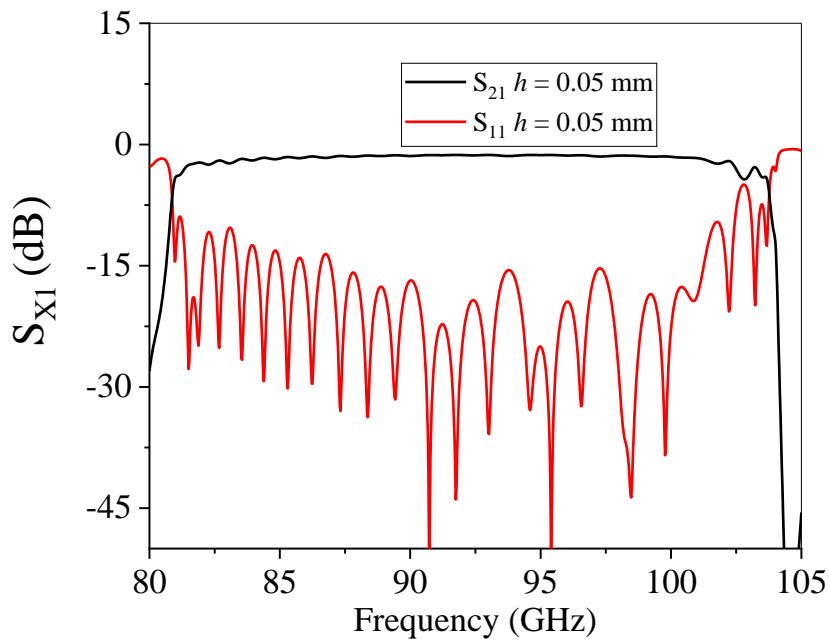
Figure 4-29: The scattering parameters of the full coupler for the HHGW-SWS.

As with the full pin structure, a 10-period interaction section and a 20-period tapering section on each side was used. Reducing the tapering section to less than 20 periods caused increased reflections, as with the full pin coupler. However, unlike the full pin coupler, using additional periods of the W-band gap waveguide at the end of the tapering sections was not necessary, as it provided an S_{11} of -15 to -18 dB without this additional section. Hence, the half-height pin coupler could make a more compact structure by reducing the overall SWS length. Figure 4-29 shows the s-parameters of the HHGW-SWS at reduced conductivity of copper $\sigma = 2.89 \times 10^7$ S/m. S_{21} is found around -1 dB for 10 interaction periods, while reflections are less than -15 dB in the bandwidth 84 – 102 GHz.

In an actual TWT, many more than 10 periods are used in the interaction section. For a single-section TWT, anywhere from 80-110 periods are used to allow gain saturation. In this case, a trade-off must be considered in terms of number of periods for sufficient beam-wave interaction (gain), while the length of the SWS is kept to the minimum to facilitate sheet beam transportation and minimise footprint. Section 4.4 goes into more

detail for the gain and beam transportation, but the results of the simulated S-parameters of the full-length SWS is reported here for completeness. A 90-period length of the interaction section for the SWS provided a transmission loss of -4 dB with reduced electric conductivity of copper in the bandwidth 82 – 103 GHz. (Figure 4-30).
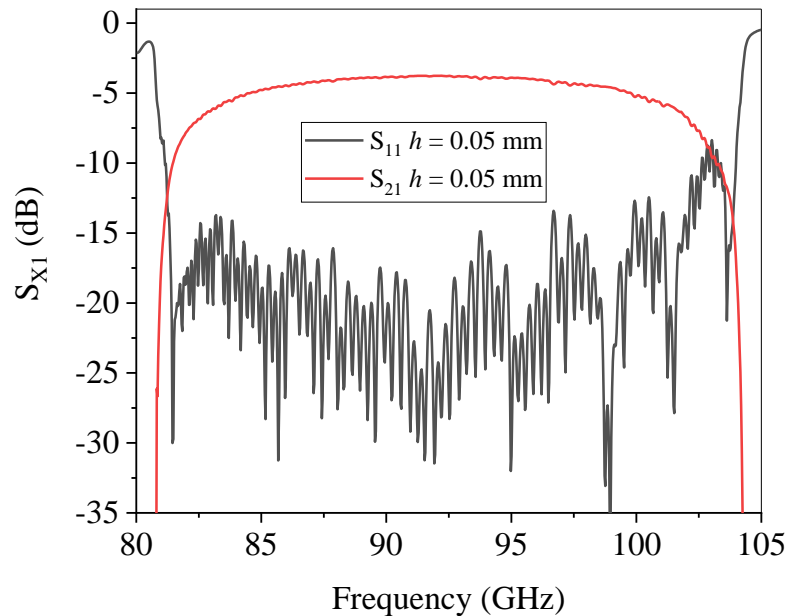
Figure 4-30: S-parameters for the HHGW-SWS 90-period TWT simulated with a reduced copper conductivity of $\sigma = 2.89 \times 10^7$ S/m.

4.3.4   Coupler design for large aspect ratio sheet beam

As the beam tunnel width of the original design (1.3 mm x 0.51 mm) is below half the length of the wavelength, the cut-off for any mode transmission within the beam tunnel is achieved and no leakage of the wave in the tunnel occurs. While the designed beam tunnel size is adequate for the designed structure and beam, at the increase of sheet beam width (aspect ratio) and frequency of operation, the probability of the tunnel beam dimension becoming above the cut-off becomes more likely. It was demonstrated in [61] that the stopband property of periodic structures with the use of Photonic crystals can be exploited to ease the design of the beam tunnel for wide sheet beams and overcome this

92

issue. As a proof of concept, this is also applied to the presented HHGW-SWS design where a beam tunnel suitable to different beam sizes is considered here. The gap waveguide can be used to the advantage of integrating a beam tunnel with a width larger than cut-off wavelength by adding carefully placed pins in the beam tunnel. The pins then generate the forbidden frequency range which the mode propagates in, thus confining the wave and not allowing transmission within the beam tunnel to occur. When the beam tunnel width is more than half the wavelength, transmission of the propagating mode can occur within the beam tunnel, thus causing losses in transmission from the input to the output port of the TWT. In this case, the central frequency of 93.5 GHz is taken. This gives a wavelength of 3.2 mm, and a maximum beam tunnel width of 1.6 mm. The effects of transmission loss and higher reflections is seen beyond 1.6 mm in this structure.

Initially the stopband of the beam tunnel pins is simulated in an eigenmode simulation, optimised using previous parametric studies to realise the required stopband. The schematic in Figure 4-31 and Table 4-5 shows the final design of the beam tunnel pins and the respective dimensions, with the resulting stopband shown in Figure 4-32. The pins are then placed in the beam tunnel (2 x 0.51 mm) of the coupler bend to verify the transmission and reflections characteristics, as seen in Figure 4-33.
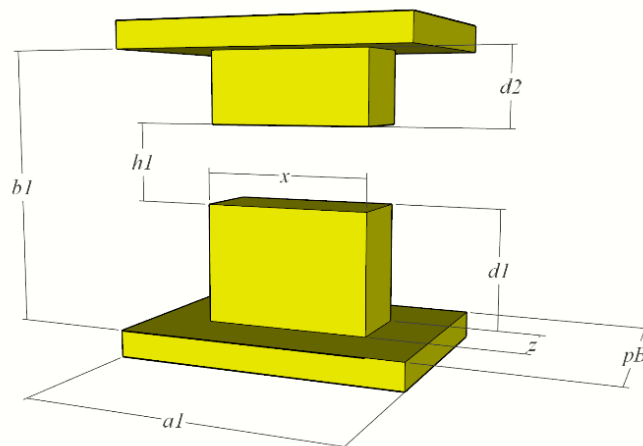
Figure 4-31: The unit cell study of the beam tunnel pin.

Table 4-5: Parameters of the unit cell for the beam tunnel pins.

Parameter	Dimension (*mm*)
b1	1.27
a1	2
x	0.99
z	0.47
d1	0.46
d2	0.3
h1	0.51
pB	1.7

The SWS propagating mode ranges between 79 and 104 GHz, and so the pins need to be designed to block this range of frequencies. To demonstrate this concept, a beam tunnel width of 2 mm is selected as port transmission occurs at this point because the width is above the cut-off frequency of the wavelength. The optimised pins generate a stopband in the range of 77.5 to 120 GHz, adequately covering the required frequency range. This allows for a much wider beam tunnel width beyond the cut-off limit of 1.6 mm. This brings the original beam tunnel size from 1.3 x 0.51 mm to 2 x 0.51 mm. The height of the beam tunnel is still relatively restricted, due to the gap size of the inner beam tunnel pins (within the bend) being no greater than 0.51 mm.
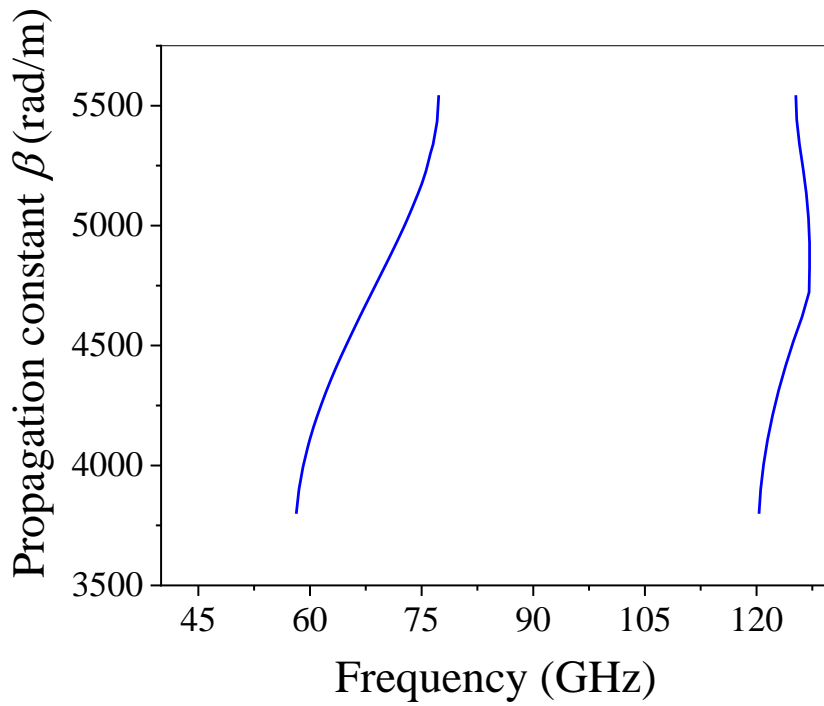
Figure 4-32: The stopband generated by the beam tunnel pin.
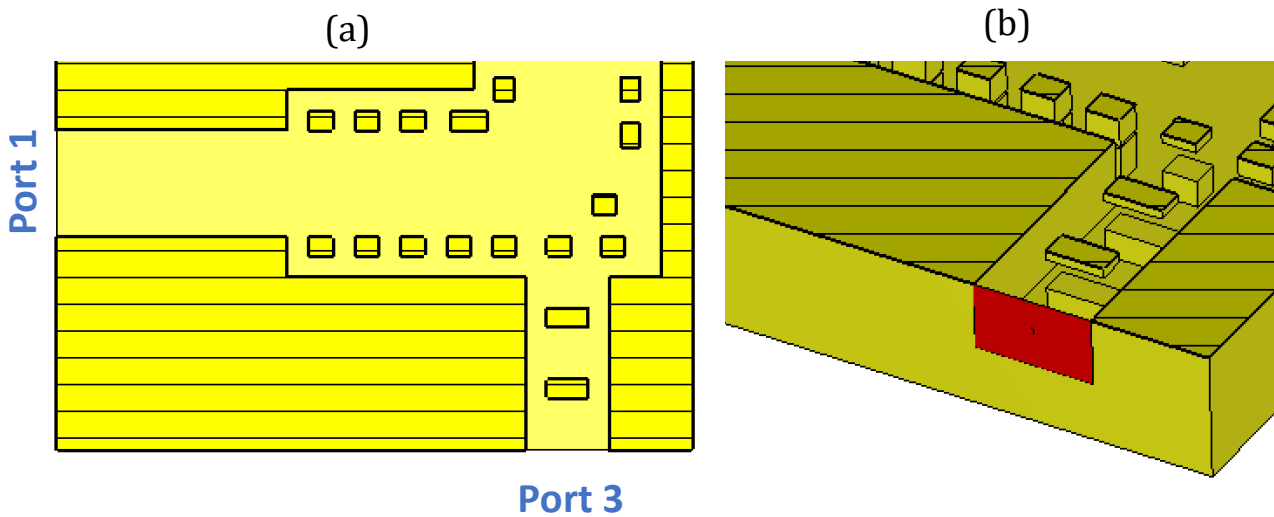
Figure 4-33: (a) Top view of the bend with the modified beam tunnel. (b) Perspective view of the beam tunnel pins placed within the HHGW-SWS coupler.

S_{11} of the bend with the beam tunnel pins returned a good value of less than -18 dB for

the desired frequency range in Figure 4-34. The transmission from the beam tunnel (port

3) to port 1 (S_{31}) indicates how well the beam tunnel is isolated, as to avoid leakage of the signal into the beam tunnel thus increasing S_{21} transmission loss. It can be seen how transmission loss is excessive enough that no leakage occurs into the beam tunnel.
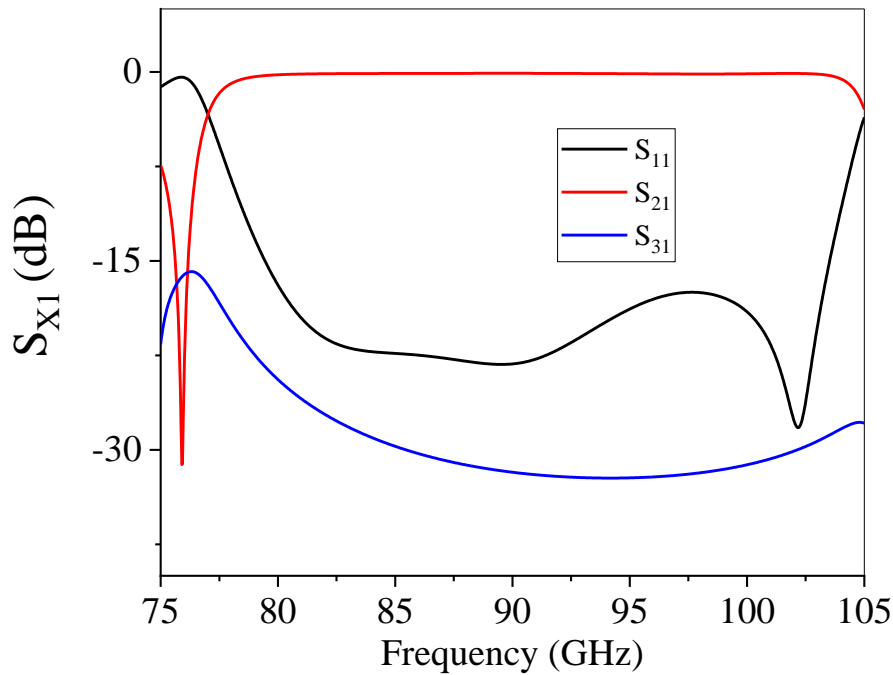
Figure 4-34: Scattering parameters of the coupler bend with the beam tunnel pins placed within the tunnel.

4.4   Particle-In-Cell (PIC) simulations

4.4.1 Introduction

Particle-in-cell (PIC) simulations are performed to simulate the time-domain interaction between the electron beam and the RF signal to determine the resulting amplification in the designed single section TWT. Notable results that can be retrieved and analysed from the PIC simulations are the gain variation with frequency, the output-input power characteristic, and the beam transportation properties. The gain for a TWT is a measure of the amplification of the input signal to the output signal. It is a ratio of the output and input power, typically represented in dB units. To establish amplification, a minimum length for the interaction section of the SWS needs to be used. A parametric study on the number of periods of the SWS was first conducted to study the bunching of the electron

beam and the resulting establishment of amplification. There needs to be a trade-off between the number of periods for optimal gain, and the amount of transmission loss due to the length of the structure while ensuring minimum distortion of the electron beam to avoid collision of particles with the copper structure. Additionally, the tube stability must be considered, using equation (4.7).

The gain is calculated at various frequency points of interest until there is a notable drop in gain, or loss of beam-wave synchronism, which defines the operating band limits of the TWT. For a single-section TWT in the W-band range, a gain of > 20 dB is desirable with a maximum gain variation within the 3 dB margin (3dB-bandwidth).

The beam must avoid collision to the structure, due to beam curling of sheet beams as described in Section 4.2.3 [66]. Beam collision also causes loss of gain due to the loss in electron density, as well as potential damage to the structure. Hence, the structure must be designed to ensure there is enough space for beam passage with minimal amount of beam curling and particle interception with the structure. This also means that the beam size itself and its distance to the SWS must be carefully selected. There must be a balance of having the beam not so close that it collides with the structure, but close enough to maintain sufficient interaction with the field established above the central corrugation.

The value of synchronous beam voltage predicted by the cold simulations must also be optimised for ideal interaction in the desired bandwidth using the PIC simulations. An optimal value is selected by testing different beam voltage values around the initial value predicted by the phase velocity results in the eigenmode simulations.

As shown in Chapter 2, The magnetic focusing system of a TWT is a critical section to ensure the beam is adequately contained. In simulations, a uniform magnetic field is considered for beam confinement to approximate the magnetic focusing system, typically

97

based on a solenoid [10] and PPM [11]. This value is kept in simulation below 1 T, due to complexity involved in accessing higher levels of magnetic field in compact size magnets. The uniform magnetic field for the designed TWT in simulation is set as 0.9 T, the minimum value which adequately confines the beam along the structure.

4.4.2 Beam parametric analysis

Numerical convergence of the PIC simulations results was investigated to adopt the minimum mesh density required for accurate results – due to the size and time intensity of the simulations, this was particularly important to control for. A minimum mesh of 8 million tetrahedron cells was required for convergence to occur.

For an 81-period single section TWT, a parametric study on the effects of current density of the beam on the obtained gain for the central frequency in band is studied in Figure 4-35. The area of the beam is kept constant (0.003 cm^2) while varying the current to change the current density. Increasing the current density increases the gain, due to the presence of more electrons to interact with the electric field. Hence, a current density of 150 A/cm^2 was used in the TWT design to maintain a gain of > 20 dB.
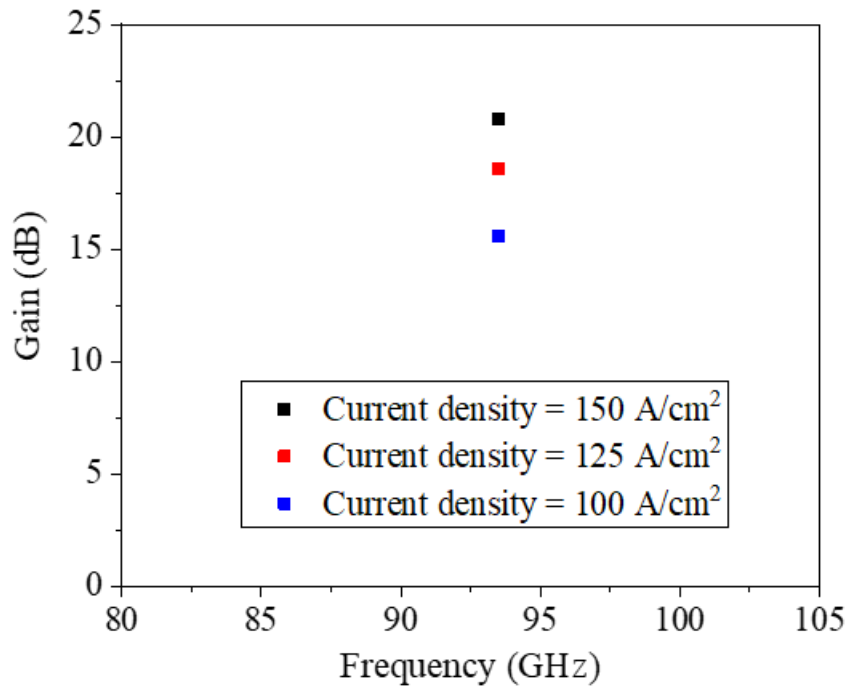
Figure 4-35: Parametric study on the current density of the electron beam for an 81-period HH-GWSWS TWT.
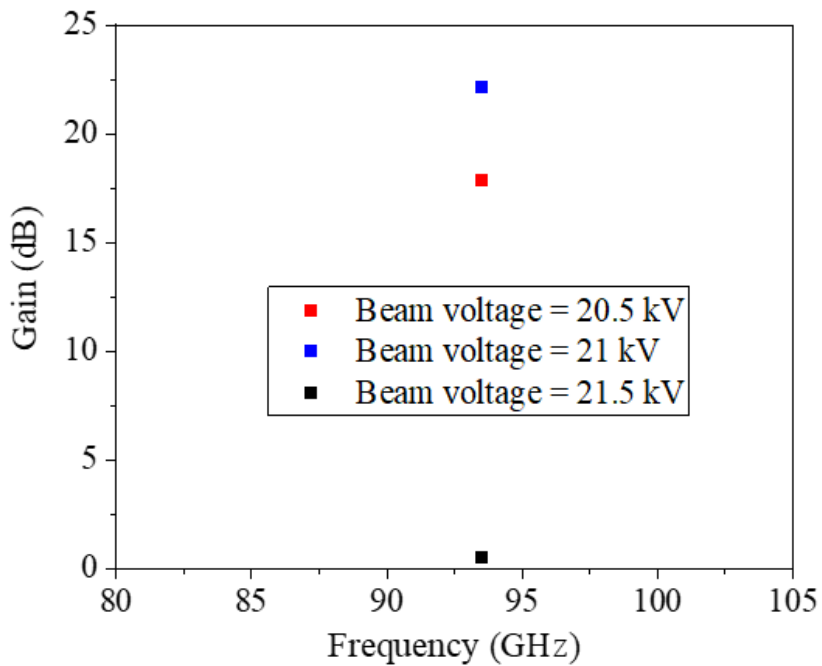
Figure 4-36: Beam voltage parametric study on the 85-period HHGW-SWS TWT.

Several beam voltage values around the predicted synchronous voltage of approximately 20 - 22 kV were simulated in Figure 4-36 to ensure the optimum beam voltage was selected for interaction, using an 85-period length TWT. It was found that 21 kV provided the highest gain, and quickly dropped off beyond 21.5 kV.

(a)   (b)   (c)
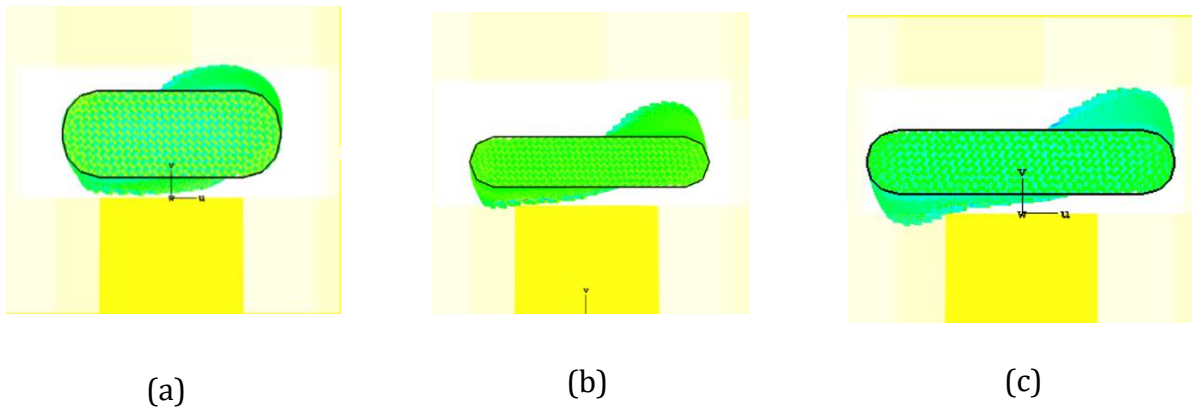
Figure 4-37: (a) a beam with dimensions 0.9 x 0.33 mm, (b) 1 x 0.2 mm, (c) 1.2 x 0.25 mm.
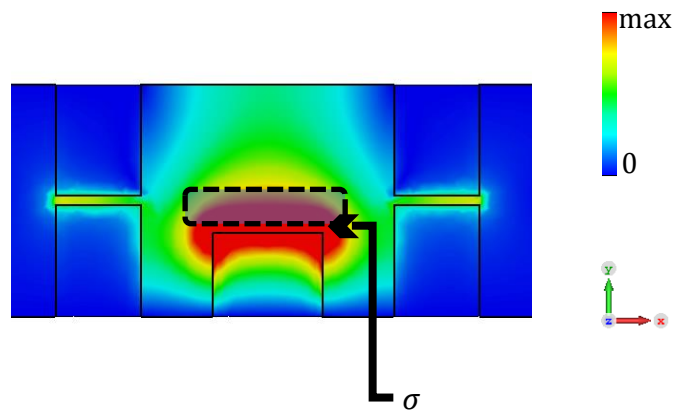
Figure 4-38: Contour plot of the transverse electric field generated by the HHGW-SWS. Superimposed is the dashed outline of the beam. The height of the gap left between the corrugation and beam is denoted as σ.

The beam's aspect ratio is crucial in minimizing collisions between the beam and the structure while sufficiently covering the electric field generated above the corrugation for optimum interaction and gain. Figure 4-37 shows the beam cross section at the end of

the HHGW TWT with 85 periods for different sheet beam aspect ratios. These snapshots were taken at the frequency point 93.5 GHz at the end of the SWS, prior to the beginning of the bend. The preferred beam aspect ratio, shown in Figure 4-37 (c), is selected to reduce the potential for collisions to the minimum while maintaining a gain > 20 dB. Figure 4-38 provides a clearer depiction of the impact of the beam's aspect ratio and position with respect to the localisation of the electric field above the central corrugation. It is necessary to provide a trade-off between the placement of the beam to achieve the optimum gain in the area with the strongest electric field (red indicates the highest field, and blue the lowest) while minimizing any beam curling effects that may result in collisions with the structure. Additionally, it demonstrates that an increase in beam size does not necessarily improve gain. From the previous results, the optimal values for current density and beam voltage are 150 A/cm^2 and 21 kV, respectively.

Finally, a parametric study on the number of the SWS periods is performed, ranging from 85-111 periods, shown in Figure 4-39. A 21 kV beam is used with the optimised beam area of 0.002 cm^2 (0.1 x 0.02 cm) and a current density of 150 A/cm^2. the optimal length for the number of periods of the propagating section can be found by examining the gain achieved from the output port signal at the central frequency of the band (in this case, 93.5 GHz). After careful consideration, 90 propagating periods were determined to be the optimal value for achieving both gain and effective beam transportation. Beyond 95 GHz, excessive beam curling occurs which causes a collision of the beam with the structure.
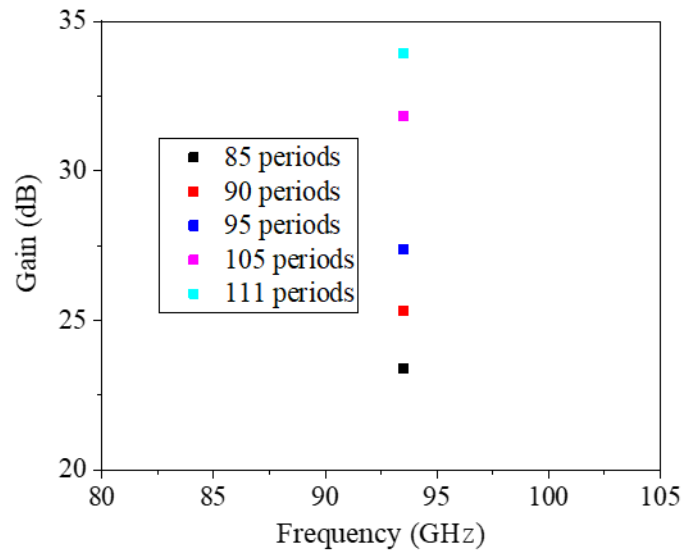
Figure 4-39: Parametric study on the number of
propagating periods for the HHGW-SWS TWT.

Figure 4-40 shows the energy modulation of electrons along the length of the TWT coupler. The electron particles decelerate which indicates electron bunching occurring, and energy is transferred from the electron beam bunches to the RF signal. Figure 4-41 illustrates how this electron energy is distributed along the position of the SWS. The electron energy trending downwards indicates that electron bunching, and energy transfer occurs along the length of the SWS.
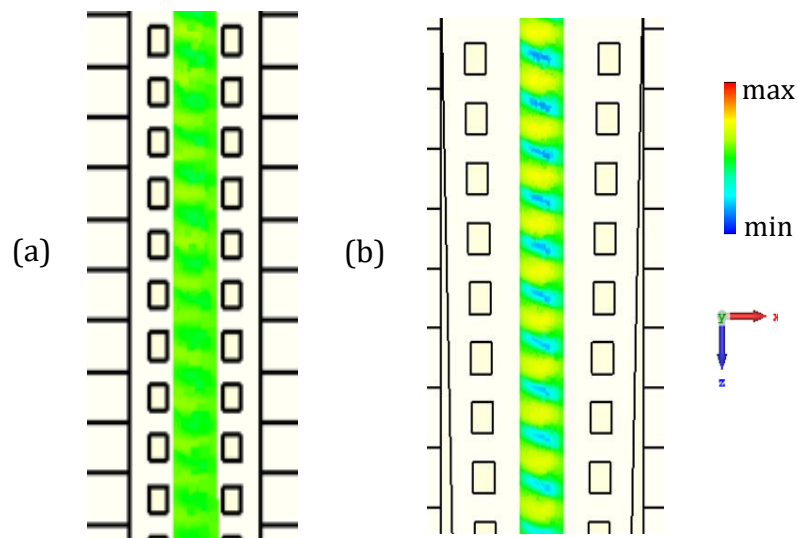
Figure 4-40: Snapshot of the electron beam as bunching of the beam occurs. (a) shows just as bunching is starting to occur, while (b) has established bunching. Various electrons accelerate, while other decelerate.
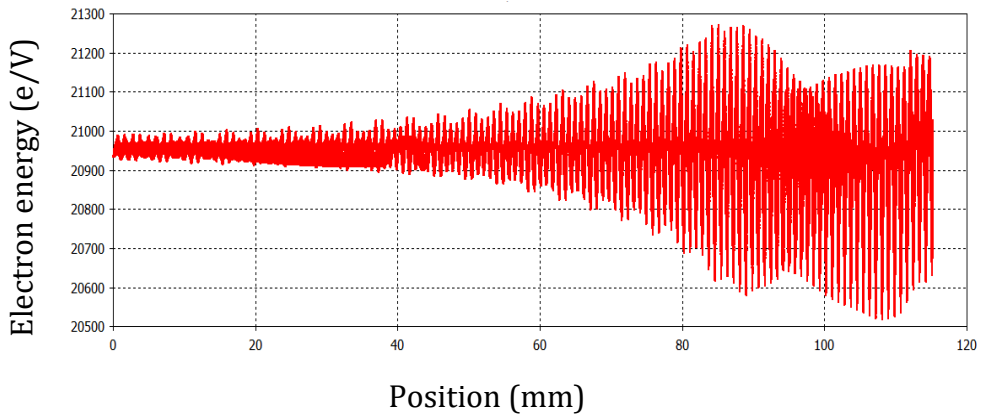
Figure 4-41: Energy modulation of the beam electrons along the length of the TWT indicating bunching of the beam and transfer of energy to the RF signal.

For the final design, a 21 kV beam is used with current of 0.3 A, beam area of 0.002 cm^2 (0.1 x 0.002 cm) and current density of 150 A/cm^2. Figure 4-42 details the gain and output power variation of the HHGW-SWS-based TWT with frequency for the input power of 10 mA. The 3 dB instantaneous bandwidth with a gain of approximately 25 dB is achieved between 89 – 99 GHz.
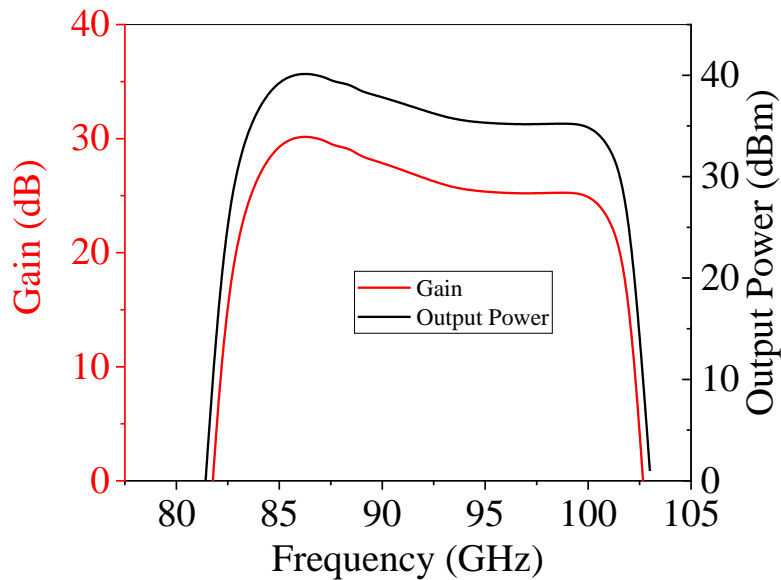
Figure 4-42: Frequency vs Gain, and Frequency vs Output power for the HHGW-SWS.

Figure 4-43 reports the input-output characteristic and corresponding gain for the frequency of 93.5 GHz. It can be noted that about 160 W of saturated power can be achieved with an input power of 0.9 W at 93.5 GHz.
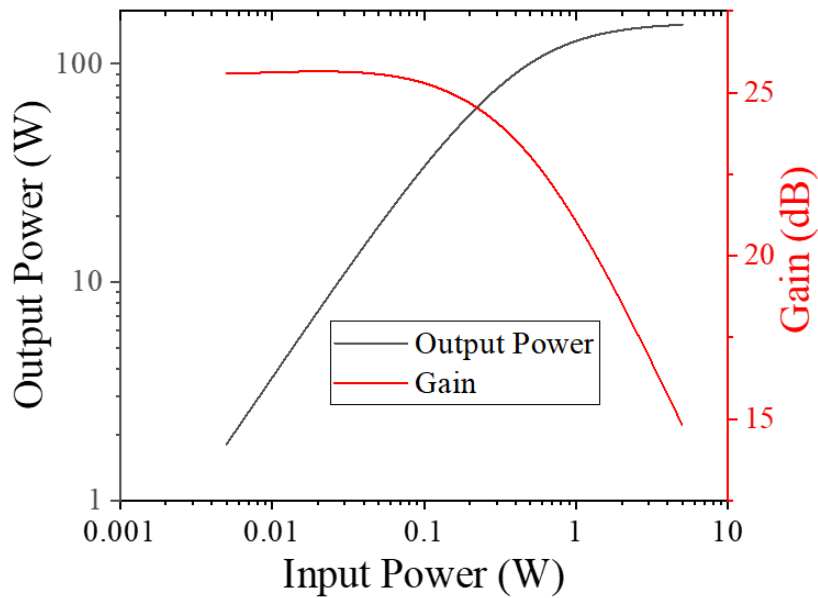
Figure 4-43: Input power vs Output power, and Input power vs Gain for the HHGW-SWS.
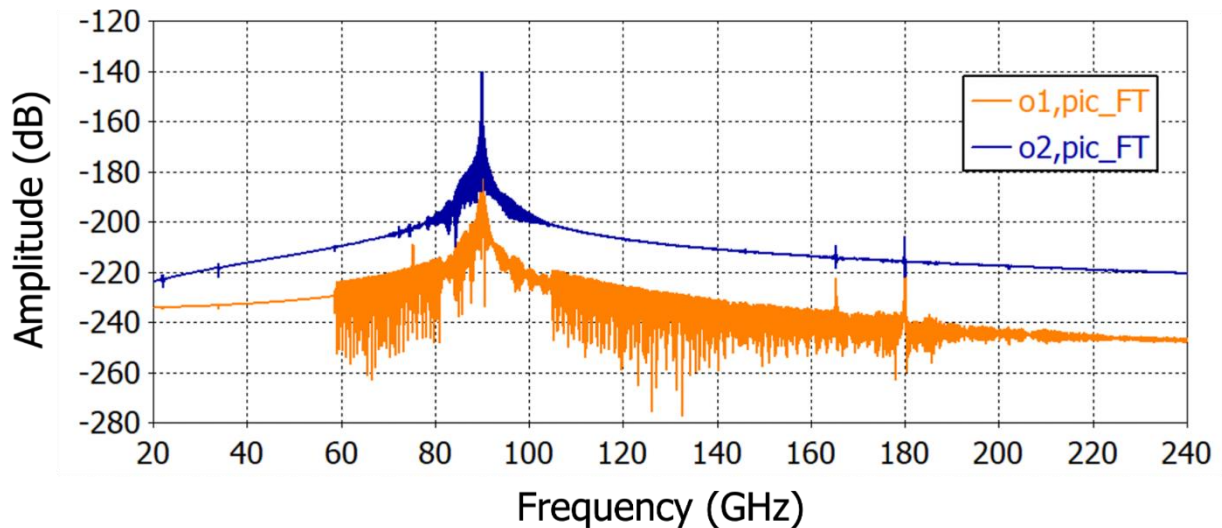
Figure 4-44: Fast Fourier transform of the output and input signal at 90 GHz obtained when running the simulation for 15 ns (in blue and orange, respectively).

Figure 4-44 shows the Fast Fourier Transform (FFT) of the output and input signal obtained at 90 GHz, a critical frequency point as the central frequency for the band, for

the simulated running time of 15 ns. The figure shows high spectral purity and no signs of oscillation of the TWT.

4.4.3   Tube stability

To prevent the occurrence of oscillations, tube stability is examined as high gain in a single-section TWT (exceeding 20-25 dB) may lead to oscillations if losses are insufficient to dampen them. The stability of a single section TWT can be approximated using (4.7) shown in [70]:

$$Q = G - |S_{11}| - |S_{22}| - |S_{21}| < 0 \qquad (4.7)$$

Where Q is the stability factor of the tube in dB, G is gain in dB, S_{11} and S_{22} are the insertion losses at the ports 1 and 2 respectively, and S_{21} is the transmission loss, in dB. Based on the previously simulated s-parameters and the simulated gain, the designed TWT is stable up to a gain of approximately 35 dB.

4.5   SWS prototype realisation

Fabrication of SWSs for vacuum electron devices continues to be a constantly improving field. Within a few years, even more efficient manufacturing techniques will be available to the VED community, which can aid in batch and mass production of devices [71], [62]. For this project, CNC machining is used as an accurate, well-known technique for sub-mm manufacturing of metal waveguides.

One of the advantages for assembly brought by the gap waveguide is that the pins allow to bring the bonding of the metal parts of the SWS two halves further away from the area of interaction, thus reducing the effects of potential SWS assembly defects on the designed electric field for interaction.

105

While a realistic TWT of this structure type would contain 90 periods for the interaction section to allow for gain saturation, for a prototype to measure the cold characteristics, a shorter interaction section can be used to experimentally verify the scattering parameters. The advantages and disadvantages of the FPGW-SWS compared to the HHGW-SWS were considered as to which would be preferable for fabrication of a prototype. Ultimately the HHGW-SWS was chosen due to the following advantages:

- More compact structure in comparison to the designed full pin coupler. In the case of a TWT, a more compact structure is more desirable to ease the magnetic focusing system design, while also reducing the complexity and footprint of fabrication.

- The short pillars have a smaller aspect-ratio, thus allowing for much easier fabrication, as there is less risk of bending or snapping of the pins during machining.

- An all-metal structure simplifies the fabrication and assembly process.

Prior to fabrication, the most critical dimensions are examined to indicate how sensitive they are to machining tolerances and verify robustness of the HHGW design to a misalignment of the top and bottom half in assembly as it will be shown in the following Section.

4.5.1   Misalignment and gap sensitivity study

One of the challenges found commonly in TWT assembly is the alignment of the top and bottom split blocks of the SWS. Misalignment can affect the dispersion of the SWS, leading to the worsening of synchronism with the beam. An example of sensitive misalignment of structures affecting the interaction field is the folded waveguide. It is found that even a

misalignment of 10 μm of the two halves of the waveguide causes a large shift and disruption of the dispersion of the SWS mode [62].
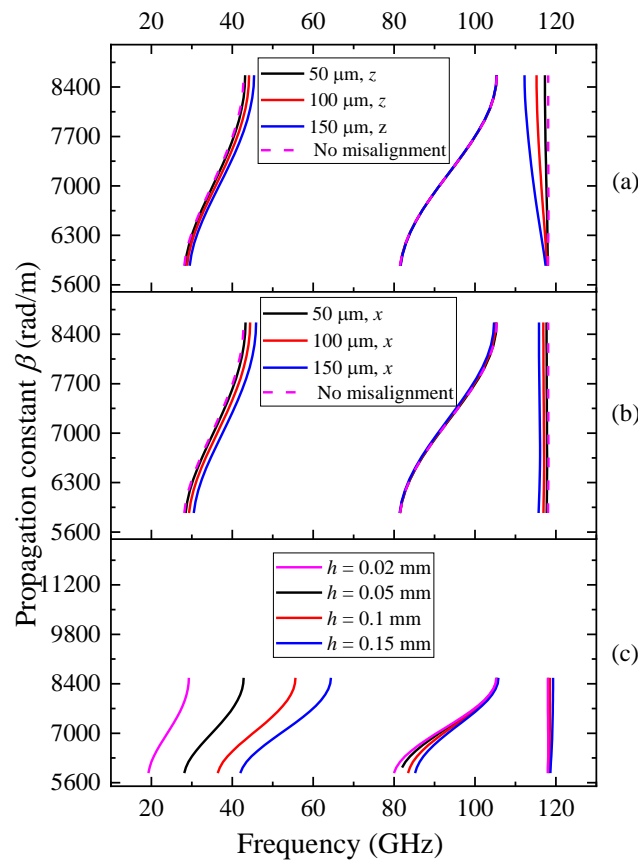
Figure 4-45: Dispersion characteristics for HHGW-SWS with a misalignment of 50 μm, 100 μm and 150 μm, in (a) *z* and (b) *x* direction, compared to no misalignment (dashed line); (c) Sensitivity study on the dispersion characteristic when varying *h*.

The gap waveguide is shown to be robust enough to withstand a misalignment of even 150 μm in the *x* or *z* direction. Figure 4-45 (a) and (b) report simulation results of the effects of misalignment of the top and bottom pins on the dispersion characteristics of the SWS mode and stopband width. Changing the alignment in both the *x* and *z* direction has no impact on the mode dispersion of the SWS. There is a shift on the stopband, however, not enough to cause direct impact to the operating frequency band.

A sensitivity study was conducted to better understand the tolerances required by the gap dimension, *h*, in fabrication. In Figure 4-45 (c), a gap in the range of 0.05 mm – 0.15 mm is studied. This figure shows that a larger gap size reduces the size of the stopband,

107

which impacts the interaction mode by shifting the value of its cut-off frequency. This could cause potential issues of desynchronising the propagating mode phase velocity with that of the beam velocity over the designed operation band, which in turn could reduce the bandwidth of the TWT. It can be noted that the gap height has minimal impact on the high frequencies, mostly impacting the lower frequencies of the interaction mode. This is also evident when looking at the scattering parameters in Figure 4-46. However, it needs to be noted that the gap dimension in this study is varied above the typical tolerances found in precision machining (+/- 10-20 μm), thus effects on interaction mode and TWT operation bandwidth will be marginal.
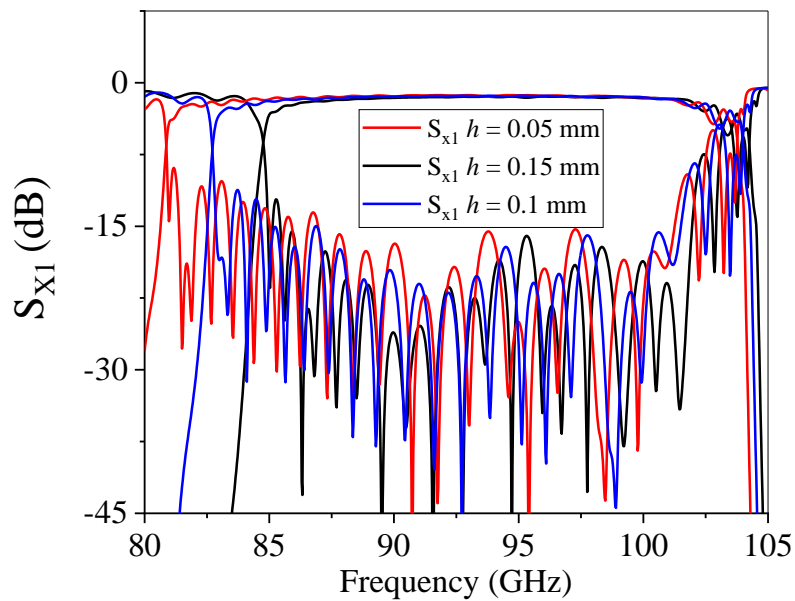
Figure 4-46: Sensitivity study of the HHGW-SWS, on the gap h in terms of the scattering parameters.

4.5.2   Prototype characterisation

The prototype of the HHGW-SWS was first configured on Solidworks to be compatible with the CNC programming for milling. A 10-period HHGW-SWS CAD design is shown in Figure 4-47 and Figure 4-48, which is used to program the CNC machine to mill the pins into a 25 cm (per half) thick block of aluminium. Aluminium is chosen instead of copper to facilitate the machining process.

(a)   (b)
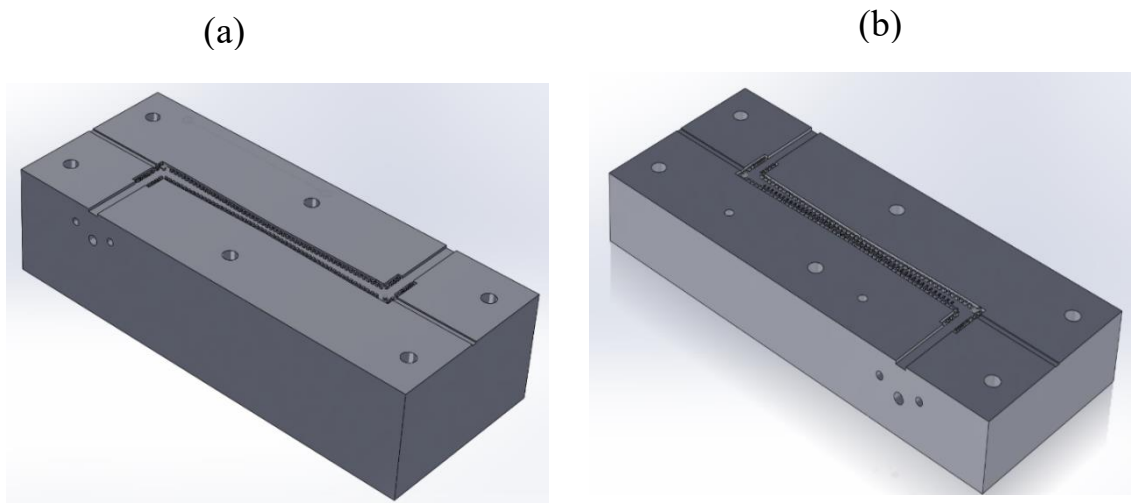
Figure 4-47: CAD design of (a) Top half of the 10-period HHGW-SWS coupler. (b) Bottom half.

(a)   (b)
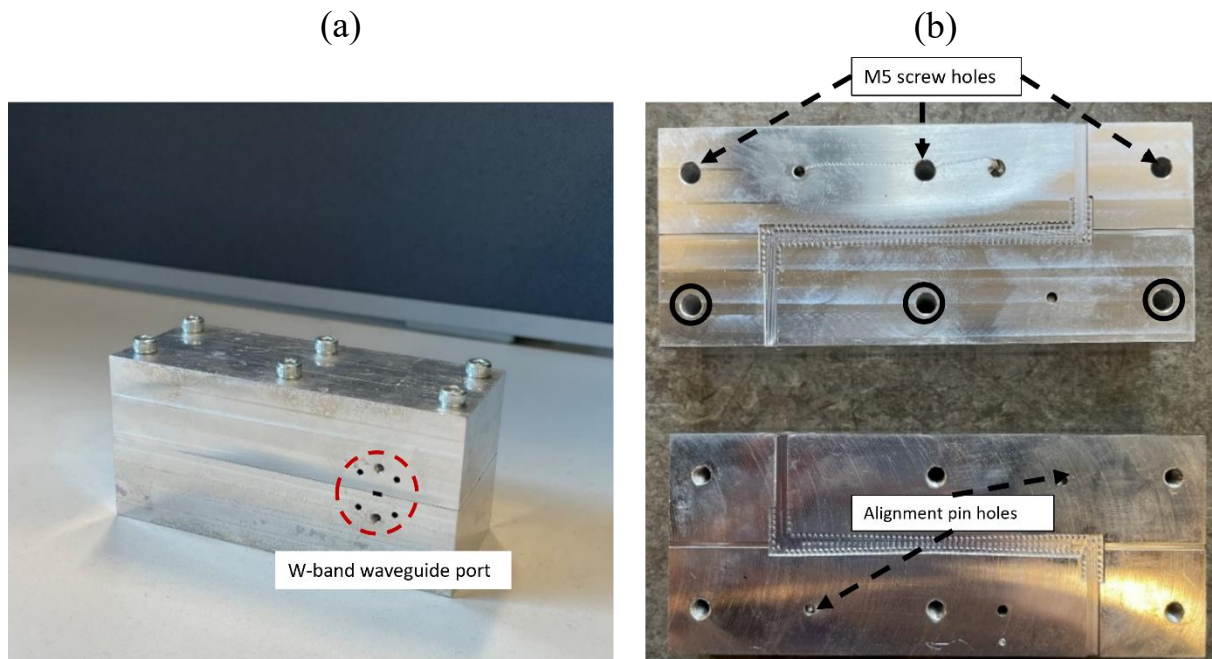
Figure 4-48: (a) Perspective view of the fabricated and assembled prototype of the HHGW-SWS TWT. (b) Top half of the structure (top), bottom half of the structure (bottom).

A 0.4 mm tooling piece was used for an air turbine rotating at 50,000 RPM on the CNC machine MAZAK VCN-430A. The part was machined in-house by the technicians in the School of Engineering, Lancaster University. Each half took approximately two days to machine, totalling 4 days to complete fabrication. The pieces were then returned to me for cleaning (ultrasonic bath in acetone and isopropyl alcohol), inspection under the microscope, assembly and measurement of the cold characteristics. The dimensions and surface roughness were examined under the Olympus 3D LEXT microscope. The microscope can virtually build a 3D model of the structure to measure the real dimensions of the pins and corrugations. Figure 4-49 shows a microscopic view of the coupler bend. It was found that dimensions of the cross section (width, length, period) were accurate approximately in the range of +/- 10-20 μm, shown in Figure 4-50. Height had more variation of +/-30-40 μm, although this contains a certain margin of error due to this not being a direct microscope measurement. There appears to be a certain level of tapering to the pins and corrugations due to the nature of the machining, where a variation of 10-30 μm [+/-] of the pin width could be seen from the top of the pin to the bottom of the pin.
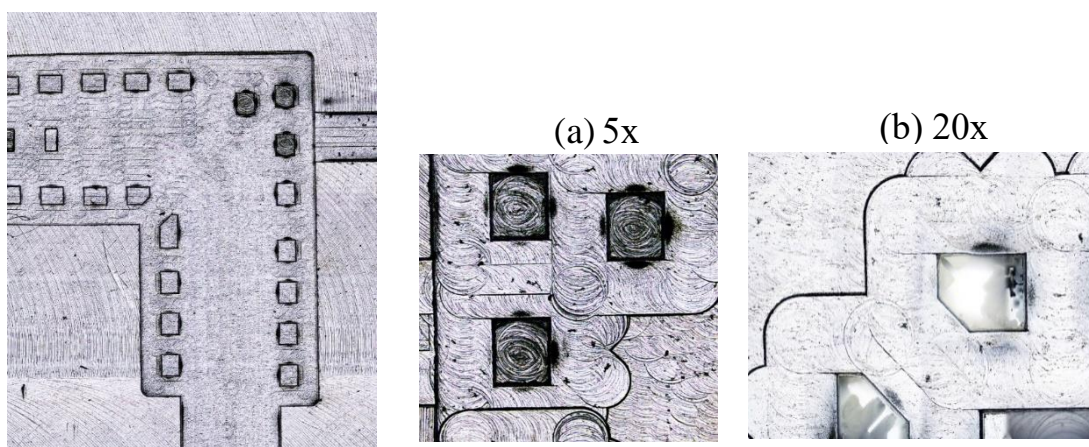
Figure 4-49: Microscopic image of the coupler bend (a) Beam tunnel pins at 5x (b) Inner corner pins at 20x.
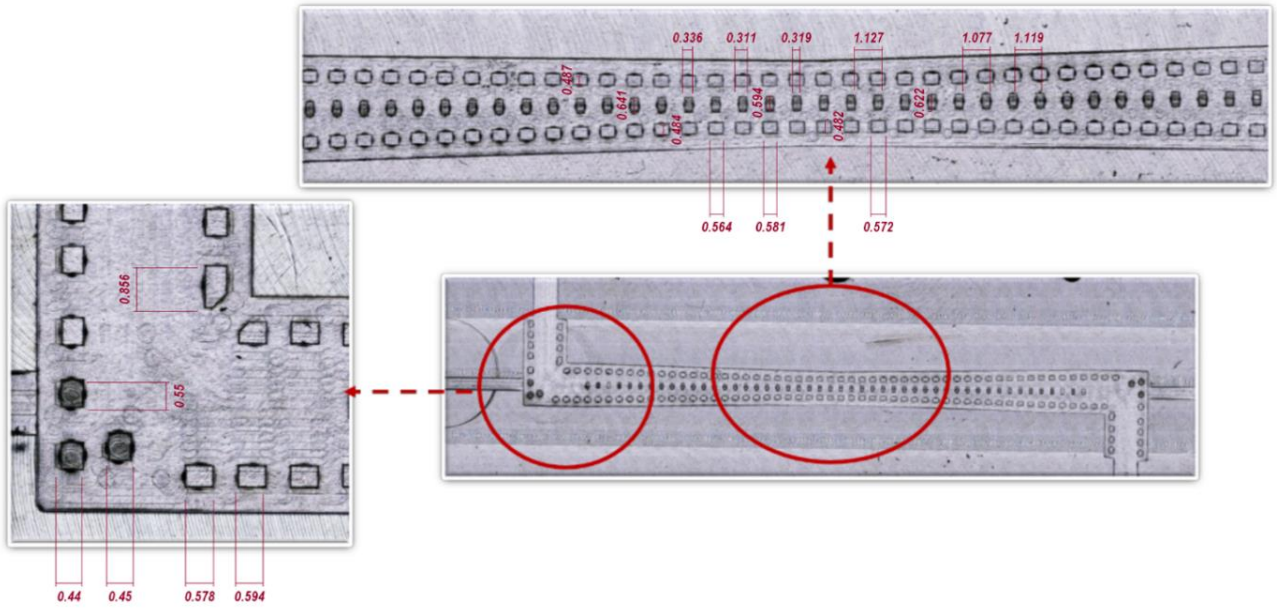
Figure 4-50: Microscopic view of the bottom half of the fabricated GW-SWS, zooming into the bend and propagation section. Dimension values are in mm.

4.5.3   Surface roughness measurement and analysis - Hammerstad-Bekkadal Model

In simulation, the metal is modelled with a reduced conductivity to mimic the typical effects of ohmic losses due to surface roughness. This is done for both the copper for the SWS design and for simulations employing aluminium, to compare with the measured results from the prototype. An accurate estimate of these losses can be modelled by measuring the average surface roughness of the prototype structure, and using the empirical formula in [72], [73] to calculate the corresponding reduced conductivity. Employing the Hammerstad-Bekkadal (HB) Model [72] the equation shows that:

$$f_{roughness} = \left\{ 1 + \frac{2}{\pi} \tan^{-1}\left(1.4 \left(\frac{\Delta}{\delta}\right)^2 \right) \right\} \qquad (\ 4.8)$$

Where (Δ) is the surface roughness in metres, and (δ) is the skin depth of the metal in metres. The skin depth of the metal for a specified frequency can be calculated as:

111

$$\delta = \sqrt{\frac{1}{\pi\mu\sigma f}} \tag{4.9}$$

The magnetic permeability μ can be taken to be $\mu \approx \mu_0 = 4\pi \times 10^{-7}$ H/m. The electrical conductivity of the metal is σ, and frequency is f in Hz.

From this, the estimated effective conductivity can be calculated as:

$$\sigma(\Delta) = \frac{\sigma(\Delta = 0)}{\left(f_{roughness}\right)^2} \tag{4.10}$$

Where $\sigma(\Delta = 0)$ is the conductivity of the smooth un-patterned metal, or otherwise known as the ideal conductivity of the material.

Using (4.8), (4.9) and (4.10) for the metal aluminium, the values calculated using the measured surface roughness of $\Delta = 200$ nm and a value of ideal conductivity $\sigma = 3.56 \times 10^7$ S/m and $f = 93$ GHz.

$$\delta = 2.77 \times 10^{-7} \text{ m}$$

$$\sigma(\Delta) = 1.78 \times 10^7 S/m$$

Hence, the effective conductivity of the patterned aluminium is approximately half of the ideal conductivity of the metal.

4.5.4 Cold test of the HHGW-SWS prototype

The SWS prototype is measured using a vector network analyser (VNA R&S ZVA 40). The input and output ports are connected to the VNA using 75 – 110 GHz extenders. Alignment of the waveguide flange and ports is done by using alignment pins to ensure proper alignment and to be flush on the port, so no leakage of the signal occurs which would impair accuracy of results. Before measurement, the coupler was assembled. Two 2mm diameter alignment pins were placed in their machined holes between the two halves to ensure the pieces did not shift once screwed together, and six M5 screws were used to hold the two halves together. The two parts were also clamped to avoid any air gaps, which marginally improved transmission losses. The assembled part was then connected to the network analyser via two W-band flanges to the input and output ports.
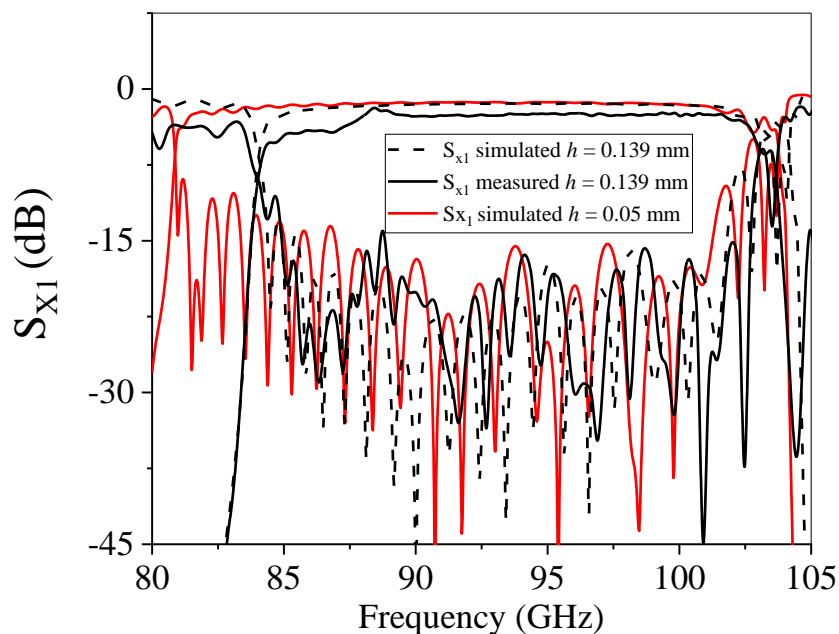
Figure 4-51: The measured scattering parameters of the CNC machined HHGW-10-period SWS coupler. It is compared to the intended simulated gap value of h = 0.05 mm, and the suspected simulated machined gap value of h = 0.139 mm.

The transmission losses (S_{21}) of the simulated structure are compared to Figure 4-51 using a reduced conductivity value of σ = 1.78 × 10^7 S/m which is the surface roughness equivalent of approximately 200 nm [72].

113

Figure 4-51 shows the measured scattering parameters of the first CNC machined HHGW 10-period SWS prototype, compared to the simulated design gap value of h = 0.05 mm, and the suspected machined gap value of h = 0.139 mm.

It can be seen in Figure 4-51 the measurement of the SWS prototype showed that there was a significant shift in the cut-off frequency of the SWS mode. After analysing the parts under the microscope, the air gap between the pins was seen to be h = 0.139 mm, a difference of approximately 89 μm compared to the designed value of h = 0.05 mm, which is higher than reasonable tolerance of machining expected at this frequency. By examining the microscope images, it could be seen that the error was due to one half of the parts had a wall height 89 μm higher than designed. Therefore, around 50 μm was milled off the wall of one part, as a conservative estimate, to avoid damaging the pins. This is interesting to note, as the air gap is shown to be one of the more critical dimensions for the mode frequency cut-off as shown previously in Figure 4-45 (c). Comparing the measured values of the re-iteration of the milled structure after removing 50 μm, this would leave an assumption of giving a value of h = 0.09 mm. Comparing to a simulated value of h = 0.1 mm in Figure 4-52 (with an S_{11} of -15 to -18 dB), it can be seen the measured value fits much closer to this, thus a removal of around 40 μm was achieved.
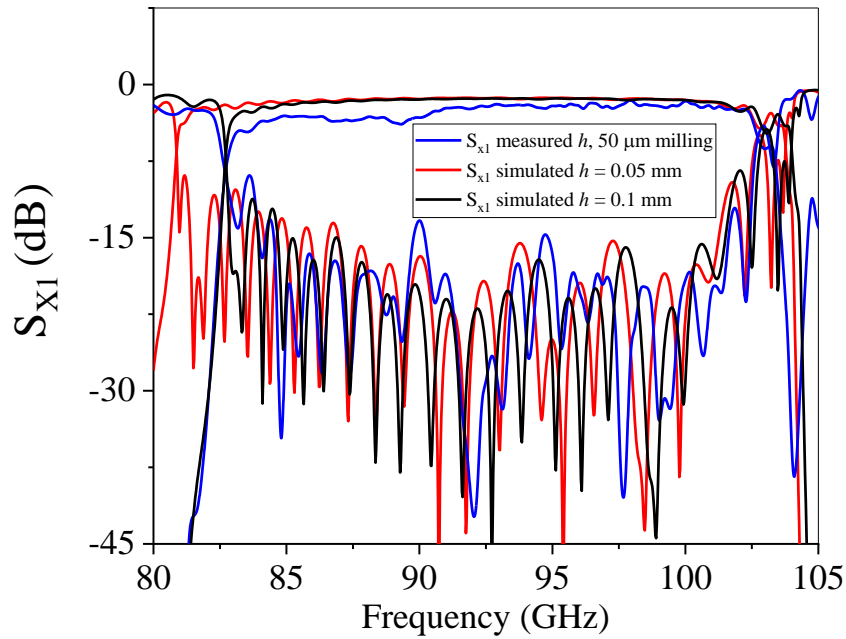
Figure 4-52: Scattering parameters of the measured second iteration of the HHGW-SWS 10-period coupler, compared to the simulated s-parameters of the intended gap of h = 0.05 mm, and the simulated suspected gap of h = 0.1 mm.

The original provided frequency band was 81 – 104 GHz, with the second iteration providing a frequency band of 83 – 104 GHz. The final simulated operating bandwidth of the HHGW-SWS TWT is 89 – 99 GHz when taking into account the beam synchronism. With the achieved gap height of h = 0.1 mm, there is a slight loss in synchronism at the start of the frequency band which may cause a reduction in the bandwidth, shown in Figure 4-53. The final operating bandwidth of the machined HHGW-SWS TWT should not be impacted as the region of synchronism is 89 – 99 GHz.
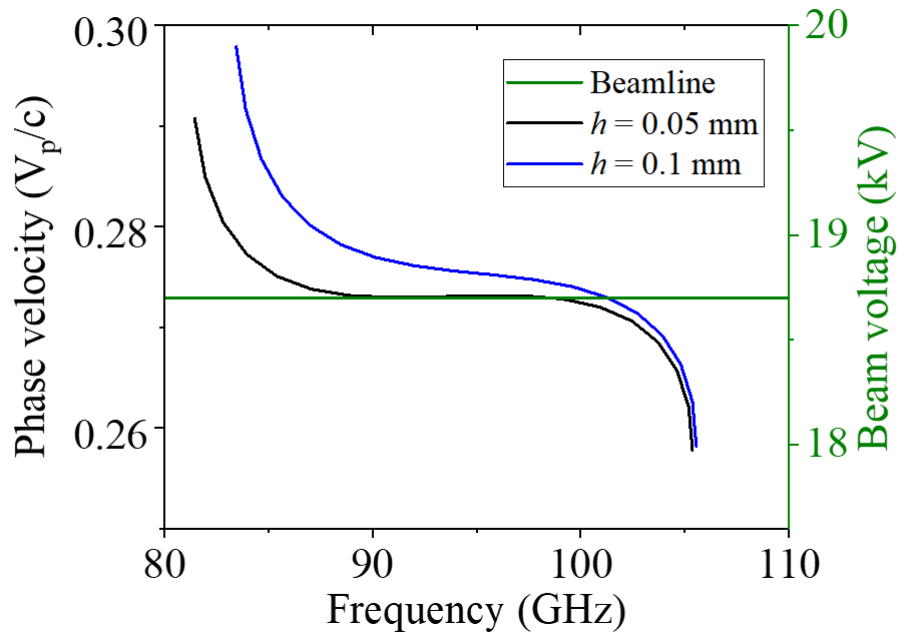
Figure 4-53: Phase velocity comparison of the HHGW-SWS, of the designed gap height h = 0.05 mm, versus the achieved gap height of h = 0.1 mm. The 19 kV beamline is superimposed over the graph to show the region of synchronism.

4.6 Conclusion

This chapter gives a comprehensive study, design, and demonstration of two novel pin-based gap waveguide when implemented in a slow wave structure (SWS) for travelling wave tubes (TWTs) operating in the W-band. The first SWS studied was based on the full-pin gap waveguide, which uses one row of full-length pins on either side of a rectangular corrugated waveguide. The dispersion characteristics, beam synchronism and scattering parameters are studied, leading to the final design of the full-pin gap waveguide-based SWS (FPGW-SWS). The FPGW-SWS shows a synchronous region of 90 - 100 GHz, providing low reflections and minimal transmission losses. The second SWS studied is based on the half-height pin gap waveguide. This type of gap waveguide was recently proposed in the literature to provide relatively wide stopbands. Dispersion and interaction impedance parametric studies were conducted on this SWS structure,

116

resulting in the half-height pin gap waveguide-based SWS (HHGW-SWS). The HHGW-SWS was compared with the FPGW-SWS, along with the half wall/half pin gap waveguide-based SWS (HWHP-SWS). Several advantages were found in the HHGW-SWS in comparison to the other proposed structures, notably the lower aspect-ratio pins and compact and flexible coupler design that can easily accommodate very high aspect ratio sheet beams. Hence, additional Particle-in-Cell simulations were conducted on the HHGW-SWS. A misalignment and sensitivity study were conducted on the most critical dimensions of the SWS, namely the gap height h. Finally, the fabrication via CNC machining, assembly and measurement of the scattering parameters and dimensional tolerances of the prototype is considered. The measured results are compared to the simulated results of similar dimensions measured under the microscope. These results show that the pin-based gap waveguide can be successfully implemented in a single section TWT at a high frequency range (specifically W-band frequencies) and provide the benefits of a stopband-based field confinement control for the SWS within a relatively easy geometry to realise. A final wide operating bandwidth of 89 – 99 GHz is presented for the HHGW-SWS, with a minimum 3 dB bandwidth gain of 25 dB and saturated output power of 160 W.

CHAPTER 5: THE GLIDE SYMMETRY GAP WAVEGUIDE SWS

5.1   Introduction

Chapter 4 studied in detail two types of gap waveguide structures for the design of mm-wave SWSs– the full-pin gap waveguide, and the half-height pin gap waveguide. The half wall/half pin gap waveguide alternative was also reviewed in comparison to these structures. They were both implemented for the use in a SWS for travelling wave tubes (TWTs) using rectangular corrugated SWSs. So far, the structures studied have used the pin gap waveguide model, following the theory used in Chapter 3. This chapter will focus on an alternative to the pins – using two plates of drilled holes, shifted half a unit cell longitudinally with a gap in the centre of the structure. This is referred to as the holey glide symmetric gap waveguide (Holey GW). It follows the same premise as the pin-based gap waveguide, but the period is typically much larger comparative to the period of the pins. This can provide the advantage of further simplifying the machining, with the potential ability to allow faster production and repeatability. The larger dimensions relative to the frequency mean that theoretically, structures with a much higher frequency can be designed without the issues found with sub-mm fabrication. The simplicity of the design also allows batch production to become more feasible. One example of the holey glide symmetric groove gap waveguide has been realised in [74]. The structure also was presented in the literature as capable to achieve a large bandwidth. However, the mismatch of the gap waveguide period and the central corrugation period adds a level of complexity to carefully selecting the periods of both structures as well as correctly analysing the eigenmode simulation data for the SWS unit cell. Multi-period structures are rarely proposed because of this, one example is the

119

photonic crystal waveguide shown in [50]. The design guidelines of this gap waveguide are also slightly different. The work in [75] and [57] detail the design characteristics and guidelines for the holey glide symmetric gap waveguide. This chapter aims to investigate for the first time the holey glide symmetric gap waveguide for the design of a SWS in a TWT and compare results to the previously proposed pin-based GW-SWSs, to assess its advantages and limitations.

5.2 The holey glide symmetric gap waveguide design guidelines
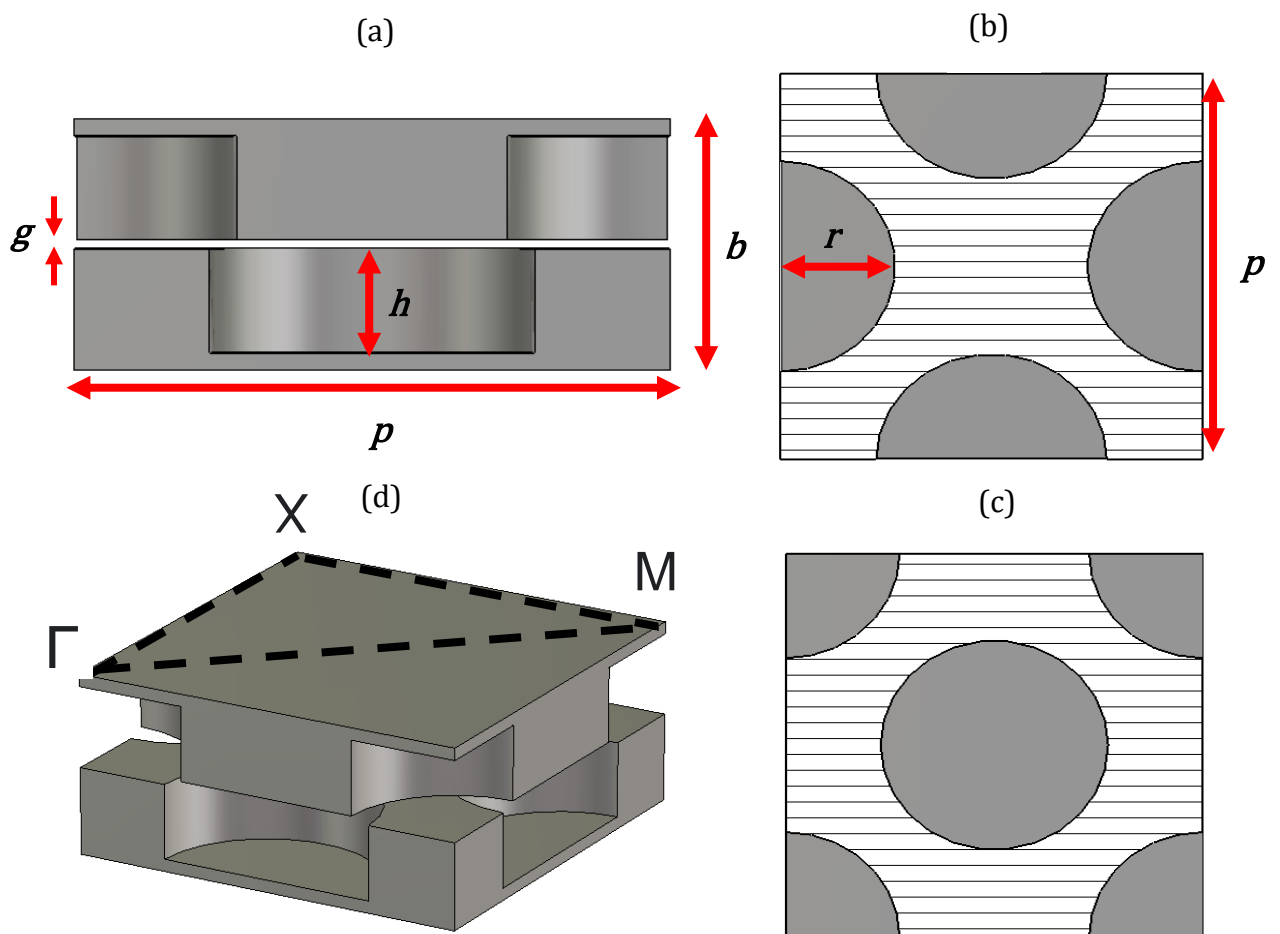
Figure 5-1: Schematic of the holey glide symmetric gap waveguide unit cell (a) Front view (b) Bottom plate (c) Top plate (d) Perspective view which shows the irreducible Brillouin zone.

Table 5-1: Dimensions of the Holey GW unit cell.

Dimensions	Value (mm)
p	3.3
h	0.61
g	0.05
r	0.9
b	1.27

Figure 5-1 and Table 5-1 present the schematic and dimensions for the holey glide symmetric gap waveguide (Holey GW) unit cell respectively. The irreducible Brillouin zone indicates the smallest possible range of the k-space, where k is the wave vector, which represent the non-symmetrical solutions of an infinite periodic lattice [76]. The band diagram of a periodic unit cell is conventionally represented by solving the geometry for the k values along the edges of this zone.

Parametric studies are run on the dimensions to better understand the design characteristics of the structure. Previous work in [57] suggests that there is an optimal radius to period ratio to maximise the bandwidth of the stopband – in the 20 – 50 GHz frequency range, it was found that the optimal ratio of r/p = 0.275 [57], or when the radius of the hole is a quarter of the period.

Using this ratio, an initial guideline for the dimensions can be selected. Given the period of the corrugation used will be $p_{corrugation}$ = 1.1 mm, the period of the Holey GW to achieve a stopband in the W-band range was chosen as p = 3.3 mm. With the period selected, an initial value of the radius can be approximated to r = 0.9 mm. Since the height of the W-band waveguide is 1.27 mm, b is set to this value. The values h = 0.61 mm and g = 0.05

mm are kept the same as the HHGW-SWS for initial simulations, as they equate to b. These initial values are used to conduct the parametric studies.

For h, literature states that a minimum hole depth is required, but after that increasing it further has not impact on the stopband. This allows for a certain level of flexibility to equate the hole depth to the waveguide height, thus not requiring any height tapering in the coupler. Figure 5-2 shows the band diagram of the glide symmetry unit cell with dimensions as given in Table 5-1. For clarity, only the band edges that define the stopband for each geometry are included. The effect of varying h is shown. Reducing h creates minimal variation in the stopband beyond $h = 0.61$ mm.
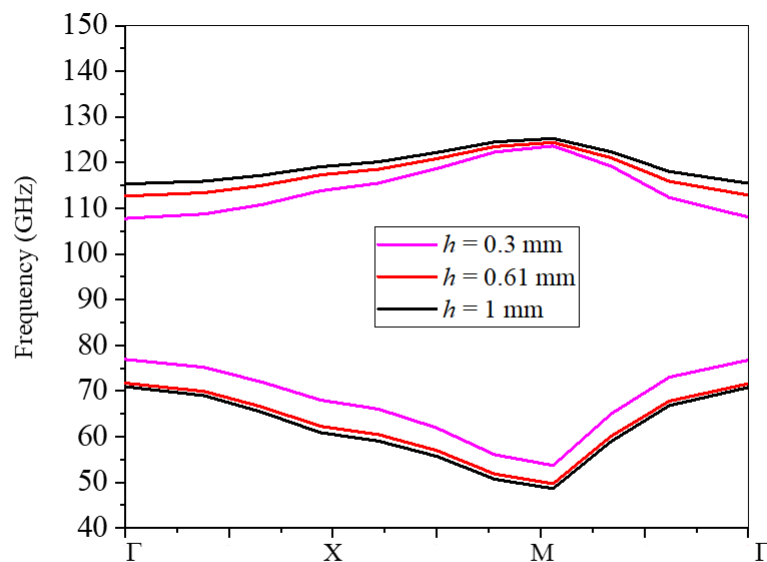
Figure 5-2: Parametric study on the Holey GW unit cell, varying h. Other dimensions are $p = 3.3$ mm, $r = 0.9$ mm, $g = 0.05$ mm, $b = 1.27$ mm.

Similar to the pins structure, decreasing the gap size increases the stopband. When the gap is not small enough, the stopband does not exist. This is demonstrated in Figure 5-3.
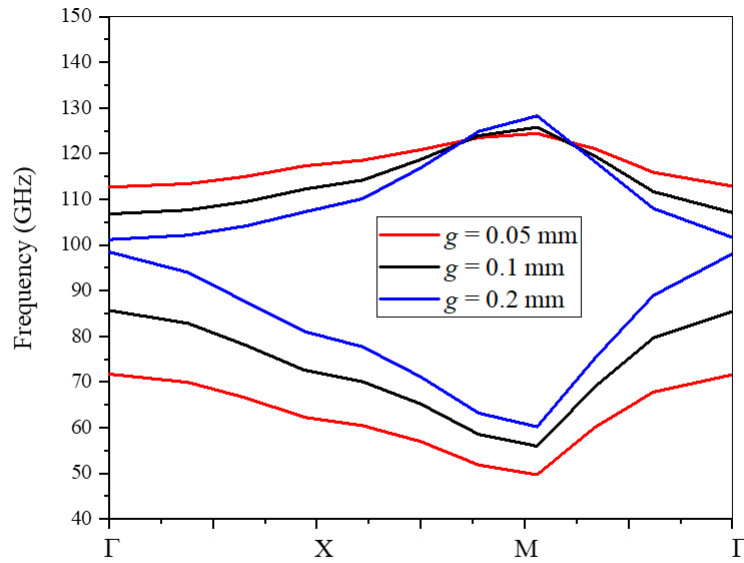
Figure 5-3: Parametric study on the Holey GW unit cell, varying g. Other dimensions are $p = 3.3$ mm, $r = 0.9$ mm, $h = 0.61$ mm, $b = 1.27$ mm.
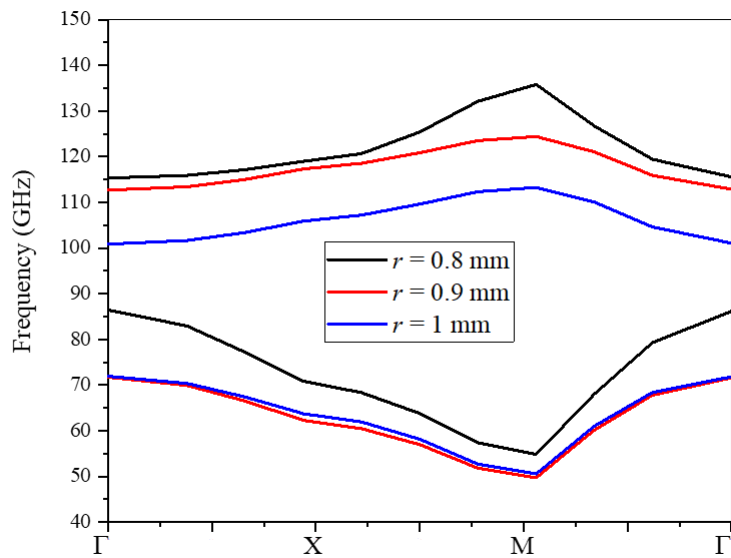
Figure 5-4: Parametric study on the Holey GW unit cell, varying r. Other dimensions are $p = 3.3$ mm, $h = 0.61$ mm, $g = 0.05$ mm, $b = 1.27$ mm.

Figure 5-4 keeps the period constant to $p = 3.3$ mm, while the radius r is varied. The optimal radius for this structure would then be $r = 0.9$ mm. Conversely, when keeping $r = 0.9$ mm constant and varying p in Figure 5-5, the optimal radius to period ratio in the W-band frequency range can be deduced to be $r/p = 0.272$. Generally, it was found that while

the stopband was adequate for this design, the bandwidth was not necessarily found to

be significantly wider compared to pin-based gap waveguides.
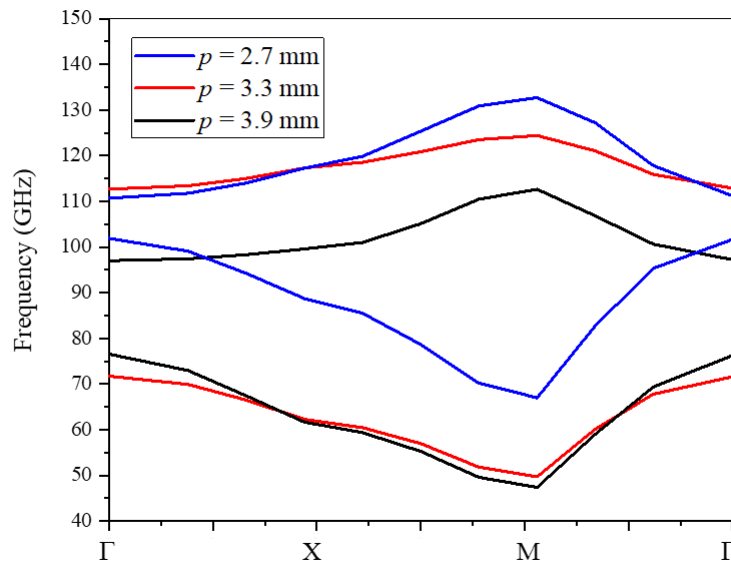
Figure 5-5: Parametric study on the Holey GW unit cell, varying p.
Other dimensions are h = 0.61 mm, r = 0.9 mm, g = 0.05 mm, b = 1.27 mm.

5.3   The holey glide symmetric gap waveguide-based SWS (Holey GW-SWS)

Based on the unit cell parametric studies, the optimised dimensions for the holey glide

symmetric gap waveguide are selected for the W-band (75 – 110 GHz) corrugated

waveguide. The unit cell, Figure 5-6, is studied in the irreducible Brillouin Zone in Figure

5-7. The mode that propagates in the z-direction are described in the first Γ-X range. The

unit cell shows a stopband from 71 GHz – 112 GHz for the x-z plane.
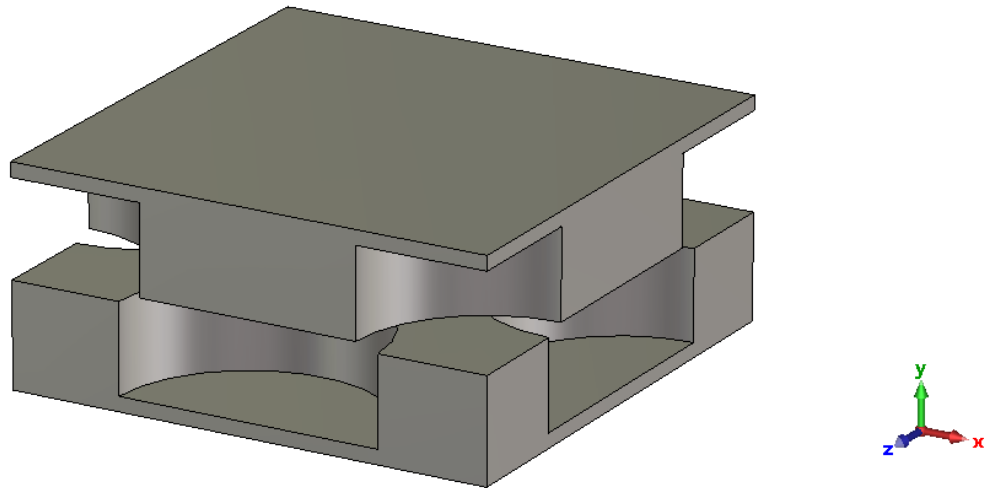
Figure 5-6: Perspective view of the Holey GW perfect unit cell.
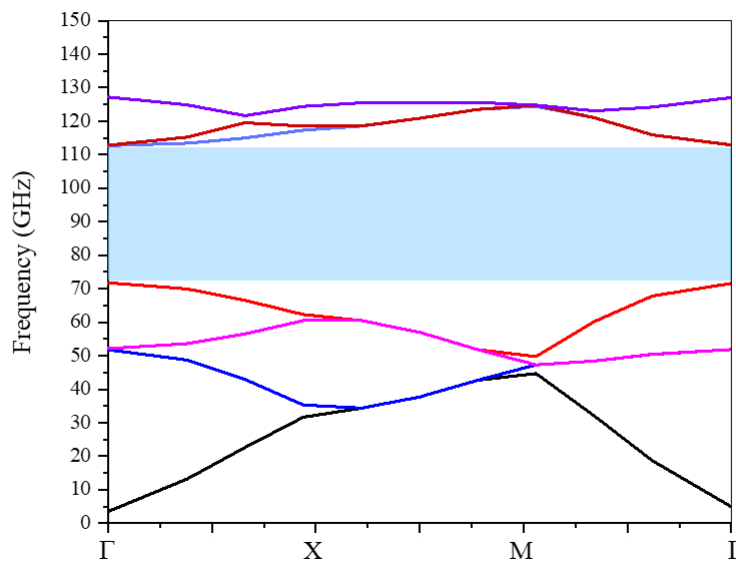
Figure 5-7: The unit cell stopband for the Holey GW-SWS.

The unit cell studies the periodicity in 2 directions. For implementing the Holey GW SWS, when a central longitudinal defect is introduced to form the waveguide, we need to restrict the study to the only direction where periodicity is conserved, in this case, along *z.* Before the waveguide is realised, the macro cell for the Holey GW, which will

correspond to the number of periods used to confine the waveguide modes laterally as shown in Figure 5-8, is studied.

(a)

(b)   (c)

(d)
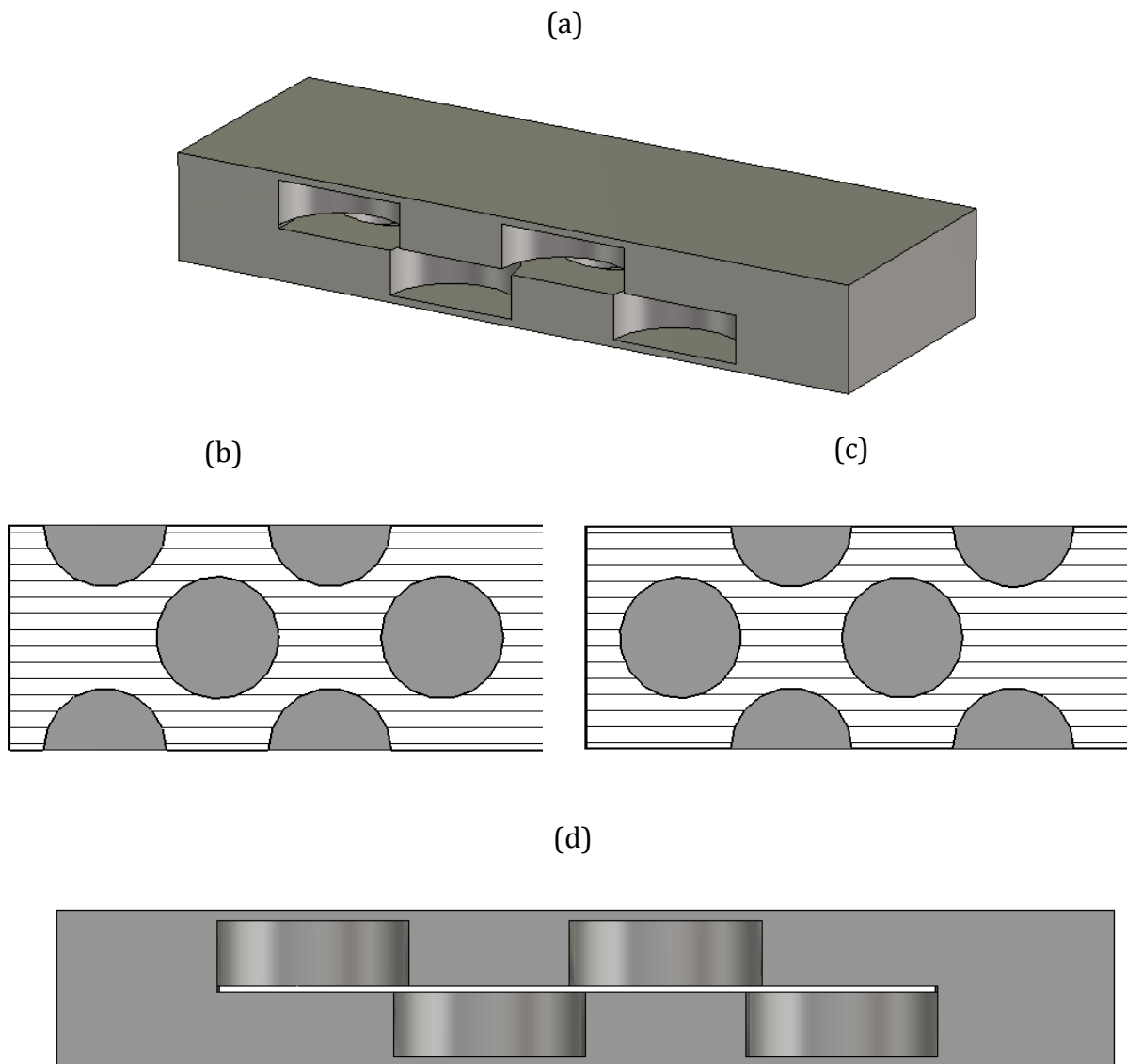
Figure 5-8: Schematic of the macro cell for the Holey GW (a) Perspective view, (b) Top plate, (c) Bottom plate, (d) Front view.

The use of 2 periods (4 rows) of the Holey GW is used initially. The propagation along z is shown in the first Brillouin zone (0-1) and shown in comparison to the unit cell band diagram in Figure 5-9. The macro cell, which approximates the unit cell characteristics, provides a stopband of 69 – 114 GHz.
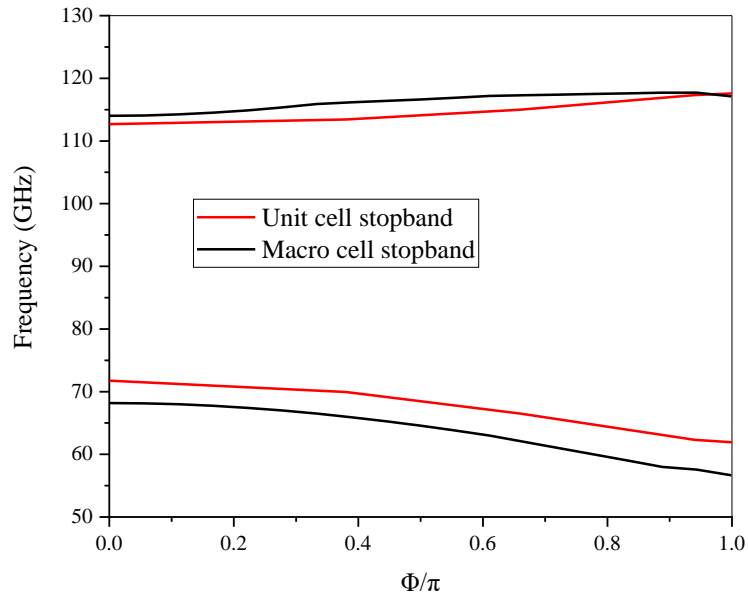
Figure 5-9: Comparison of the perfect unit cell to the macro cell of
the stopband of the Holey GW.

It is interesting to note how, comparative to the pin-based gap waveguide, the Holey GW

stopband is influenced much more by the entirety of the structure and introduction of a

groove channel. While this stopband is still adequate for the designed SWS, this reduction

in stopband must be considered when implementing the Holey GW in the form of a SWS.

The Holey W-band GW is shown in Figure 5-10, with two periods (4 rows) on either side

of the channel. This waveguide implements a W-band groove channel (2.54 mm x 1.27

mm) with two periods (4 rows) on either side of the groove channel initially. One period

(two rows) on either side of the groove channel is also studied in this Section.
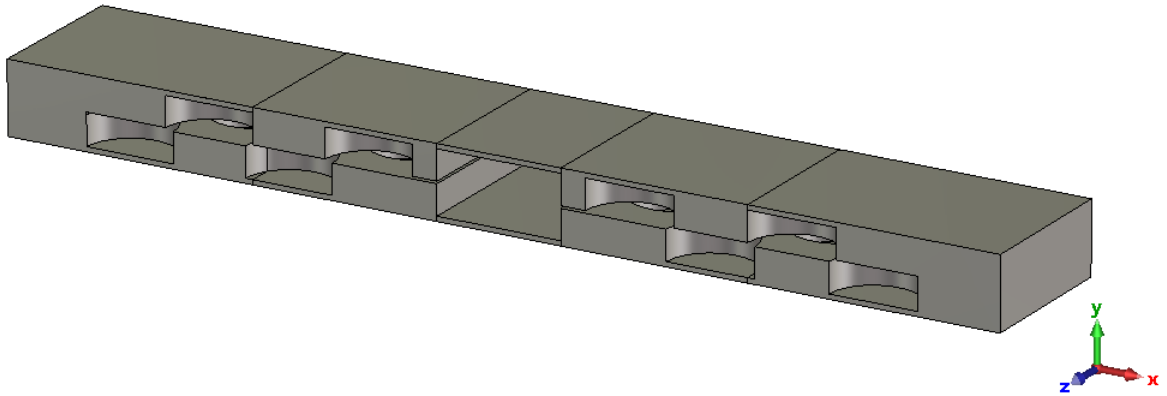
Figure 5-10: Perspective view of the W-band Holey GW.

Figure 5-11 shows the TE$_{10}$ mode of this holey GW, compared to the standard TE$_{10}$ mode found in a regular W-band waveguide with metal walls. The electric field distribution across the *x-z* plane is shown in Figure 5-12. The mode remains similar, except how it dips towards the higher frequencies due to the stopband cutting off the last few higher frequencies between 100 – 110 GHz. The allowed propagation of the TE$_{10}$ mode for the Holey GW is between 80 – 99 GHz.
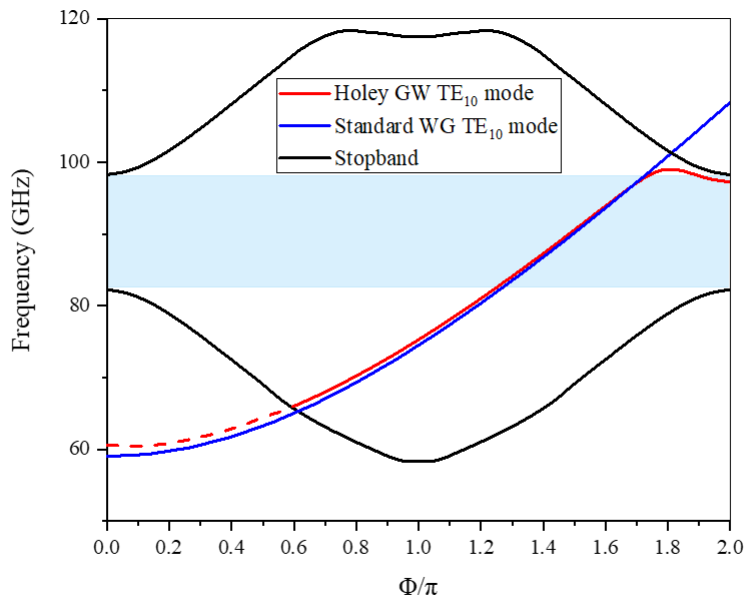
Figure 5-11: TE$_{10}$ mode comparison of the Holey GW and the conventional W-band waveguide.
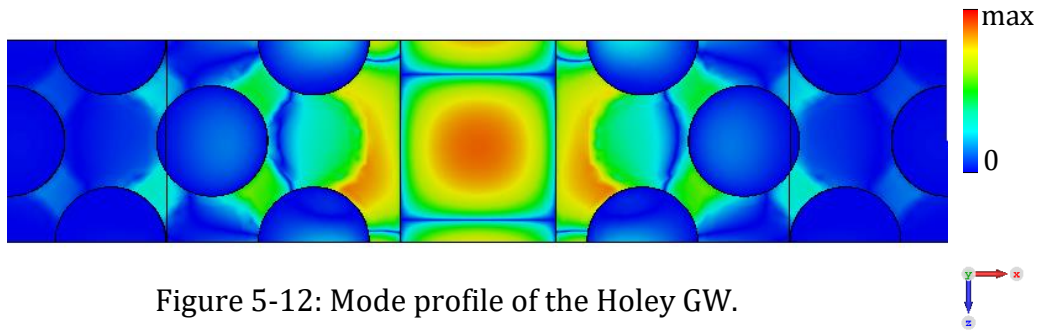
Figure 5-12: Mode profile of the Holey GW.

The Holey glide symmetric gap waveguide-based SWS (Holey GW-SWS) is then optimised. The schematic of the Holey GW-SWS is presented in Figure 5-13.
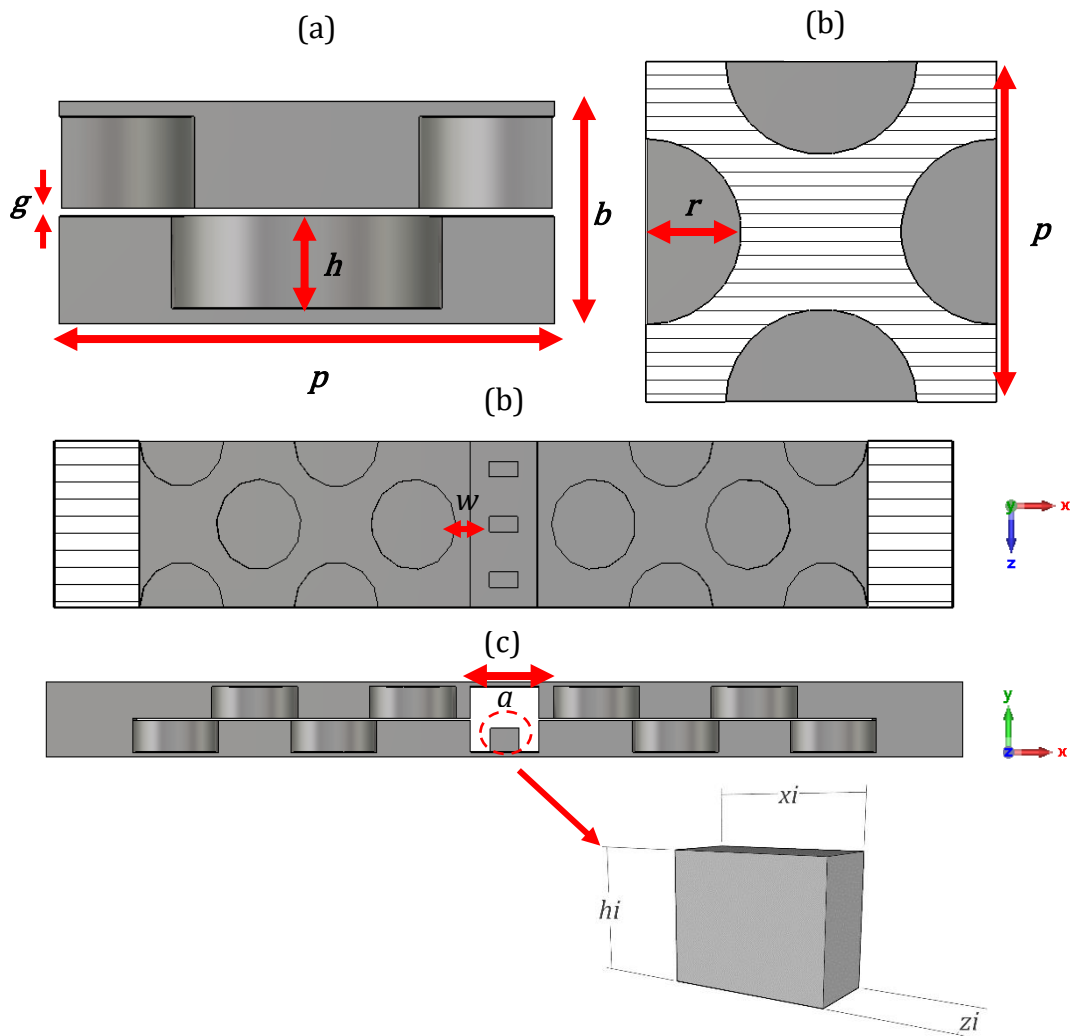
Figure 5-13: (a) Perspective view of the Holey GW-SWS, (b) Top view of the bottom plate, (c) Front view. Dimensions of the central corrugation are a = 1.44 mm, b = 1.27 mm, w = 0.5 mm, xi = 0.6 mm, hi = 0.46 mm, zi = 0.31 mm. Holey GW dimensions are g = 0.05 mm, h = 0.61 mm, r = 0.9 mm, p = 3.3mm.
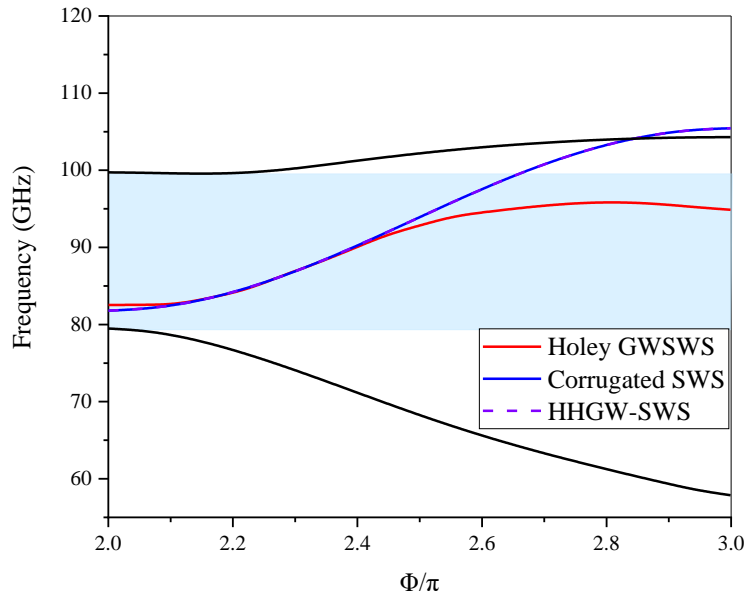
Figure 5-14: Dispersion of the 2-period Holey GW-SWS at *w* = 0.5 mm, compared to the half-height gap waveguide SWS (HHGW-SWS).

Figure 5-14 shows the dispersion of the 2-period (4 rows on each side) Holey GW-SWS in comparison to the half-height gap waveguide SWS (HHGW-SWS) for the first space harmonic. It can be seen how there is matching of dispersion with the HHGW-SWS up until beyond 95 GHz. Due to the multi-period nature of the SWS, the initial numerical data needs postprocessing to be plotted on the basis of the typical folding of the bands experienced by simulating more than one period between periodic boundaries. The mode profile supports how propagation occurs up until 95 GHz. Typically, the field of the z-component is concentrated within the channel above the central corrugations. The field of the higher frequency on the Holey GW-SWS transmits and concentrates in the gap of the holes and does not propagate very strongly within the channel beyond 95 GHz. While a small amount of electric field concentration in the gap is expected in the holey glide symmetric structure, shown in [75], for the Holey GW-SWS the concentration is much higher at the 95 GHz mark compared to the lower frequency points. Figure 5-15 demonstrates the electric field profiles of the Holey GW-SWS at 88.5 GHz, compared to at above 95 GHz.

130

(b)
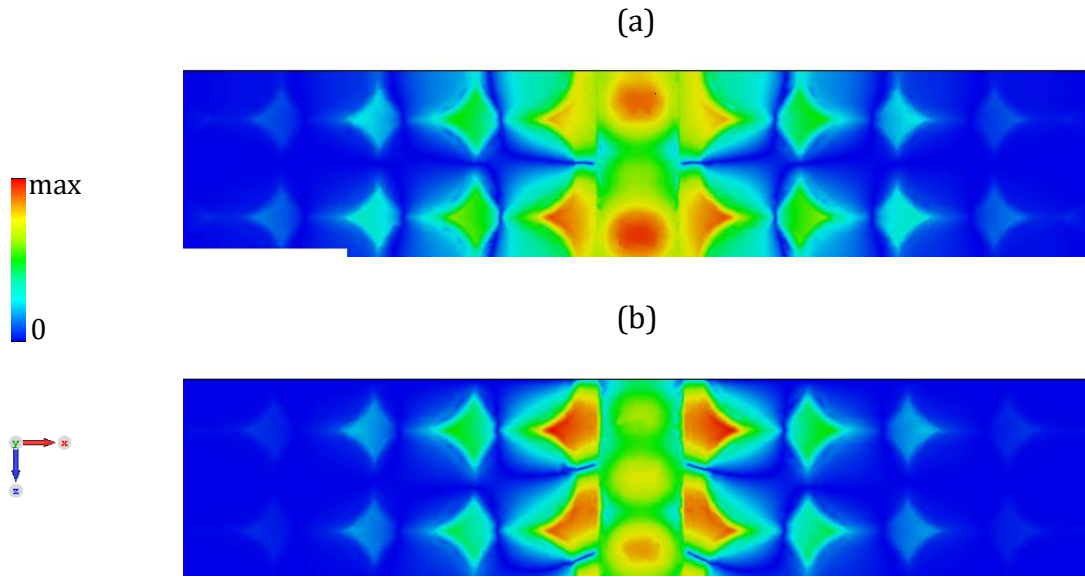
Figure 5-15: Mode profiles of the Holey GW-SWS at (a) 88.5 GHz, (b) 96 GHz.

A comparison of the stopbands at various stages of design are shown in Figure 5-16 – the unit cell, the electric boundary unit cell, the W-band TE_{10}, and the Holey GW-SWS stopband.
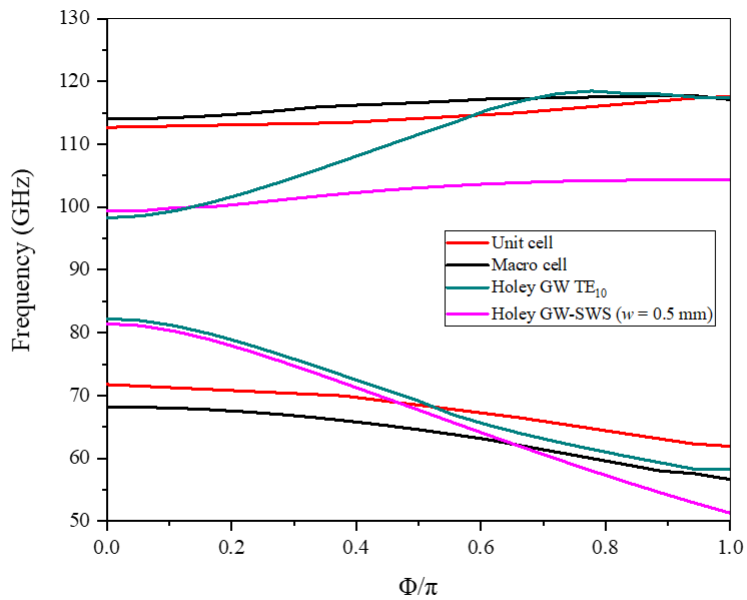
Figure 5-16: Comparison of the stopband found at each point in design characterization.

The Holey GW-SWS is also simulated with just one period (2-hole rows), in Figure 5-17. Using less periods can be advantageous as a more compact structure can be designed. A similar dispersion output is achieved in this case. The 1-period Holey GW-SWS is demonstrated with both $w = 0.3$ mm and $w = 0.5$ mm.
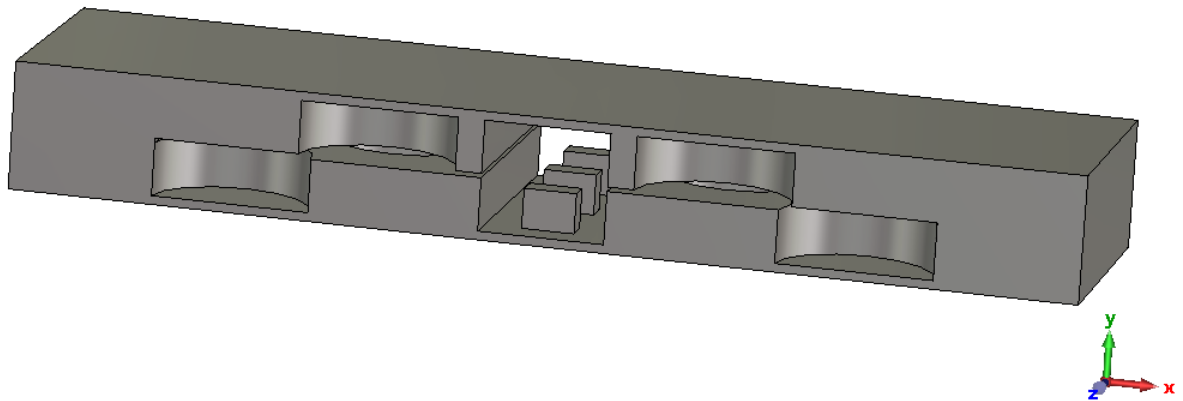
Figure 5-17: Perspective view of the 1-period Holey GW-SWS.
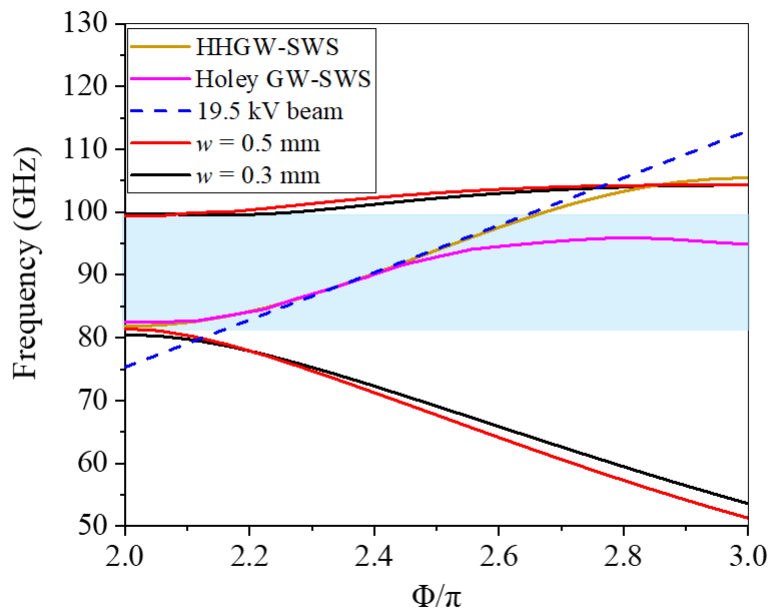
Figure 5-18: Dispersion of the 1-period Holey GW-SWS, compared to the HHGW-SWS. A 19.5 kV beamline is superimposed to show the area of synchronicity. The stopband for the structure is demonstrated with a wall thickness of w = 0.3 mm and w = 0.5 mm.

Figure 5-18 shows the area of synchronicity for the Holey GW-SWS. With a 19.5 kV beam, this is obtained in the frequency range of 86 – 94 GHz. Figure 5-19 shows the mode profiles, and an apparent change in the distribution of the electric field after 95 GHz can be observed.

(a)

(b)

(c)

(d)
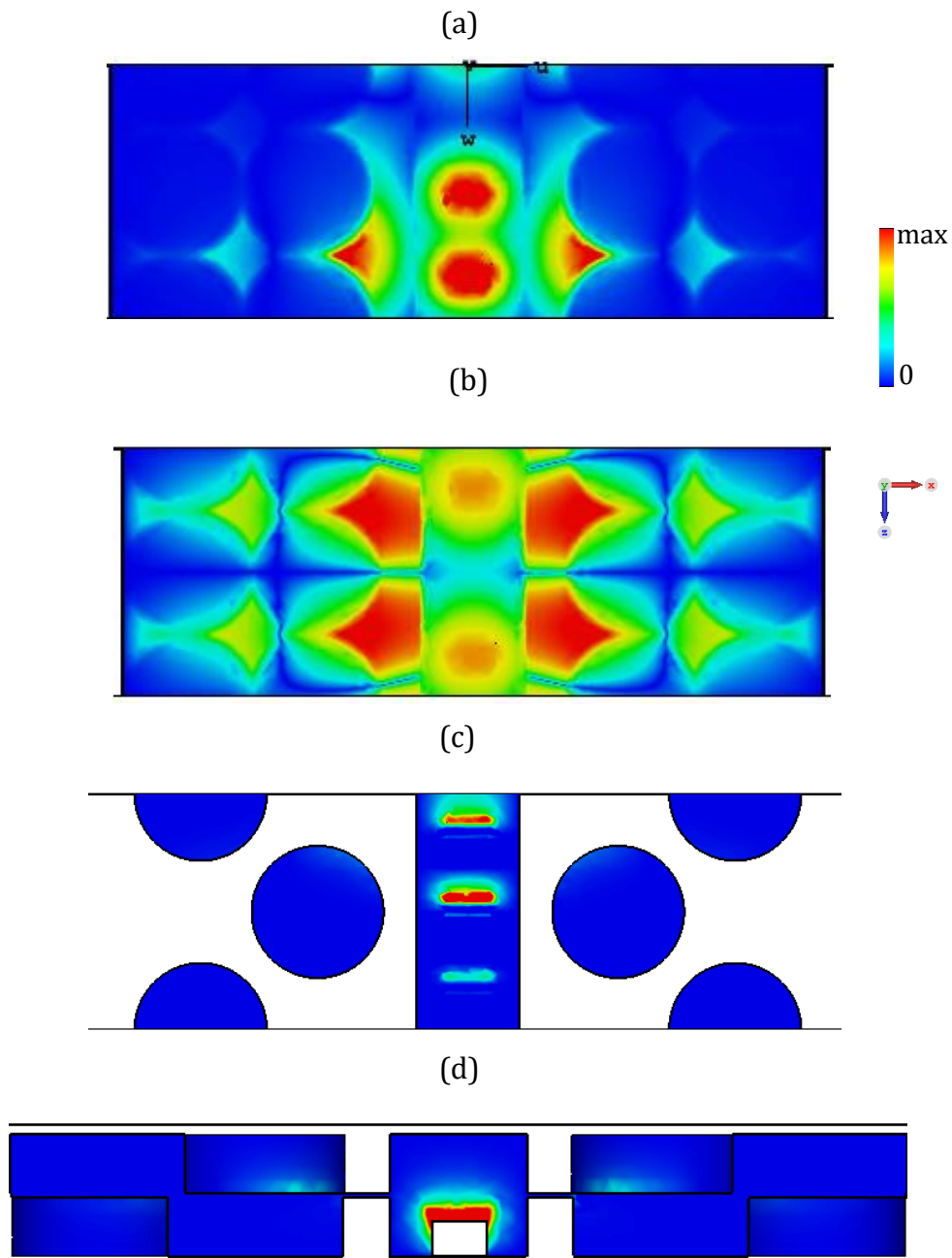
Figure 5-19: Mode profiles of the 1-period Holey GW-SWS for (a) 88 GHz, (b) 95 GHz (c) E_z field component at 88 GHz (d) E_z field component in the transverse plane.

5.4   The WR-10 back-to-back coupler design for the Holey GW

A design of the WR-10 holey glide symmetry waveguide coupler is considered next to study mode propagation. These simulations were run in the time domain using a perfect electric conductor (PEC). The W-band TE_{10} mode ranges from 60 – 110 GHz. When the stopband is introduced, this should theoretically filter the local waves from within the stopband and not allow transmission, while a TE_{10} W-band mode to propagate within the stopband frequency range. In the 2-period case, Figure 5-20 shows the schematic of the WR-10 Holey GW back-to-back coupler. Figure 5-21 shows that transmission is achieved

(a)

(b)
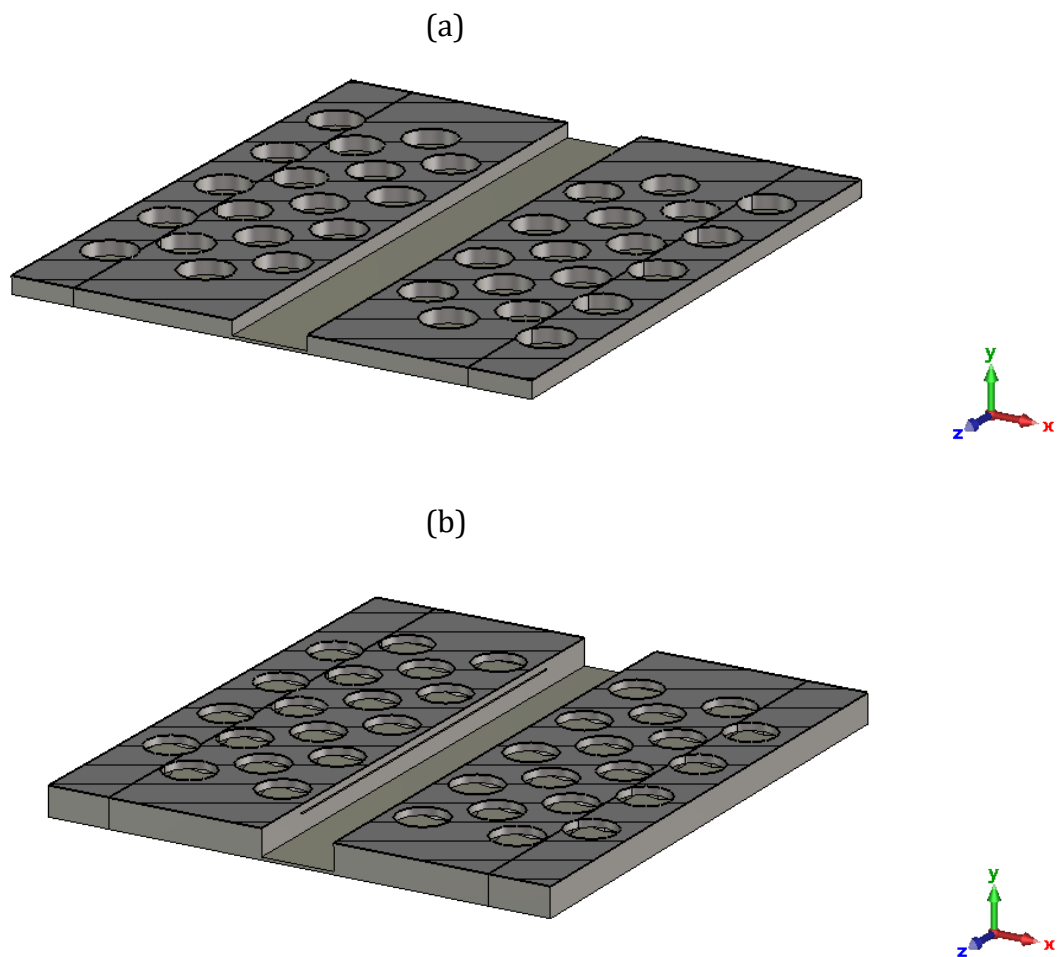
Figure 5-20: Perspective view of the W-band WR10 back-to-back coupler (a) Bottom plate, (b) Top plate. b
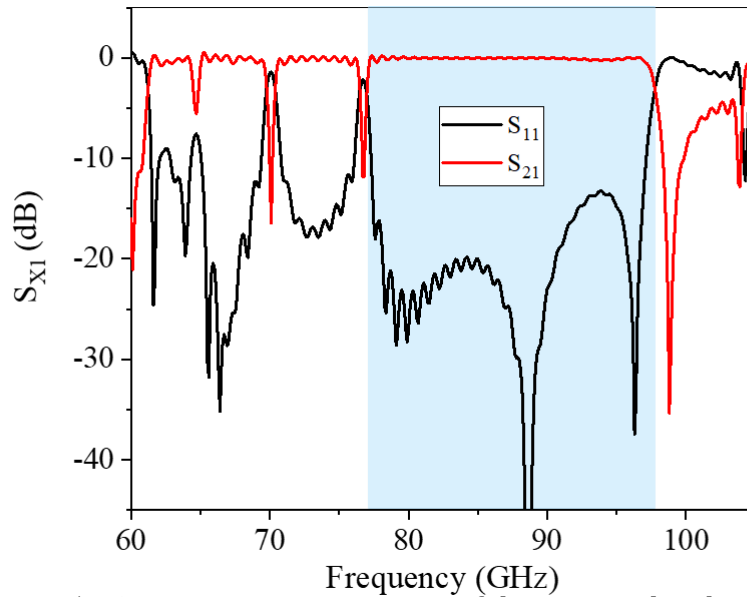
Figure 5-21: Scattering parameters of the 2-period W-band WR10 back-to-back coupler.

In the "pockets" of transmission that occur, there is still visible propagation of the mode in the field profiles. For instance, at 72.5 GHz, Figure 5-21 shows transmission is occurring at this frequency point. This can then be verified in the field profile in Figure 5-22. In contrast, where a reflection peak is seen at 76.75 GHz, the field dissipates in Figure 5-23. For comparison, Figure 5-24 shows the mode profile of the transmission of the frequency point 85 GHz within the operating band.
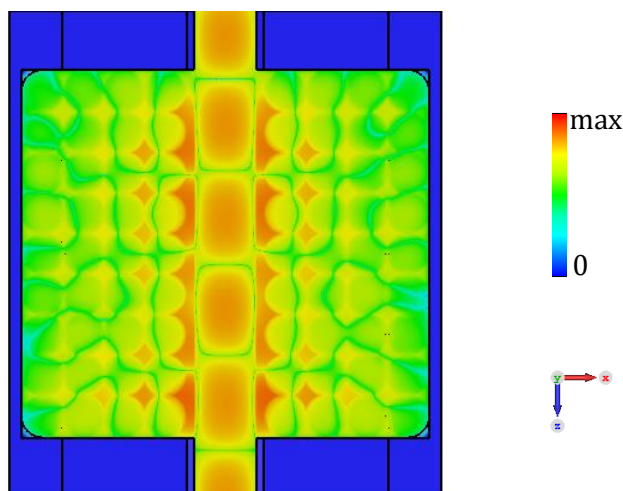
Figure 5-22: Field profile for the 2-period W-band WR10 back-to-back coupler at 72.5 GHz.
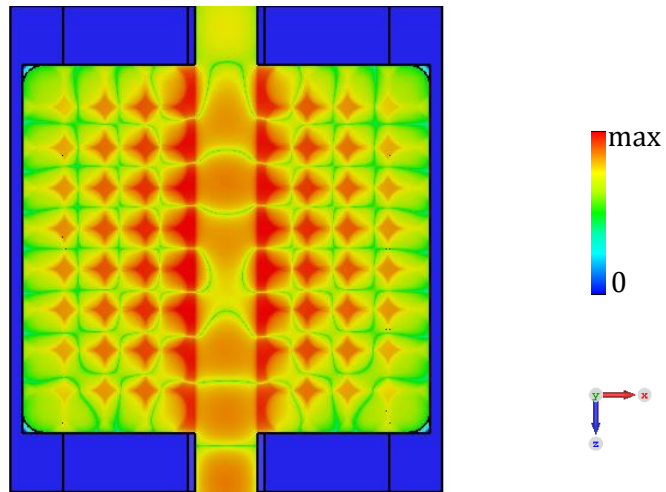
Figure 5-23: Field profile for the 2-period W-band WR10 back-to-back coupler at 76.75 GHz.
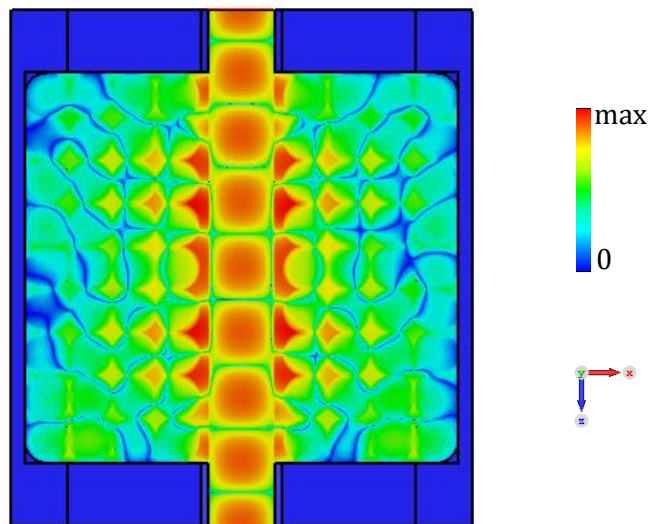
Figure 5-24: Field profile for the 2-period W-band WR10 back-to-back coupler at 85 GHz.

In the 1-period case, in Figure 5-25, the stopband ranges from 80 – 100 GHz. When looking at Figure 5-26, this becomes apparent. Practically, transmission cannot be completely blocked off outside the stopband unless the number of periods of the gap waveguide are increased. However, there is a clear range of good transmission between 80 – 100 GHz.

(a)

(b)
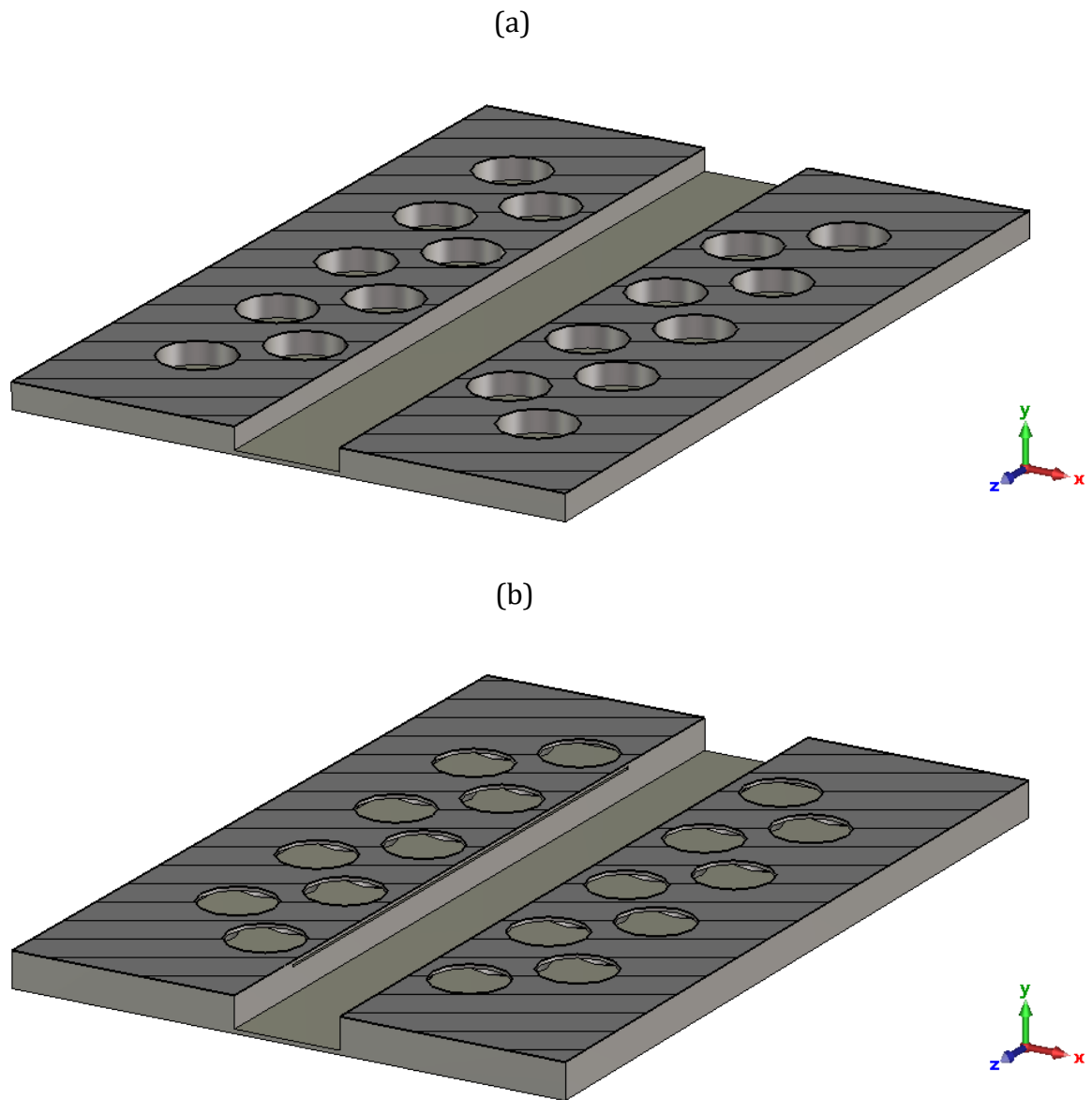
Figure 5-25: View of the W-band WR10 back-to-back coupler (a) Bottom plate, (b) Top plate.
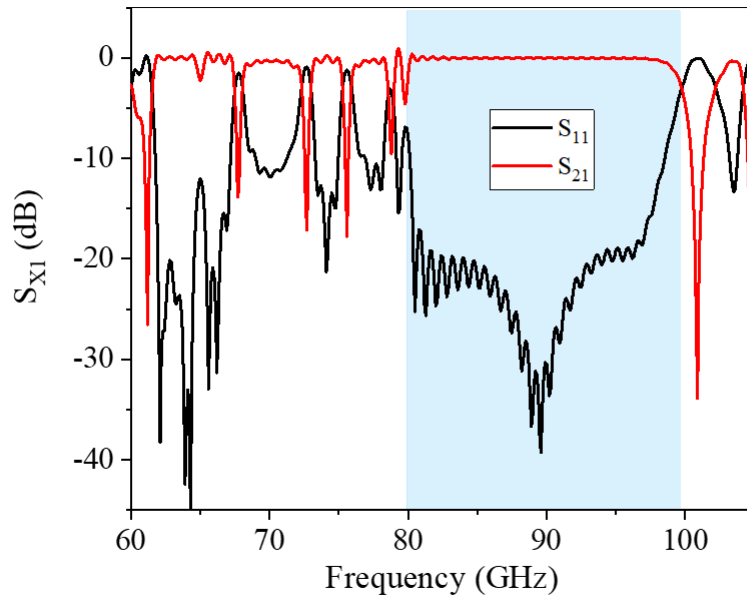
Figure 5-26: Scattering parameters of the 1-period W-band WR10 back-to-back coupler.

5.5   The Holey GW-SWS back-to-back coupler design

Figure 5-27 shows the schematic of a 10-interaction period, 20-period tapering of the back-to-back coupler structure, similar to what is used in Chapter 4. Increasing the wall thickness from w = 0.3 mm to w = 0.5 mm does improve the reflections within the frequency band, and this comparison is presented in Figure 5-28. While the use of w = 0.3 mm gives an S_{11} around -10 dB, w = 0.5 mm provides an S_{11} of around -15 dB. The use of one period (2 rows) of holes was found sufficient for this structure. The frequency band is 83 – 94 GHz. The electric conductivity of the material, copper, was set as the ideal value 5.96 x10^7 S/m. These simulations were run in the frequency domain for increased accuracy.

138
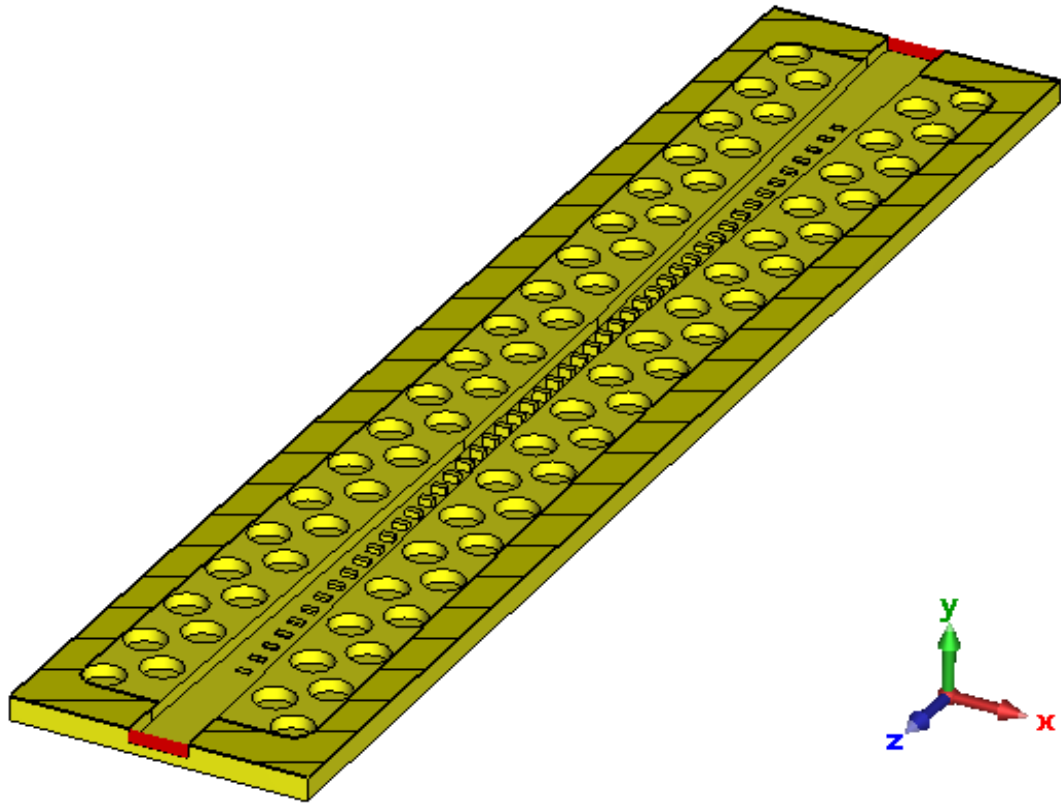
Figure 5-27: Back-to-back coupler design for the Holey GW-SWS.
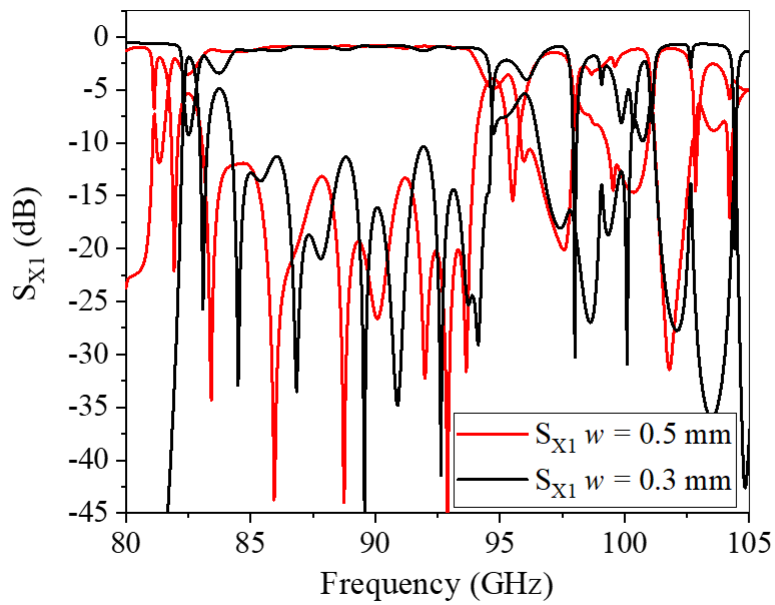
Figure 5-28: Scattering parameters of the Holey GW-SWS back-to-back coupler when w = 0.5 mm and w = 0.3 mm.

5.6   Holey gap waveguide-based TWT design

As the simulation of the interaction impedance is not straightforward due to the nature of the multi-period SWS, a particle-in-cell simulation of the TWT can give insight on the feasibility of the SWS for the TWT design. It is expected that the variation of the geometry generating the stopband will not significantly affect the interaction impedance.

Initial PIC simulations of this structure use 3 periods of holey gap waveguide on either side, 91 propagating periods, a 20-period tapering of the SWS on either side, with a constant width from the coupler wall to the edge of the holey configuration of $w = 0.7$ mm to couple with a standard W-band (2.54 mm x 1.27 mm) waveguide. Increasing the number of rows of the holey structure from 1 period to 3 periods seems to allow slightly better synchronism with a 21 kV beam and were added in the PIC simulations to ensure better enforcement of the stopband, as seen in Figure 5-30. A conventional H-plane bend is implemented to house the beam tunnel (1.3 mm x 0.35 mm), Figure 5-29. A beam (1 x 0.2 mm) with 21 kV is simulated. With a beam current of 0.3 A, oscillations were generated in the TWT. TWT oscillation is a common and critical issue found when designing at high frequencies [77], [78]. The reasons can be poor matching of the ports which causes a reflection that builds up in time, too high current of the beam [79], too many periods (going beyond gain saturation), too high input power, or interaction with a higher order mode. Linked to the matching at the ports, band edge oscillation is a common concern [79], [78], which is considered here to show the capability of gap waveguides in filtering out unwanted frequency propagation. Implementing a high gain TWT in this structure allows us to explore the options in which potential oscillations in a TWT can be improved.
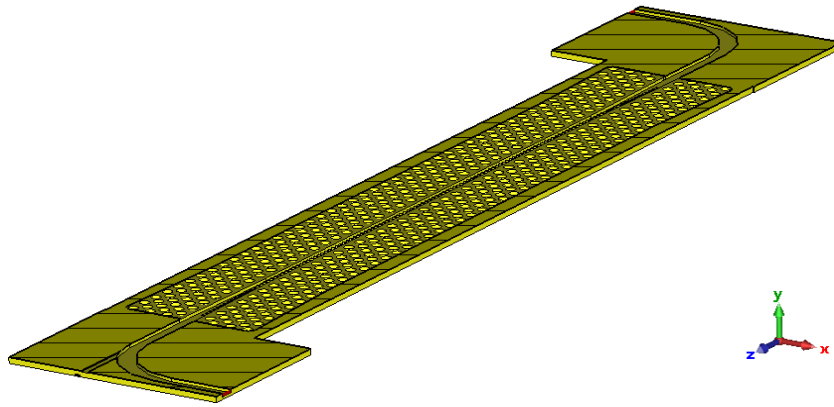
Figure 5-29: Perspective view of the 3-period Holey GW-SWS TWT.

The most notable improvement for this structure came from reducing the beam current. Reduction in beam current in turn reduces gain which typically dampens oscillation of a structure, with the unintended benefit of reduction in beam curling.

While oscillation does not occur with these measures in place, small peaks in the FFT indicate that there is unwanted frequency propagation within the channel still potentially occurring, which can lead to potential oscillations as the TWT continues to operate for a longer period of time. The main change that can be made which can alter the stopband without completely changing the mode dispersion of the structure, and thus the beam synchronism with the signal, is the wall thickness w. The dispersion of the 3-period Holey GW-SWS at w = 0.7 mm and w = 0.9 mm is shown in Figure 5-30, with the mode profile shown in Figure 5-31. A minimum thickness of w = 0.7 mm is required to allow propagation of the signal to occur and not be reflected into the port, while increasing further to w = 0.9 mm reduced the FFT frequency peaks of the output signal at 87 GHz, shown in Figure 5-33. The PIC simulations are run for 20ns to ensure sufficient time is given for possible oscillation to establish. As it can be seen in this Figure, increasing the wall thickness not only makes machining easier, but also dampens some of the frequency peaks, such as at 95 and 99.5 GHz. The fact that the 99.5 GHz peak was not removed

141

entirely indicates that there is an inherent mismatch at this frequency point, and optimization is required of the SWS mode dispersion or coupler. The mode profile does however show a significant reduction in the electric field (Figure 5-31) at the 99.5 GHz peak when using w = 0.9 mm compared to w = 0.7 mm. The stopband where w = 0.9 mm covers 83 – 95 GHz, which may then dampen the propagating mode beyond 95 GHz.

(a)

(b)
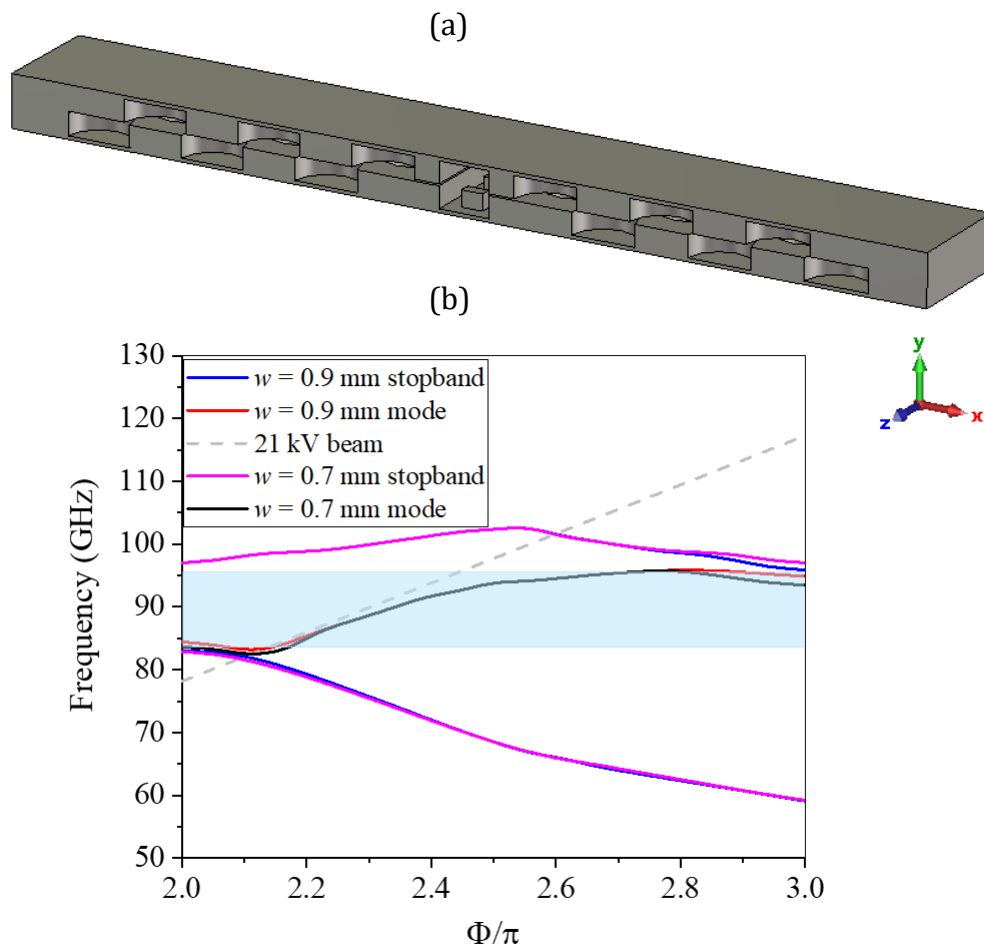
Figure 5-30: (a) Schematic of the 3-period Holey GW-SWS, (b) Mode dispersion of the 3-period Holey GW-SWS at w =0.7 mm and w = 0.9 mm with a 21 kV beam superimposed over.
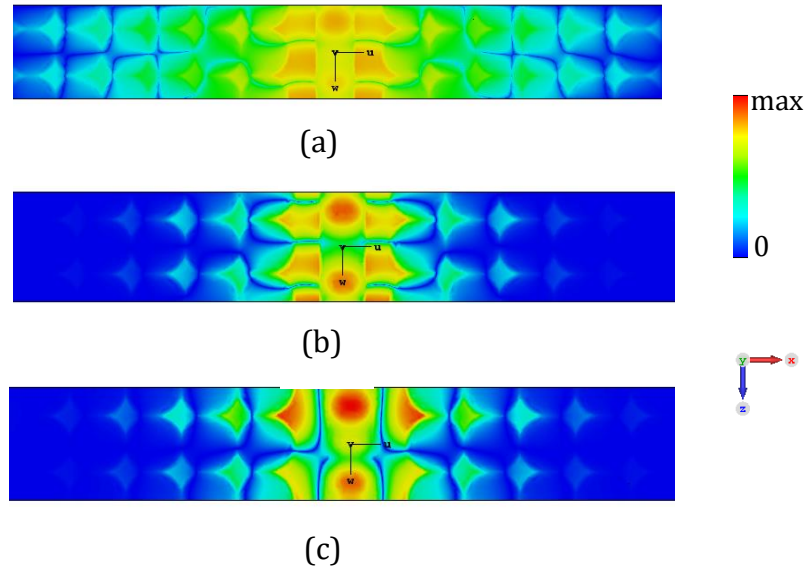
Figure 5-31: (a) *w* = 0.9 mm at 99.5 GHz, (b) *w* = 0.7 mm at 99.5 GHz, (c) *w* = 0.9 mm at 87 GHz.
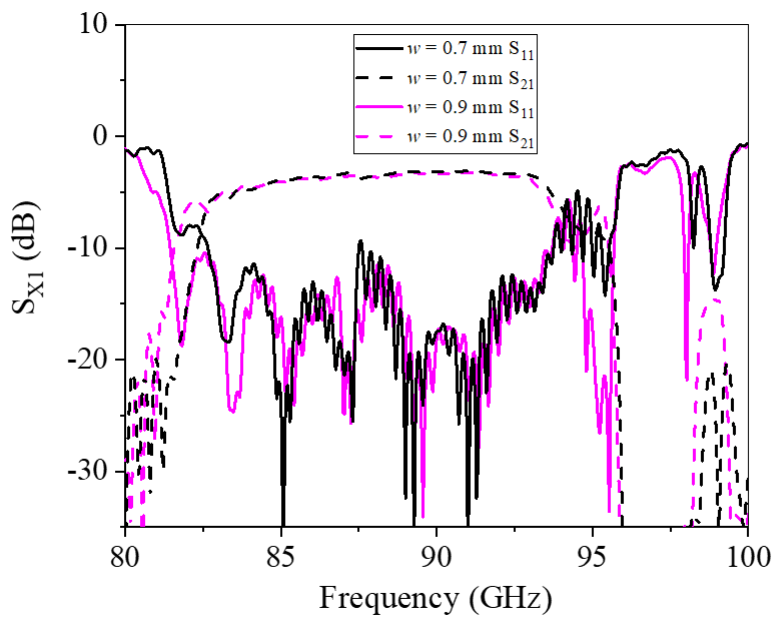
Figure 5-32: Scattering parameters of the 91-period Holey GW-SWS TWT at *w* = 0.7 mm and 0.9 mm. The electric conductivity of the copper is 5.96x10^7 S/m.

The bandwidth where *w* = 0.9 mm is 83 – 93 GHz, shown in Figure 5-32. Increasing the

value *w* can dampen unwanted peaks without the requirement of fundamentally

changing the mode dispersion. However, the drawback is that increasing this dimension

also slightly dampens the gain of structure.

(a)

(b)
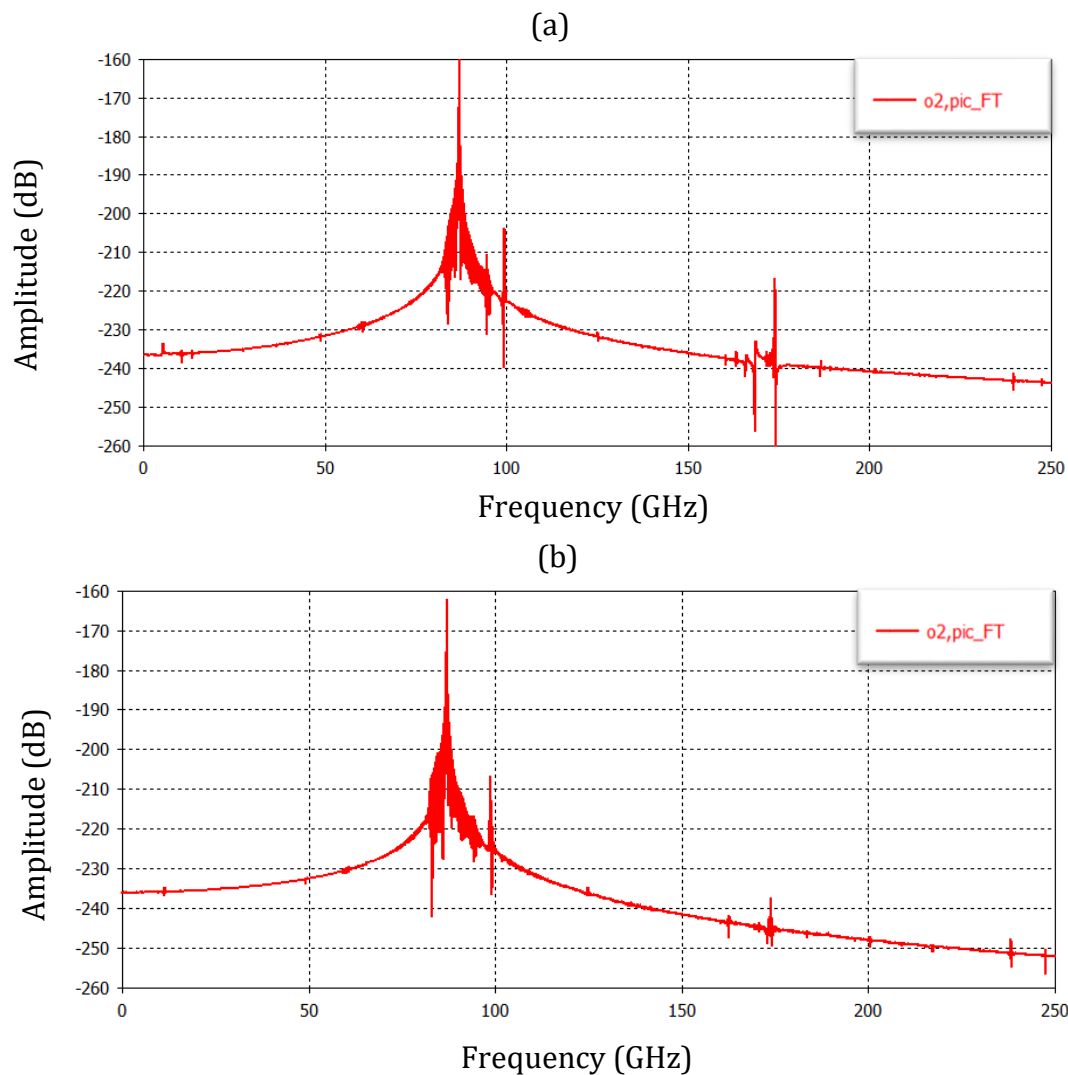
Figure 5-33: Spectral purity of the Holey GW-SWS TWT at 87 GHz when (a) *w* = 0.7 mm, (b) *w* = 0.9 mm.

Looking at the tube stability equation:

$$Q = G - |S_{11}| - |S_{22}| - |S_{21}| < 0 \tag{1}$$

The tube stability factor for this designed TWT is a maximum gain of 25 dB. With an 0.3

A beam current, a gain of above 25 dB is achieved, deeming the initially designed TWT

144

unstable. Hence, with the current reduced, an electron beam of the following parameters (1 x 0.2 mm, maximum beam current 0.09 A, 21 kV beam), and a wall thickness of w = 0.9 mm, the final tube design is stable. The beam voltage was optimised to 21 kV, providing the highest signal gain.

Table 5-2: Gain achieved with various beam voltages. 21 kV provides the highest gain at 88.5 GHz.

Beam voltage (kV)	Gain (dB)
19.5 kV	-6.08242
20.5 kV	10.99
21 kV	17.01562
21.5 kV	0.537443
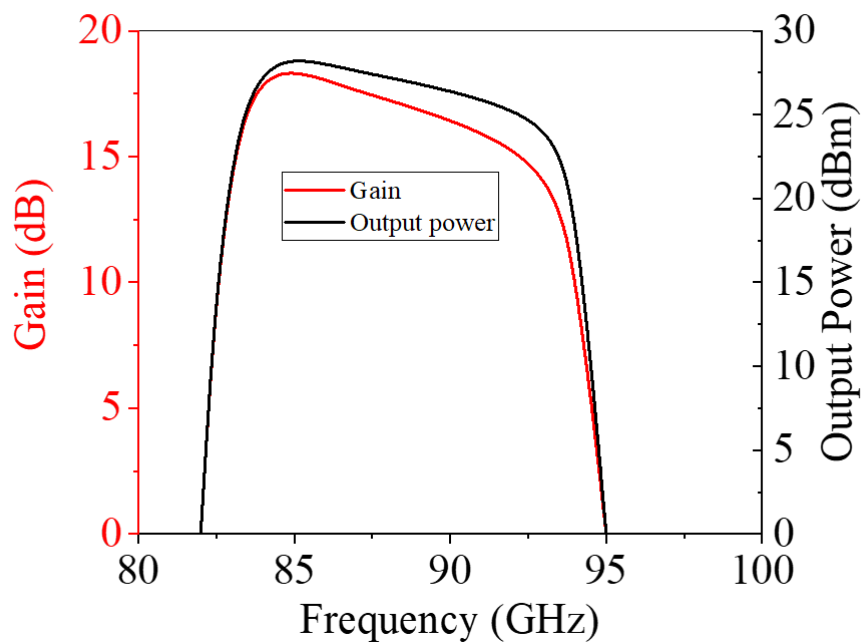
Figure 5-34: Gain and output power plotted against the frequency provided by the Holey GW-SWS TWT.
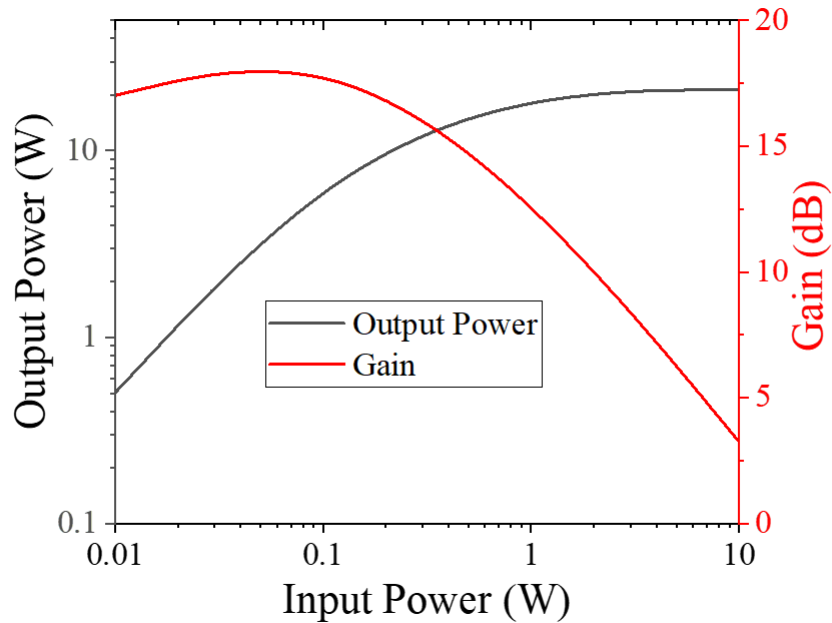
Figure 5-35: Logarithmic plot of output power and gain against
input power for the Holey GW-SWS TWT at 87 GHz.

The final SWS provides reflections of -12 to -15 dB, and a gain of 15 – 18 dB for the 3 dB
TWT operating bandwidth of 83 – 93 GHz (Figure 5-34) with an input power of 0.01 W in
the linear region. Figure 5-35 shows the output power and gain in relation to the input
power at 87 GHz. The maximum output power is at around 21 W at an input power of
approximately 1 W at 85 GHz. The reason for the relatively lower gain is due to the
reduction of current. This can be increased after mode optimisation. Further optimization
of the coupler was attempted, however, to obtain improved gain and reduced scattering
parameters, integration of a holey gap waveguide-based coupler bend would need to be
considered to adequately reduce reflections and better beam synchronism as discussed
in further work in Chapter 6.

5.7   Conclusion

A new holey glide symmetric gap waveguide SWS is presented to characterize the capabilities of this gap waveguide topology for the design of TWTs SWS. Initial numerical simulations show that the structure can operate as an amplifier between 83 – 93 GHz. The main advantage is the simplicity of machining which only involves drilling of holes for the gap waveguide and larger period. This may ease repeatability in TWT fabrication and lower costs, as compared to other gap waveguide designs.

Due to the dispersion characteristics found for the Holey GW-SWS, synchronism bandwidth for TWT operation was reduced as compared with the pin-based SWS configurations. Also, PIC simulations of this structure suggest oscillations within the tube arise for the same beam parameters and gain level that were presented in Chapter 4. Even reducing the beam current and consequently gain, less spectral purity was obtained in output. Another limitation on this structure is that it does appear to inherently have higher electric field concentration situated in between the gap, compared to pin-based gap waveguide structures. A parametric study of the design geometry has shown partial improvement in this respect with varying of the metal wall spacing dimension, w. The obtained results evidence that a more thorough study of the optimum SWS mode dispersion should be conducted, including also different longitudinal loading for the central channel. Additionally, an integrated coupler structure based on the same GW topology should be considered as further work to fully assess the potential of this geometry.

CHAPTER 6: CONCLUSIONS AND FUTURE WORK

6.1 Summary of the outcomes of this work

One of the major trends in the development of modern electronics has been to increase the frequency of operation to access a wide range of novel, disruptive applications such as those underpinning the next generation of high-capacity high-speed wireless communication networks (both terrestrial and space). However, power scales inversely with frequency which limits, by order of magnitudes, the achievable power level. This limitation is particularly severe for accessing wireless communications at the millimetre waves due to the power requirements to overcome the atmospheric attenuation at this range, highly dependent on the presence of humidity and chance of rain. Vacuum electronics today offer the only technological solution to provide sufficient power at the transmitter and travelling wave tubes (TWTs) power amplifiers, that can be scaled at these frequencies while ensuring moderate costs and robustness against the tight tolerances intensively sought. This work has addressed some of challenges of developing repeatable, cost-effective, and compact TWTs for the upper millimetre wave range by introducing the properties of gap waveguides in the design process of the TWT SWS.

This technology has proven effective in the dampening of higher order modes, a critical issue to reduce the risk of oscillations in TWT operation, especially those operating with sheet electron beams, while providing relatively simple fabrication. The work has focused on designing the metal enclosure of the SWS based on gap waveguide technology, where the interaction with the beam is set by a central corrugation loaded along the waveguide. First, for simplicity, the pin-based gap waveguide was investigated. Two structures have been proposed on the basis of this geometry, the FPGW-SWS and the HHGW-SWS, which

149

both hold potential as frequency selective, flexible designs for mm-wave SWSs. Dispersion characteristics and interaction impedance were presented and optimised for wide band interaction approximately in the 90 – 100 GHz range. It was shown that while conventional design guidelines for the pin gap waveguide are useful for initial dimensions selection, more leeway exists for the gap size and pin height value design, and these parameters can be selected according to other requirements such as operation bandwidth for the SWS mode and stopband.

The complete design of an integrated gap-waveguide input-output coupler including the beam tunnel for the sheet electron beam was presented. The flexibility of this technology allows to easily adapt the design for very wide aspect ratio sheet beams, which alternatively would require the integration of complex mismatching circuits to isolate the resulting above cut-off beam tunnel dimensions. Due to the added benefits provided by the HHGW-SWS with respect to the FPGW-SWS, such as short aspect ratio pins and compact coupler design, this structure was selected for fabrication and PIC simulation purposes. The scattering parameters and modal bandwidth of the HHGW-SWS have been experimentally verified for the prototype version, with transmission losses of around 1 dB for a reduced conductivity simulation, and reflections of below -15 dB. A gain of minimum 25 dB was achieved in the 89 – 99 GHz 3dB-bandwidth, with a saturated output power of 160 W at an input power of 1 W at 93.5 GHz. Numerical and experimental results demonstrate that the gap height is a particularly sensitive parameter in determining the lower cut-off frequency point of the SWS mode. This can potentially reduce the effective TWT operation band. However, current fabrication techniques ensure sufficient dimensional accuracy to satisfy the required tolerances on the gap dimension.

150

The later section of the thesis focused on an alternative geometry of the gap waveguide. Based on the same central corrugation as above, a novel holey glide symmetric gap waveguide SWS is investigated. In literature, this gap waveguide topology has been presented to provide a comparatively broader stopband width. It was found through simulations that while stopband can be broad, its width did not increase significantly with respect to the previously considered pin-based structure. To note, the stopband is more evidently impacted by the inclusion of a central groove and longitudinal loading of this with corrugations. Results have suggested that the holey gap waveguide plays a more significant role in determining the dispersion characteristics of this SWS topology. A thorough parametric study is conducted on the unit cell to find the optimised dimensions for a W-band TWT design. Scattering parameters of a complete SWS design and PIC simulations are conducted to determine the beam-wave interaction properties. It was found that this design could be susceptible to oscillations. Several mitigations were put in place to greatly reduce oscillations, such as designing the stopband to filter the unwanted oscillating frequency, but complete spectral purity was not achieved. This is likely due to the SWS design requiring further optimisation. This structure is still of great interest due to its potential for easier fabrication, repeatability, wideband operation and moderate output power. The Holey GW-SWS operates between 83 – 93 GHz with a maximum output power of 21 W.

6.2 Implications for future technology

As of 2023, 5G is currently being rolled out for consumer use internationally. With the increased rates of remote working and increased requirements of large amounts of data being transmitted in a very short period, data transmission beyond 5G will be the reality

in years to come. High power, high frequency devices which can transmit multigigabit-per-second can provide the baseline for a network of ultrafast data transmission.

Fabrication technology has been improving vastly day by day. While these designed structures may not yet be at the standard of batch production, in these years to come the pin-based and hole-based waveguides may be viable for mass production, hence, successful rollout for use in multigigabit data transmission for public use.

6.3   Limitations

Currently, there is a limitation in the successful repeatable fabrication and implementation of these structures, considering the many proposed simulated structures in the literature which ultimately were not successfully realised. While fabrication techniques are rapidly improving, there is work to be done before reliable, quick, and economically viable fabrication of even the pin-based proposed structures is available. This thesis puts an emphasis on simple design, which would be the most realistic for widespread applications.

For the holey-based gap waveguide, current research is very limited on any mm-wave devices. Before any practical work can be conducted, further investigation is required to better understand the nature of the structure. While the current results presented in this thesis show potential, further work is required for definitive conclusions on the benefits and limitations provided by this design.

In summary, the work in this thesis has numerically demonstrated the suitability of gap waveguide concepts to support the development of compact, flexible and cost-effective millimetre wave SWSs for the design and realisation of wideband, stable and relatively

high power TWT operation. The presented technology is scalable to higher frequency ranges where it can be especially suitable for realisation via LIGA process and can be extended in principle to other types of SWSs than the corrugated waveguide.

6.4 Further research

To successfully demonstrate the practical application of the pin-based gap waveguided TWT, a hot test of the full TWT (including magnetic focusing system, electron gun, assembled, bonded and vacuum tight enclosure) is required which are beyond the scope of this project. However, if the structure is to be used in a practical sense, the continuous operation of the TWT should be experimentally demonstrated. Further work should look at the machining of the TWT-length SWS in copper and bonding process of the two halves prior experimental verification.

Another direction of further work relates more investigation into the full potential of the glide symmetric holey gap waveguide, where dispersion characteristics improvement for wider band operation should be addressed with the implementation of a holey glide symmetric gap waveguide-based bend to optimise reflection/transmission characteristics (matching) and consequently tube stability. Additionally, the introduction of a two-section TWT with a sever could be explored to effectively eliminate oscillations commonly encountered in high frequency TWTs [80].

With the continued effort and research in developing slow wave structures and improving fabrication techniques, gap waveguide technology can be a forefront in furthering the race towards successful and commercial implementation of high frequency TWTs for fast, reliable data transmission.

153

155

REFERENCES

[1] C. Paoloni, D. Gamzina, R. Letizia, Y. Zheng and N. C. L. Jr., "Millimeter wave traveling wave tubes for the 21st Century, Journal of Electromagnetic Waves and Applications," *Journal of Electromagnetic Waves and Applications,* 2020.

[2] D. F. G. Minenna, J. Puech, Y. Elskens, F. Doveil, F. André, J.-F. Auboin and É. Duverdier, "The traveling-wave tube in the history of telecommunication," *The European Physical Journal H,* vol. 44, pp. 1 - 36, 2019.

[3] A. Seabaugh, "The Tunneling Transistor," IEEE Spectrum, 2013.

[4] C. &. P. Industries, "Helix TWTs," [Online]. Available: https://www.cpii.com/product.cfm/1/19/64. [Accessed June 2023].

[5] M. Field, T. Kimura, J. Atkinson, D. Gamzina, N. C. Luhmann, B. Stockwell, T. J. Grant, Z. Griffith, R. Borwick, C. Hillman, B. Brar, T. Reed, M. Rodwell, Y.-M. Shin, L. R. Barnett, A. Baig, B. Popovic, C. Domier, R. Barchfield, J. Zhao, J. A. Higgins and Y. Goren, "Development of a 100-W 200-GHz High Bandwidth mm-Wave Amplifier," *IEEE Transactions on Electron Devices,* vol. 65, no. 6, pp. 2122-2128, 2018.

[6] 5. t. 6. G. S. T. A 75 Watt, "Helen Limburg; Diego Zamora; Jon Davis; Ivo Tammaru," Lewis Research Centre, California, 1995.

[7]   H. Cheng, X. Zhu, F. Hou, W. Wang, L. Shen and S. Hu, "Compact 31-W 96-GHz Amplifier Module in GaN-MEMS for Wireless Communications," *IEEE Transactions on Microwave Theory and Techniques,* vol. 70, no. 2, pp. 1233 - 1241, 2022.

[8]   A. M. Cook, E. L. Wright, K. T. Nguyen, C. D. Joye, J. C. Rodgers, R. L. Jaynes, I. A. Chernyavskiy, F. N. Wood, B. S. Albright, D. K. Abe, J. P. Calame, B. Levush, D. E. Pershing, J. Atkinson and T. Kimura, "Demonstration of a W-Band Traveling-Wave Tube Power Amplifier With 10-GHz Bandwidth," *IEEE Transactions on Electron Devices,* vol. 68, no. 5, pp. 2492 - 2498, 2021.

[9]   "TWEETHER," [Online]. Available: https://www.lancaster.ac.uk/engineering/research/emit/tweether/. [Accessed May 2023].

[10] "ULTRAWAVE," [Online]. Available: www.ultrawave2020.eu. [Accessed May 2023].

[11] Z. Liu, J.-Y. Deng and D. Sun, "Slow-Wave Groove Gap Waveguide Bandpass Filter," *IEEE Access,* p. 1, 2019.

[12] E. Pucci, "Gap Waveguide Technology for Millimeter Wave Applications and Integration with Antennas," 2013.

[13] R. J. Barker, N. C. Luhmann, J. H. Booske and G. S. Nusinovich, Modern Microwave and Millimeter-Wave Power Electronics, Wiley-IEEE Press, 2005.

[14] A. Gilmour, Principles of Travelling Wave Tubes, 1994.

[15] L. Stark, "Electromagnetic waves in periodic structures," 1952.

[16] R. Carter, Microwave and RF Vacuum Electronic Power Sources, 2018.

[17] U. Chipengo, "Novel Concepts for Slow Wave Structures used in High Power Backward Wave Oscillators".

[18] G. M. S. Santos, C. C. Xavier and C. C. Motta, "A study of a PPM focusing system for a C-band power TWT," in *2011 SBMO/IEEE MTT-S International Microwave and Optoelectronics Conference (IMOC 2011)*, Natal, 2011.

[19] Dassault Systemes, *CST Studio Suite.*

[20] C. S. Suite, "ELECTROMAGNETIC SIMULATION SOLVERS," Dassault Systemes, [Online]. Available: https://www.3ds.com/products-services/simulia/products/cst-studio-suite/solvers/. [Accessed June 2023].

[21] X. Shi and et al, "Study on Wideband Sheet Beam Traveling Wave Tube Based on Staggered Double Vane Slow Wave Structure," *IEEE Transactions on Plasma Science,* vol. 42, pp. 3996-4003, 2014.

[22] C. Paoloni, M. Mineo, M. Henry and P. G. Huggard, "Double Corrugated Waveguide for Ka-Band Traveling Wave Tube," *IEEE Transactions on Electron Devices,* vol. 62, pp. 3851-3856, 2015.

[23] C. Paoloni, A. D. Carlo, F. Bouamrane and e. al, "Design and realization aspects of 1-THz cascade backward wave amplifier based on double corrugated waveguide," *IEEE Transactional Electron Devices,* pp. 1236-1243, 2013.

[24] R. Basu, J. M. Rao, T. Le, R. Letizia and C. Paoloni, "Development of a D-Band Traveling Wave Tube for High Data-Rate Wireless Links," *IEEE Transactions on Electron Devices,* vol. 68, no. 9, pp. 4675-4680, 2021.

[25] C. Paoloni and A. Malekabadi, "UV-LIGA microfabrication process for sub-terahertz waveguides utilizing multiple layered SU-8 photoresist," *Journal of Micromechanics and Microengineering,* 2016.

[26] J. C. Tucek, M. A. Basten, D. A. Gallagher, K. E. Kreischer, R. Lai, V. Radisic, K. Leong and R. Mihailovich, "A 100 mW, 0.670 THz power module," in *IVEC 2012*, Monterey, 2012.

[27] J. M. Socuéllamos, R. Letizia, R. Dionisio and C. Paoloni, "Novel Meander Line Slow Wave Structure for W-band TWT," in *2020 45th International Conference on Infrared, Millimeter, and Terahertz Waves (IRMMW-THz)*, Buffalo, 2020.

[28] T. Baba, D. Mori, K. Inoshita and Y. Kuroki, "Light localizations in photonic crystal line defect waveguides," *IEEE Journal of Selected Topics in Quantum Electronics,* vol. 10, no. 3, pp. 484-491, 2004.

[29] R. Letizia, M. Mineo and C. Paoloni, "Photonic Crystal-Structures for THz Vacuum Electron Devices," *IEEE TRANSACTIONS ON ELECTRON DEVICES,* 2015.

[30] P.-S. Kildal, E. Alfonso, A. Valero-Nogueira and E. Rajo-Iglesias, "Local Metamaterial-Based Waveguides in Gaps Between Parallel Metal Plates," *IEEE ANTENNAS AND WIRELESS PROPAGATION LETTERS,* vol. 8, pp. 84-87, 2009.

[31] Dadashzadeh and E. Tahanian, "A Novel Gap-Groove Folded-Waveguide Slow-Wave Structure for G-Band Traveling-Wave Tube," *IEEE Transactions on Electron Devices,* vol. 63, no. 7, pp. 2912-2918, 2016.

[32] X. Li, X. Huang, S. Mathisen, R. Letizia and C. Paoloni, "Design of 71–76 GHz Double-Corrugated Waveguide Traveling-Wave Tube for Satellite Downlink," *IEEE Transactions on Electron Devices,* vol. 65, no. 6, pp. 2195 - 2200, 2018.

[33] R. Zheng, P. Ohlckers and X. Chen, "Particle-in-Cell Simulation and Optimization for a 220-GHz Folded-Waveguide Traveling-Wave Tube," *IEEE Transactions on Electron Devices,* vol. 58, no. 7, pp. 2164-2171, 2011.

[34] C. Paoloni, R. Basu, P. Narasimhan, J. Gates and R. Letizia, "Design and Fabrication of E-band Traveling Wave Tube for High Data Rate Wireless Links".

[35] J. Lai, Y. Gong, X. Xu, Y. Wei, Z. Duan, W. Wang and J. Feng, "W-Band 1-kW Staggered Double-Vane Traveling-Wave Tube," *IEEE Transactions on Electron Devices,* vol. 59, no. 2, pp. 496 - 503, 2011.

[36] M. J. Madou, Fundamentals of Microfabrication and Nanotechnology.

[37] H. Li, D. Li, Y. Hu, P. Pan, T. Li and J. Feng, "UV-LIGA microfabrication for high frequency structures of a 220GHz TWT amplifier," in *2016 IEEE International Vacuum Electronics Conference (IVEC)*, Monterey, CA , 2016.

[38] Y. Q. Fu, A. Colli, A. Fasoli, J. K. Luo, A. J. Flewitt, A. C. Ferrari and W. I. Milne, "Deep reactive ion etching as a tool for nanostructure fabrication," *Journal of Vacuum*

Science & Technology B: Microelectronics and Nanometer Structures Processing, Measurement, and Phenomena, p. 1520–1526, 2009.

[39] A. M. Cook, C. D. Joye, J. P. Calame and D. K. Abe, "3D-printed mold electroforming for microfabrication of W-band TWT circuits," in *2017 Eighteenth International Vacuum Electronics Conference (IVEC)*, London, 2017.

[40] H. Z. L. Hai, L. Ying, Y. Laixia and G. Yang, "Direct Ink Writing of Materials for Electronics-Related Applications: A Mini Review," *Frontiers in Materials,* vol. 8, 2021.

[41] "Everything You Need to Know About CNC Machining Tolerances," [Online]. Available: https://www.rapiddirect.com/blog/cnc-machining-services-tolerances/. [Accessed May 2023].

[42] C. D. Joye, J. P. Calame, M. Garven and B. Levush, "UV-LIGA microfabrication of 220 GHz sheet beam amplifier gratings with SU-8 photoresists," *JOURNAL OF MICROMECHANICS AND MICROENGINEERING,* 2010.

[43] G. Hong, A. Holmes and M. Heaton, "SU8 resist plasma etching and its optimisation," in *Symposium on Design, Test, Integration and Packaging of MEMS/MOEMS 2003*, Cannes, 2003.

[44] B. Bêche, P. Papet, D. Debarnot, E. Gaviot, J. Zyss and F. Poncin-Epaillard, "Fluorine plasma treatment on SU-8 polymer for integrated optics," *Optics Communications,* vol. 246, no. 1-3, pp. 25-28, 2005.

[45] G. Ulisse, P. Schürch, W. W. Koelmans and V. Krozer, "3D printing of a metallic helix for traveling wave tube amplifiers operating in millimeter wave range," in *2021 46th International Conference on Infrared, Millimeter and Terahertz Waves (IRMMW-THz)*, Chengdu, 2021.

[46] M. G. Silveirinha, C. A. Fernandes and J. R. Costa, "Electromagnetic Characterization of Textured Surfaces Formed by Metallic Pins," *TRANSACTIONS ON ANTENNAS AND PROPAGATION,* vol. 56, no. 2, 2008.

[47] Z. Liu, J.-Y. Deng and D. Sun, "Slow-Wave Groove Gap Waveguide Bandpass Filter," *IEEE Access,* vol. 7, pp. 52581-52588, 2019.

[48] E. Rajo Iglesias, M. Ferrando-Rocher and A. Uz Zaman, "Gap Waveguide Technology for Millimeter-Wave Antenna Systems," *IEEE Communications Magazine,* vol. 56, no. 7, pp. 14-20, 2018.

[49] B. J. Mousa, "Millimetre-Wave Components Based on Groove Gap Waveguide Technology: Design and Development," Liverpool, 2022.

[50] R. Letizia, M. Mineo and C. Paoloni, "Photonic Crystal-Structures for THz Vacuum Electron Devices," *IEEE TRANSACTIONS ON ELECTRON DEVICES,* vol. 62, no. 1, 2015.

[51] Y. Shi, W. Feng, Z. Qian, S. He, X. Y. Zhou, W. Che, Q. Xue and Q. Wu, "Gap Waveguide Technology," *IEEE Microwave Magazine,* pp. 62-73, 1 December 2022.

[52] D. Sievenpiper and e. al, "High-Impedance Electromagnetic Surfaces with a Forbidden Frequency Band," *IEEE TRANSACTIONS ON MICROWAVE THEORY AND TECHNIQUES,* 1999.

[53] P.-S. Kildal, E. Alfonso, A. Valero-Nogueira and E. Rajo-Iglesias, "Local Metamaterial-Based Waveguides in Gaps Between Parallel Metal Plates," *IEEE ANTENNAS AND WIRELESS PROPAGATION LETTERS,* vol. 8, pp. 84-87, 2009.

[54] D. M. Pozar, Microwave Engineering, New York: Wiley, 2009.

[55] F. Fan, J. Yang, V. Vassilev and A. U. Zaman, "Bandwidth Investigation on Half-Height Pin in Ridge Gap Waveguide," *IEEE Transactions on Microwave Theory and Techniques,* vol. 66, no. 1, pp. 100-108, 2017.

[56] E. Pucci, "Gap Waveguide Technology for Millimeter Wave Applications and Integration with Antennas," 2013.

[57] M. Ebrahimpouri, O. Quevedo-Teruel and E. Rajo-Iglesias, "Design Guidelines for Gap Waveguide Technology Based on Glide-Symmetric Holey Structures," *IEEE Microwave and Wireless Components Letters,* vol. 27, no. 6, pp. 542-544, 2017.

[58] F. Fan, J. Yang and P.-S. Kildal, "Half-height pins - a new pin form in gap waveguide for easy manufacturing," in *10th European Conference on Antennas and Propagation (EuCAP)*, Davos, 2016.

[59] E. Pucci, A. U. Zaman, E. Rajo-Iglesias and P.-S. Kildal, "New low loss inverted microstrip line using gap waveguide technology for slot antenna applications," in *Proceedings of the 5th European Conference on Antennas and Propagation (EUCAP)*, Rome, Italy, 2011.

[60] Q. Chen, F. Mesa, X. Yin and O. Quevedo-Teruel, "Accurate Characterization and Design Guidelines of Glide-Symmetric Holey EBG,," *IEEE Transactions on Microwave Theory and Techniques,* vol. 68, no. 12, pp. 4984-4994, 2020.

[61] R. Letizia, M. Mineo and C. Paoloni, "Photonic Crystal-Structures for THz Vacuum Electron Devices," *IEEE Transactions on Electron Devices,* vol. 62, no. 1, pp. 178-183, 2015.

[62] C. Paoloni, D. Gamzina, R. Letizia, Y. Zheng and N. C. L. Jr., "Millimeter wave traveling wave tubes for the 21st Century, Journal of Electromagnetic Waves and Applications," vol. 35, no. 5, pp. 567-603, 2021.

[63] L. R. Billa, M. N. Akram, C. Paoloni and X. Chen, "H - and E -Plane Loaded Slow Wave Structure for W -Band TWT," *IEEE Transactions on Electron Devices,* vol. 67, no. 1, pp. 309-313, 2020.

[64] R. Rennie and J. Jaw, A Dictionary of Physics, Oxford University Press, 2009.

[65] P. C. Panda, V. Srivastava and A. Vohra, "Analysis of Sheet Electron Beam Transport Under Uniform Magnetic Field," *IEEE Transactions on Plasma Science,* vol. 41, no. 3, pp. 461-469, 2013.

[66] K. T. Nguyen, J. A. Pasour, T. M. Antonsen, P. B. Larsen, J. J. Petillo and B. Levush, "Intense Sheet Electron Beam Transport in a Uniform Solenoidal Magnetic Field," *IEEE Transactions on Electron Devices,* vol. 56, no. 5, pp. 744-752, 2009.

[67] G. Liu, W. He, A. W. Cross, H. Yin and D. Bowes, "Simulation of a G-band sheet beam backward wave oscillator with double staggered metallic rod array," *Journal of Physics D: Applied Physics,* vol. 46, 2013.

[68] J. H. Booske, B. D. McVey and T. M. Antonsen, "Stability and confinement of nonrelativistic sheet electron beams with periodic cusped magnetic focusing," *Journal of Applied Physics,* 1993.

[69] Y.Saito, "BREAKDOWN PHENOMENA IN VACUUM," in *Proceedings of the 1992 Linear Accelerator Conference*, Ottawa, Ontario, 1992.

[70] R. Basu, L. R. Billa, J. M. Rao, R. Letizia and C. Paoloni, "Design of Slow Wave Structure for G-band TWT for High Data Rate Links," in *2019 International Vacuum Electronics Conference (IVEC)*, Busan, South Korea, 2019.

[71] R. Ives, "Microfabrication of high-frequency vacuum electron devices," *IEEE Transactions on Plasma Science,* vol. 32, no. 3, pp. 1277-1291, 2004.

[72] H. Braunisch, X. Gu, A. Camacho-Bragado and L. Tsang, "Off-Chip Rough-Metal-Surface Propagation Loss Modeling and Correlation with Measurements," in *2007 Proceedings 57th Electronic Components and Technology Conference*, Sparks, NV, USA, 2007.

[73] M. V. Lukic and D. S. Filipovic, "Modeling of 3-D Surface Roughness Effects With Application to μ-Coaxial Lines," *IEEE Transactions on Microwave Theory and Techniques,* vol. 55, no. 3, pp. 518-525, 2007.

[74] M. Ebrahimpouri, E. Rajo-Iglesias, Z. Sipus and O. Quevedo-Teruel, "Low-cost metasurface using glide symmetry for integrated waveguides," in *2016 10th European Conference on Antennas and Propagation (EuCAP)*, Davos, Switzerland, 2016.

[75] Z. Sipus, K. Cavar, M. Bosiljevac and E. Rajo-Iglesias, "Glide-Symmetric Holey Structures Applied to Waveguide Technology: Design Considerations.," *Sensors (Basel).,* 2020.

[76] Q. Chen, F. Mesa, X. Yin and O. Quevedo-Teruel, "Accurate Characterization and Design Guidelines of Glide-Symmetric Holey EBG," *IEEE TRANSACTIONS ON MICROWAVE THEORY AND TECHNIQUES,* vol. 68, no. 12, 2020.

[77] K. T. Nguyen, J. Pasour, A. Vlasov, S. Cooke, L. Ludeking, B. Levush and D. K. Abe, "Oscillation characteristics in waveguide-based TWT amplifiers," in *2015 IEEE International Vacuum Electronics Conference (IVEC)*, Beijing, 2015.

[78] D. Chernin et al, "TWT stability for frequencies near a band edge," in *2013 IEEE 14th International Vacuum Electronics Conference (IVEC)*, Paris, 2013.

[79] D. Hung, I. Rittersdorf, P. Zhang, D. Chernin, Y. Lau, J. T. Antonsen, J. Luginsland, D. Simon and R. Gilgenbach, "Absolute Instability near the Band Edge of Traveling-Wave Amplifiers," *Phys. Rev. Lett.,* vol. 115, no. 12, 2015.

[80] Y. Xie, N. Bai, C. Shen, H. Fan, Z. Chen and X. Sun, "Backward-Wave Oscillation Suppression in Folded Waveguide Traveling-Wave Tube With Metamaterial Absorber," *IEEE Access,* vol. 11, pp. 4830-4837, 2023.

[81] K. T. Nguyen and e. al, "Design Methodology and Experimental Verification of Serpentine/Folded-Waveguide TWTs," *IEEE TRANSACTIONS ON ELECTRON DEVICES,* 2014.

[82] S. Cogollos, M. Brumos, V. E. Boria, C. Vicente, J. Gil, B. Gimeno and M. Guglielmi, "A Systematic Design Procedure of Classical Dual-Mode Circular Waveguide Filters Using an Equivalent Distributed Model," *IEEE Transactions on Microwave Theory and Techniques,* vol. 60, no. 4, pp. 1006 - 1017, 2012.

[83] R. Picone, B. Baum and R. McKendry, "Plasma microcontact patterning (PμCP): a technique for the precise control of surface patterning at small-scale," *Methods Cell Biol. ,* 2014.

[84] J. Chen, Z. Wang, F. Wang, C. Gao, J. Li, Q. Xie, Z. Zi, J. Cai and J. Feng, "Demonstration of a Broadband W-Band Microwave Power Module With Improved Gain Flatness," *IEEE Electron Device Letters,* vol. 43, no. 8, pp. 1335 - 1338, 2022.

[85] M. Mineo, C. Paoloni, A. D. Carlo, A. M. Fiorello and M. Dispenza, "Corrugated waveguide slow-wave structure for THz travelling wave tube," in *European Microwave Conference (EuMC)*, 2009.

[86] M. Mineo and C. Paoloni, "0.22 THz TWT based on the double corrugated waveguide," in *IEEE International Vacuum Electronics Conference*, 2014.

[87] C. Paoloni and M. Mineo, "Double-Corrugated Rectangular Waveguide Slow-Wave Structure for Terahertz Vacuum Devices," *IEEE Transactions on Electron Devices,* vol. 57, no. 11, pp. 3169-3175, 2010.

[88] A. Z. Abozied and R. Letizia, "Gap waveguides for millimeter wave slow wave structures," in *2021 22nd International Vacuum Electronics Conference (IVEC)*, 2021.

[89] D. Sun, X. Chen, J.-Y. Deng, L.-X. Guo, W. Cui, K. Yin, Z. Chen, C. Yao and F. Huang, "Gap Waveguide With Interdigital-Pin Bed of Nails for High-Frequency Applications," *IEEE Transactions on Microwave Theory and Techniques,* vol. 67, no. 7, pp. 2640 - 2648, 2019.

[90] C. Paoloni, D. Gamzina, R. Letizia, Y. Zheng and N. C. L. Jr., "Millimeter wave traveling wave tubes for the 21st Century, Journal of Electromagnetic Waves and Applications," vol. 35, no. 5, pp. 567-603, 2021.

[91] A. Z. Abozied, J. Gates and R. Letizia, "Half-Height Pin Gap Waveguide-Based Slow-Wave Structure for Millimeter Wave Traveling-Wave Tubes," *IEEE Transactions on Electron Devices (Early Access),* pp. 1 - 7, 2023.

[92] A. Z. Abozied and R. Letizia, "Investigation of gap waveguide-based slow wave structure for millimeter wave travelling wave tubes," in *2021 14th UK-Europe-China Workshop on Millimetre-Waves and Terahertz Technologies (UCMMT)*, Lancaster, UK, 2021.

[93] C. Q. Choi, " These Transistor Gates Are Just One Carbon Atom Thick - Researchers may have hit a hard limit," IEEE Spectrum, 2022.

[94] C. M. Armstrong, E. C. Snively, M. Shumail, C. Nantista, Z. Li, S. Tantawi, B. W. Loo, R. J. Temkin, R. G. Griffin, J. Feng, R. Dionisio, F. Mentgen, N. Ayllon, M. A. Henderson and T. Goodman, "Frontiers in the Application of RF Vacuum Electronics," *IEEE Transactions on Electron Devices (Early Access),* pp. 1 - 13, 2023.

[95] M. Mineo and C. Paoloni, "Double-Corrugated Rectangular Waveguide Slow-Wave Structure for Terahertz Vacuum Devices," *IEEE Transactions on Electron Devices,* vol. 57, no. 11, pp. 3169-3175, 2010.